



The  
University  
Of  
Sheffield.

# MOCVD Growth and Characterization of High Quality Semi-polar (11-22) AlGaN Obtained with Overgrowth Technique

**By:**  
Zhi LI

Supervisor: Professor Tao Wang

A thesis submitted for the degree of  
Doctor of Philosophy (Ph.D.)

The University of Sheffield  
Faculty of Engineering  
Department of Electronic and Electrical Engineering

Submission Date  
April, 2018

# Abstract

Epitaxial growth of semi-polar (11-22) AlGa<sub>N</sub> layers with different Al composition has been performed by using the metal organic chemical vapour deposition (MOCVD) technique. A two-step overgrowth technique has been developed to both improve the crystal quality and address the cracking issue simultaneously for the AlGa<sub>N</sub> growth. Comprehensive studies on the structural and optical properties of the AlGa<sub>N</sub> overgrowth layers have been performed.

Semi-polar (11-22) AlGa<sub>N</sub> layers with various Al compositions have been obtained with two different approaches. The first one is the standard AlGa<sub>N</sub> growth on the planar (10-10) *m*-plane sapphire substrates with either AlN or GaN buffer layer. Semi-polar AlGa<sub>N</sub> multiple quantum wells (MQWs) with various QW thickness grown on this standard template show no clear blueshift in optical emission wavelength with increasing excitation power, indicating the absence of quantum-confined Stark effect (QCSE). However, this method results in inadequate crystal quality and serious wafer cracking in the epilayers.

To address both issues, another approach - a two-step overgrowth technique - has been developed. With such overgrowth technique, we have achieved thick ( $> 2 \mu\text{m}$ ) and crack-free semi-polar (11-22) AlGa<sub>N</sub> layers grown on the top of nearly but not yet fully-coalesced GaN overgrown on micro-rod arrayed templates. These overgrowth layers with the Al composition up to 55.3% exhibit the best crystal quality ever achieved compared to other reports.

A comprehensive investigation on the reduction of defects including the basal-plane stacking faults (BSFs) and strain relaxation has been carried out on the AlGa<sub>N</sub> overgrowth layers. Detailed X-ray diffraction measurements in on-axis and off-axis planes for different AlGa<sub>N</sub> structures indicate significantly reduced dislocation density in the AlGa<sub>N</sub> overgrowth samples. The BSF density is also found to be greatly reduced with the overgrowth technique by performing both the (11-22) reciprocal space mapping (RSM) and the low temperature (LT) photoluminescence (PL) measurements.

The in-plane and out-of-plane strain in the overgrown AlGa<sub>N</sub> layers have been calculated by adopting a triclinic unit cell model, exhibiting anisotropic strain along two primary in-plane directions and even compressive instead of tensile in-plane strain. The great strain relaxation has been attributed to the residual voids formed within the underlying GaN during the overgrowth process. It has been found that large lattice tilts between the AlGa<sub>N</sub> and the GaN are present, which also confirms dramatic strain relaxation along the in-plane direction.

Furthermore, the optical properties of the AlGa<sub>N</sub> samples with Al composition ranging from 32.0% to 55.3% have been investigated systematically. Both the near-band-edge (NBE) and BSFs-related emission are studied by LT PL and room temperature cathodoluminescence (CL) measurements. The energy separation between the two emission peaks increases with increasing Al composition, which is mainly ascribed to the compositional discrepancy within BSF regions and enhanced QCSE also within the BSF regions.

Temperature-dependent PL measurements have also been performed to study the exciton localization effect in both emission regions, showing the localization depth of the BSFs-related emission is larger than that of the NBE in each sample. More importantly, a detailed comparison study has been performed on these semi-polar AlGa<sub>N</sub> samples and their *c*-plane AlGa<sub>N</sub> counterparts with similar Al composition. All the semi-polar AlGa<sub>N</sub> samples show a clear reduction in exciton localization depth and PL linewidth compared with their *c*-plane counterparts. These results presented demonstrate that semi-polar (11-22) AlGa<sub>N</sub> may be more favourable to be employed towards deep UV laser diodes than *c*-plane AlGa<sub>N</sub>.

# Acknowledgement

Pursuing a PhD degree overseas is always not an easy thing for everybody. I am very grateful to arrive at this final stage of my PhD studies with so many people's care and help, to whom I would like to take the opportunity here to show my most sincere gratitude.

First of all, I want to express my sincere gratitude to my supervisor Prof. Tao Wang. My PhD project should not have been finished without his professional support and instructions. Thanks to his recommendation, I was awarded the faculty scholarship which supported my whole life in the UK. He guided me how to take care of the MOCVD machine, how to deal with problems when something has happened and also instructed me how to grow and analyse. His enthusiasm and hard work on research profoundly influenced me and impressed me. His trust on me gave me overwhelming pressure, although made me progress very fast.

I realised that I made him quite disappointed at the final stage of my PhD studies, and I felt very sorry and sad for this. I did not mean to, I just have my own reasons. No matter how he will look at me, I will never hate him and always remember what he has offered to me, and show my deeply respect to him.

Furthermore, my special thanks go to Dr. Yipin Gong and Dr. Xiang Yu. They helped me quite a lot on the MOCVD operation and growth. They always stayed together with me in the cleanroom, either to discuss with me or support me in the growth. Their ideas and suggestions on the MOCVD growth are quite helpful for me, and their accompany always gets rid for my loneliness and fear.

I also would like to show my sincere appreciation to Dr. Jie Bai and Mr. Ling Jiu. They provided a lot of high quality templates for my growth, which saved my time and eased my pressure. I know that template fabrication is a complex and time-consuming job. Both of them spent huge time on it. Dr. Bai also helped me a lot on proof reading. And Mr. Jiu helped me to measure a lot of SEM images. Their work is very important for me, and I thank them very much.

I am also very thankful to Dr. Liancheng Wang, who is not only my colleague but also my very good friend. We get the same supervisor in China and have the same supervisor in the UK, nothing can break down such a bond between us. He supported me a lot on new MOCVD growth and also helped me organise and revise my paper manuscripts. No more

existing words than thank you could express my gratitude to him. I wish him have a bright career and better life in future.

Also, many thanks to Dr. Benbo Xu, who gave me help on the treatment and some measurements. And thank Dr. King Xun, who provided templates for overgrowth. Many thanks to Mr. Yun Zhang, who trained me how to use time-resolved PL and PLE. And thank Dr. Yaonan Hou, who provided nonporous templates for me and lots of helpful discussions, and many thanks to Mr. Xuanming Zhao, who supported me a lot on the MOCVD growth, sample treatment and XRD measurements. Specially, I am grateful to Mr. Shuoheng Shen, who provided a lot of help in my private life.

I also would like to thank Dr. Duc Dinh, who supported me quite a lot in my last year. He helped me to make plans for the growth with his experience and excellent ideas. He gained my great respect with his professional skills as well as his personalities.

I would like to extend my thanks to other colleagues. Many thanks to Dr. Rick Smith, who gave me a lot of help on the 244 laser maintenance and PL measurement. His patience and kindness impressed me very much. Also thank Dr. Modestos Athanasious, who provided me lots of support on PL setup and gave many helpful discussions on the measurements. Many thanks to some other colleagues, Mr. Nicolas Poyiatzis, Mr. Zohaib Ahmed Syed, and Mr. Suneal Ghataora, who provided useful discussions and kind suggestions.

I want to specially thank the team from Strathclyde University, Prof. Robert Martin and Dr. Jochen Bruckbauer. They performed CL measurements for my samples and gave me a lot of support for my journal publications.

My project could not go so smoothly without support from many technicians and staffs from the EEE department and the III-V centre. I want to show my appreciation to our senior technician, Mr. Paul Haines, who supported our group a lot on the machine repair. He also provides me a lot of help on the cleanroom induction and training. Many thanks to Mr. David Morris, Mr. Jon Milner, Mr. Richard Frith, Dr. Paul Fry, Dr. Ian Farrer and Dr. Rob Airey, who provide extensive support on different equipment maintenance and training. Also thank Mr. Gordon Askwith for keeping the cleanroom tidy and clean.

Many thanks to Hilary, Frances, and Dr. Thomas Walter. Their excellent work makes my PhD study go smoothly. Special thanks to Dr. Chaoyuan Jin, who encouraged me and gave me guidance when I felt depressed and helpless.

Sincerely thank my father, who always thought about me even in front of death. I will keep in mind for ever what he had done for me, and always wish him take care in heaven with

my deepest sincerity. Also, thank my mother and my brother, thank you for your understanding and endless support.

Finally, thank my wife and lovely daughter. Nothing can express my love to you both. The only thing I can do for you is to accompany you all the time.

Zhi Li  
Sheffield, UK  
October, 2017

# List of Publications

## Journal Publications

1. **Z. Li**, L. Jiu, Y. Gong, L. Wang, Y. Zhang, J. Bai, and T. Wang. “Crack-free Semipolar (11-22) AlGa<sub>N</sub> on overgrown GaN on micro-rod template: simultaneous quality improvement and strain management”, *Applied Physics Letters* 110, 082103 (2017).
2. **Z. Li**, L. Wang, L. Jiu, Y. Gong, Y. Zhang, J. Bruckbauer, J. Bai, R. Martin, and T. Wang. “Optical investigation of semipolar (11-22) AlGa<sub>N</sub> with High Al Composition”. *Applied Physics Letters* 110, 091102 (2017).
3. J. Bruckbauer, **Z. Li**, N. K. Gunasekar, M. Warzecha, P. Edwards, L. Jiu, Y. Gong, J. Bai, T. Wang, C. Trager-Cowan, and R. Martin. “Spatially-resolved optical and structural properties of semi-polar (11-22) Al<sub>x</sub>Ga<sub>(1-x)</sub>N with x up to 0.56”, *Scientific Reports* 7, 10804 (2017).
4. Y. Gong, K. Xing, B. Xu, X. Yu, **Z. Li**, J. Bai, and T. Wang. “(Invited) High Efficiency Green-Yellow Emission from InGa<sub>N</sub>/Ga<sub>N</sub> Quantum Well Structures Grown on Overgrown Semi-Polar (11-22) Ga<sub>N</sub> on Regularly Arrayed Micro-Rod Templates”. *ECS Transaction* 66, 151 (2015).
5. J. Bai, Y. Gong, **Z. Li**, Y. Zhang, and T. Wang, “Semi-polar InGa<sub>N</sub>/Ga<sub>N</sub> multiple quantum well solar cells with spectral response at up to 560 nm”. *Solar Energy Materials and Solar Cells* 175, 47 (2018).

## Conference Publications

1. **Z. Li**, L. Jiu, Y. Gong, L. Wang, Y. Zhang and T. Wang, “Growth and optical investigation of semipolar (11-22) AlGa<sub>N</sub> with high Al composition on overgrown GaN on micro rod templates”, *UK Nitrides Consortium (UKNC) Summer Conference*, Sheffield, UK (2016). Oral presentation.
2. **Z. Li**, L. Wang, L. Jiu, J. Bruckbauer, Y. Gong, Y. Zhang, J. Bai, R. W. Martin and T. Wang, “Exciton Localization of Semi-polar (11-22) Al<sub>x</sub>Ga<sub>1-x</sub>N with High Al Composition”, *UK Nitrides Consortium (UKNC) Winter Conference*, Oxford, UK (2017). Poster.
3. **Z. Li**, L. Wang, L. Jiu, J. Bruckbauer, Y. Gong, Y. Zhang, J. Bai, R. W. Martin and T. Wang, “Structural and Optical Investigation of Semi-polar (11-22) Al<sub>x</sub>Ga<sub>1-x</sub>N with High Al Composition”, *Semiconductor and Integrated Optoelectronics (SIOE)*, Cardiff, UK (2017). (Oral presentation done by Dr. Gong).
4. L. Jiu, Y. Gong, Y. Zhang, **Z. Li**, J. Bai and T. Wang, “High quality non-polar (11-20) GaN overgrown on mask-patterned micro-rod arrayed templates”, *Semiconductor and Integrated Optoelectronics (SIOE)*, Cardiff, UK (2017).
5. J. Bruckbauer, G. Naresh-Kumar, **Z. Li**, L. Jiu, P. R. Edwards, J. Bai, T. Wang, C. Trager-Cowan, and R. W. Martin, “Optical and structural properties of semi-polar (11-22) AlGa<sub>N</sub> epilayers with high AlN content”, *International Symposium on Semiconductor Light Emitting Devices (ISSLED)*, Alberta, Canada (2017).
6. C. Brasser, J. Bruckbauer, **Z. Li**, L. Jiu, J. Bai, P. R. Edwards, T. Wang and R. W. Martin, “Luminescence and conductivity studies of chevrons in semi-polar (11-22) InGa<sub>N</sub>/Ga<sub>N</sub> multiple quantum well structures”, *International Conference on Nitride Semiconductors (ICNS)*, Strasbourg, France (2017).

# Abbreviations

<b>AlN</b>	aluminium nitride	<b>LT</b>	low temperature
<b>AlGaN</b>	aluminium gallium nitride	<b>MFC</b>	mass flow controller
<b>AlInGaN</b>	aluminium indium gallium nitride	<b>MO</b>	metal organic
<b>A<sup>0</sup>X</b>	acceptor-bound exciton	<b>MOCVD</b>	metal organic chemical vapour deposition
<b>BSF</b>	basal-plane stacking fault	<b>MOVPE</b>	metal organic vapour phase epitaxy
<b>CCD</b>	charge-coupled detector	<b>NBE</b>	near-band-edge
<b>CCS</b>	close-coupled showerhead	<b>NH<sub>3</sub></b>	ammonia
<b>CH</b>	crystal-field split-off hole	<b>PC</b>	pressure controller
<b>CL</b>	cathodoluminescence	<b>PL</b>	photoluminescence
<b>CMP</b>	chemical mechanical polishing	<b>PLE</b>	photoluminescence excitation
<b>Cp<sub>2</sub>Mg</b>	bis(cyclopentadienyl)magnesium	<b>PMT</b>	photomultiplier tube
<b>DAP</b>	donor-acceptor pair	<b>ppb</b>	parts per billion
<b>DIC</b>	differential interference contrast	<b>ppm</b>	parts per million
<b>DUV</b>	deep ultra-violet	<b>PSF</b>	prismatic stacking fault
<b>D<sup>0</sup>X</b>	donor-bound exciton	<b>QB</b>	quantum barrier
<b>ELOG</b>	epitaxial laterally overgrowth	<b>QCSE</b>	quantum-confined stark effect
<b>EQE</b>	external quantum efficiency	<b>QW</b>	quantum well
<b>FWHM</b>	full width at half maximum	<b>RLP</b>	reciprocal lattice point
<b>FX</b>	free exciton	<b>RSM</b>	reciprocal space map
<b>GaN</b>	gallium nitride	<b>RT</b>	room temperature
<b>H<sub>2</sub></b>	hydrogen	<b>MQW</b>	multiple quantum well
<b>HEMT</b>	high electron mobility transistor	<b>sccm</b>	standard cubic millimetres per minute
<b>HH</b>	heavy hole	<b>SE</b>	secondary electron
<b>InN</b>	indium nitride	<b>SEM</b>	scanning electron microscopy
<b>IQE</b>	internal quantum efficiency	<b>SiC</b>	silicon carbide
<b>LD</b>	laser diode	<b>SiH<sub>4</sub></b>	silane
<b>LED</b>	light-emitting diode		
<b>LH</b>	light hole		
<b>LO</b>	longitudinal optical		

<b>Si<sub>2</sub>H<sub>6</sub></b>	disilane	<b>TMIn</b>	trimethylindium
<b>TEM</b>	transmission electron microscope	<b>UV</b>	ultra-violet
<b>TMAI</b>	trimethylaluminium	<b>WPE</b>	wall plug efficiency
<b>TMGa</b>	trimethylgallium	<b>XRC</b>	X-ray diffraction rocking curve

# Table of Contents

Abstract .....	I
Acknowledgement .....	III
List of Publications .....	VI
Abbreviations .....	VIII
Chapter 1 Introduction .....	1
1.1 Research History of III-nitride UV Devices .....	1
1.2 State-of-the-art and Challenges.....	3
1.3 Motivation and Aim.....	6
1.4 Thesis Organization .....	8
References .....	9
Chapter 2 Background .....	11
2.1 General Introduction to Semiconductors .....	11
2.2 Physics of III-nitride Semiconductors .....	12
2.2.1 Material Property .....	13
2.2.2 Crystal Structure .....	14
2.2.3 Electronic Band Structure .....	15
2.3 Semi-polar and Non-polar.....	18
2.3.1 Polar Plane and Polarity.....	18
2.3.2 Spontaneous and Piezoelectric Polarization .....	18
2.3.3 Semi-polar and Non-polar Planes .....	20
2.3.4 Other Properties .....	21
2.4 Defects in III-nitrides .....	22
2.4.1 Point defects.....	22
2.4.2 Dislocations.....	23
2.4.3 Stacking Faults (SFs) .....	26
2.5 Epitaxial Growth.....	28
2.5.1 Substrate and Lattice Mismatch.....	28
2.5.2 Traditional Two-step Growth .....	29
2.5.3 Epitaxial Laterally Overgrowth (ELOG) .....	30
2.5.4 Semi-polar and Non-polar Growth .....	31
References.....	34
Chapter 3 Experimental Techniques .....	37

3.1 Metal Organic Chemical Vapour Deposition (MOCVD).....	37
3.1.1 Introduction.....	37
3.1.2 System Principle .....	38
3.1.3 Gas Delivery .....	39
3.1.4 MO Sources .....	41
3.1.5 Close-coupled Showerhead Reactor .....	43
3.1.6 In-situ Monitoring.....	44
3.2 Characterization Techniques.....	46
3.2.1 Nomarski Microscopy.....	46
3.2.2 X-ray Diffraction (XRD) .....	47
3.2.3 Scanning Electron Microscopy (SEM) .....	50
3.2.4 Cathodoluminescence (CL) .....	51
3.2.5 Photoluminescence (PL) .....	51
References.....	54
Chapter 4 Epitaxial Growth of Semi-polar (11-22) AlGa <sub>N</sub> on Planar Substrates.....	55
4.1 Introduction.....	55
4.2 Semi-polar (11-22) AlGa <sub>N</sub> Epilayer Growth .....	55
4.2.1 Growth Parameters.....	55
4.2.2 Structural Characterization .....	58
4.2.3 Optical Properties.....	60
4.3 Semi-polar (11-22) AlGa <sub>N</sub> MQWs .....	62
4.3.1 RT and LT PL .....	62
4.3.2 Power dependent PL .....	64
4.4 Conclusion .....	66
References.....	67
Chapter 5 Epitaxial Growth of Semi-polar (11-22) AlGa <sub>N</sub> with Overgrowth Technique .....	68
5.1 Introduction.....	68
5.2 Experimental Details.....	69
5.2.1 Template Fabrication .....	69
5.2.2 Overgrowth Procedures .....	71
5.3 Characterization and Discussions .....	72
5.3.1 Surface morphology.....	72
5.3.2 Determination of the Al Content.....	75
5.3.3 Crystal Quality .....	77

5.3.4 Optical Property .....	78
5.3.5 Growth Temperature Effect .....	80
5.4 Conclusion .....	83
References .....	84
Chapter 6 Defect and Strain Analysis of Semi-polar (11-22) AlGa <sub>N</sub> Obtained with Overgrowth Technique.....	86
6.1 Introduction.....	86
6.2 Experimental Details.....	87
6.3 Defect Reduction Analysis .....	88
6.3.1 On-axis (11-22) reflection.....	88
6.3.2 Off-axis reflections .....	90
6.3.3 (11-22) RSMs.....	92
6.3.4 BSFs in LT PL .....	93
6.4 Strain Relaxation.....	94
6.4.1 Strain modelling in semi-polar (11-22).....	94
6.4.2 Analysis for the strain calculation.....	96
6.4.3 Lattice tilt in (11-22) and (11-24) RSMs .....	98
6.5 Conclusion .....	100
References.....	101
Chapter 7 Optical Investigation of High-Quality Semi-polar (11-22) AlGa <sub>N</sub> layers.....	102
7.1 Introduction.....	102
7.2 Experimental Details.....	103
7.3 Results and Discussion .....	105
7.3.1 LT PL.....	105
7.3.2 RT CL .....	107
7.3.3 Temperature dependent PL.....	108
7.3.4 Localization Effect.....	111
7.4 Conclusion .....	112
References.....	114
Chapter 8 Summary and Future work.....	116
8.1 Summary .....	116
8.2 Future work.....	118

# Chapter 1 Introduction

Group III-nitride semiconductors, including GaN, AlN, InN and their ternary and quaternary alloys have attracted much attention due to their unique properties for optoelectronic and electronic applications. The last two decades have seen the remarkable breakthroughs on the research and development of III-nitride materials and devices, which have led to the award of the Nobel Prize in Physics in 2014 [1]. III-nitride-based optoelectronics such as blue/green/white light-emitting diodes (LEDs) and violet/blue laser diodes (LDs) have been successfully commercialized after a period of tremendous growth and rapid progress. Alongside this, other applications in power electronics, e.g. radio frequency power amplifiers [2] and high electron mobility transistors (HEMTs) [3] have also experienced remarkable success during the same period. Solid-state lighting based on III-nitride LEDs is replacing the conventional light bulbs to bring a revolution in energy technologies and change the entire human life in this century [4].

While III-nitride emitters working in the visible spectral range (400 – 700 nm) have made unparalleled progress during recent years, ultraviolet (UV) emitters especially deep UV (DUV) (< 300nm) emitters based on Al-containing alloys, e.g. AlGaN or AlInGaN are less developed due to technique difficulties. Although considerable effort has been paid in short-wavelength UV emitters due to their wide applications [5] in air/water purification, UV curing, information storage and short-range communication etc., big gaps between the visible and UV devices in terms of device performance still remain.

This chapter starts with an overview of the development of III-nitrides, particularly on AlGaN-based structures and devices. Subsequently, current status and technical issues of AlGaN-based UV emitters are presented, followed by the motivation and aims of our research on semi-polar (11-22) AlGaN. Finally, the structure of this thesis is explained.

## 1.1 Research History of III-nitride UV Devices

Although the research on III-nitrides could be traced back to the 1930s when the GaN crystal was first synthesized [6], high-quality materials required for III-nitride-based devices have only been realised in the past two decades, which could be attributed to a lot of pioneering

work done by the three Nobel Prize laureates, who are Prof. I. Akasaki, Prof. H. Amano and Prof. S. Nakamura. The method used for the heteroepitaxial growth of III-nitrides with a low-temperature GaN or AlN nucleation layer was developed around the nineties, which enables high crystal quality epilayers grown on foreign substrates (e.g. sapphire) [7-8]. Alongside this, p-type GaN, which was unachievable previously, was realized by using either low-energy electron beam irradiation [9] or N<sub>2</sub>-ambient thermal annealing [10]. The two-step growth technique and development of n-type and p-type materials led to the rapid growth and progress for developments of III-nitride visible LEDs and LDs.

The research about III-nitride UV devices initiated in the 1990s, just after the time when Amano first demonstrated the use of low-temperature AlN buffer layer and Nakamura first introduced low-temperature GaN nucleation layer to improve the quality of epilayers significantly. The first AlGaIn/GaN multiple quantum well (MQW) LED emitting at 353 nm was reported by Han *et al.* from Yale University in 1998 [11]. Afterwards researchers from the worldwide groups such as University of South Carolina, RIKEN, and Northwestern University shortened the emission wavelength further by adopting different structures. The shortest wavelength of an AlN LED is 210 nm, which was achieved by Taniyasu *et al.* from NTT in 2006 [12].

**Table 1.1 Some milestones in the development of III-nitride-based UV LEDs and LDs.**

Key Achievements	Contributors, Year	Reference
First AlGaIn-GaN-AlGaIn MQWs	Khan <i>et al.</i> , 1990	[13]
First AlGaIn/GaN MQW LED (353nm)	Han <i>et al.</i> , 1998	[11]
First 352-nm LED on bulk GaN	Nishida <i>et al.</i> , 2001	[14]
First 305-nm AlInGaIn LED	Khan <i>et al.</i> , 2001	[15]
First 280-nm LED with AlInGaIn MQWs	Yasan <i>et al.</i> , 2002	[16]
First 250-nm AlGaIn LED	Adivarahan <i>et al.</i> , 2002	[17]
First AlGaIn MQW LD < 360 nm	Kneissl <i>et al.</i> , 2003	[18]
First 350.9 nm AlGaIn/GaN LD	Iida <i>et al.</i> , 2004	[19]
First 210-nm AlN LED	Taniyasu <i>et al.</i> , 2006	[12]
Stimulated emission from AlN at 214nm	Shatalov <i>et al.</i> , 2006	[20]
First 336-nm AlGaIn MQW LD	Yoshida <i>et al.</i> , 2008	[21]

For the AlGaIn-based UV LEDs, the first device operating at wavelengths below 360 nm was reported by Kneissl *et al* in 2003 [18]. And the shortest wavelength which has been achieved is 336 nm, reported by Hamamatsu Photonics in 2008 [21].

Some milestones in the development of AlGaIn-based UV devices could be briefly summarized in Table 1.1.

## 1.2 State-of-the-art and Challenges

The last decade has seen a significant development of III-nitride UV LEDs due to the continuously improved material quality. Current status on the external quantum efficiency (EQE) of III-nitride UV LEDs is summarized in Figure 1.1.

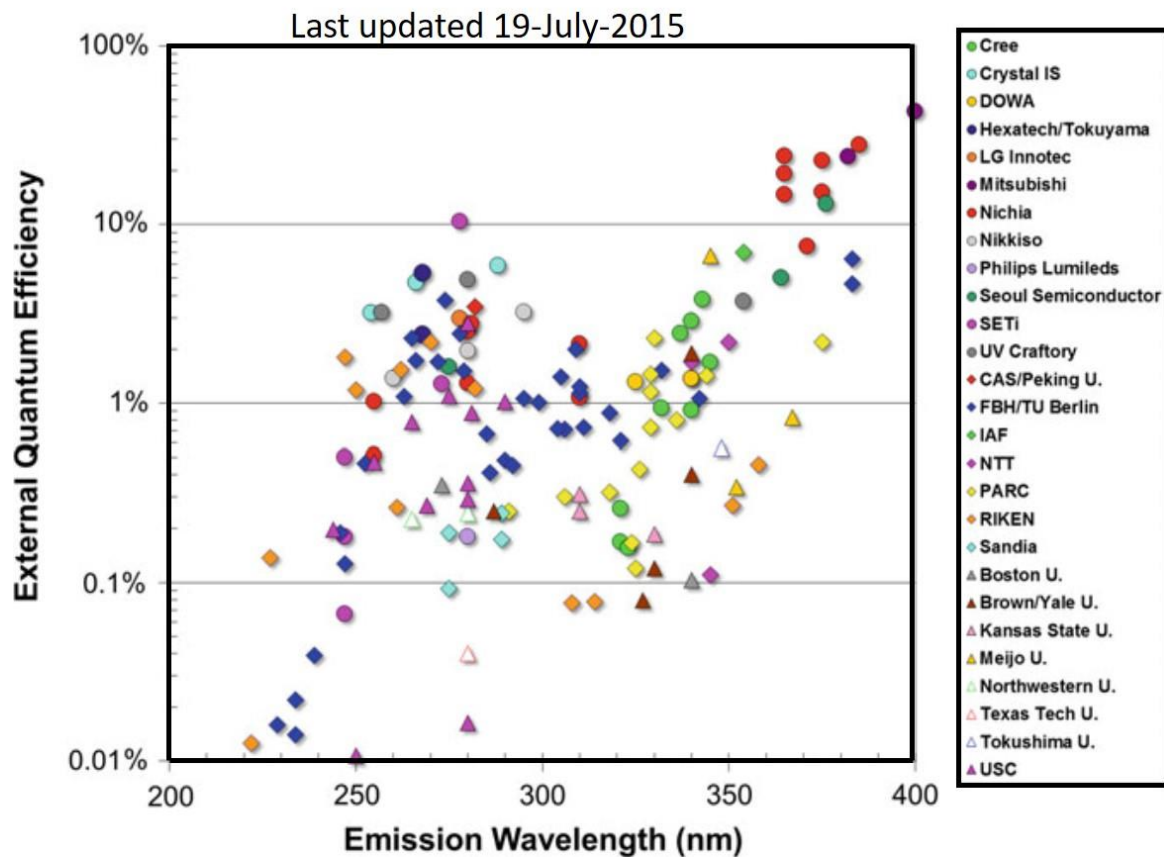


**Figure 1.1 Current status in EQE for AlGaIn-based UV LEDs. Taken from [22].**

While the EQE achieved for LEDs emitting in the near-UV and visible spectral ranges is as high as 60-80%, the figure for UV LEDs shorter than 365 nm is at least one order of magnitude less [22]. A record EQE up to 14.3 % in a DUV LED was reported by UV Craftory in 2014 [23]. Very recently, an even higher EQE > 20 % for a UV LED operating at 275 nm was reported by Takano *et al* [24].

The light output power dramatically decreases when the wavelength becomes shorter. An output power of above 30 mW of a 270-nm UV LED has been obtained by Hirayama *et al* [25], whereas only several tens of nW was achieved for the LED emitting at 210 nm [14].

Therefore, despite the fact that emission wavelengths of UV LEDs that have been obtained span the entire UV-A (400-320 nm) and UV-B (320-280 nm) range and even goes though the UV-C (280-200nm) range, AlGaIn-based UV LEDs suffer from relatively low EQE and light output power.

Generally, the energy conversion efficiency or the wall plug efficiency (WPE) of LEDs is described by the following equation:

$$WPE = \frac{P_{out}}{I \cdot V} = \eta_{EQE} \cdot \frac{\hbar\omega}{e \cdot V} \quad (1.1)$$

where  $P_{out}$  is the light output power,  $I$  the injection current,  $V$  the operation voltage,  $\hbar\omega$  the energy of photons and  $\eta_{EQE}$  the EQE. There are three factors that affect the EQE - the carrier injection efficiency ( $\eta_{inj}$ ), the radiative recombination efficiency ( $\eta_{rad}$ ) and the light extraction efficiency ( $\eta_{ext}$ ). The relation between these factors can be expressed as:

$$\eta_{EQE} = \eta_{inj} \cdot \eta_{rad} \cdot \eta_{ext} = \eta_{IQE} \cdot \eta_{ext} \quad (1.2)$$

All factors that limit these efficiencies will consequently limit the EQE and affect the device performance.

### Material Quality

AlGaIn is currently the most promising candidate for DUV LEDs. Many problems encountered in developing AlGaIn-based UV LEDs are related with the crystal quality of this material. The large lattice mismatch between the foreign substrate and the AlN epilayers generates high density of threading dislocations (typically in the order of  $10^{10} \text{ cm}^{-2}$ ), which normally act as non-radiative recombination centres and hence reduce the radiative recombination efficiency. The growth of AlGaIn, compared with GaN, is also more difficult due to a much larger sticking coefficient and lower surface mobility of Al adatoms, which contributes to a high density of extended defects, such as dislocations and grain boundaries, and poor surface morphology [26]. Furthermore, the pre-reaction between the Al precursors (trimethylaluminium or triethylaluminium) and ammonia ( $\text{NH}_3$ ) resulting in gas-phase byproduct formation makes the epitaxy of high-quality AlGaIn even more difficult.

Another challenge about growth is the strain management to enable the achievement of thick and crack-free AlGaIn epilayers. AlGaIn grown on GaN templates normally suffers from tensile stress which leads to the wafer cracking and disrupts the fabrication of devices such as LEDs. With increasing the Al content, this issue becomes more severe.

## Quantum-confined Stark Effect (QCSE)

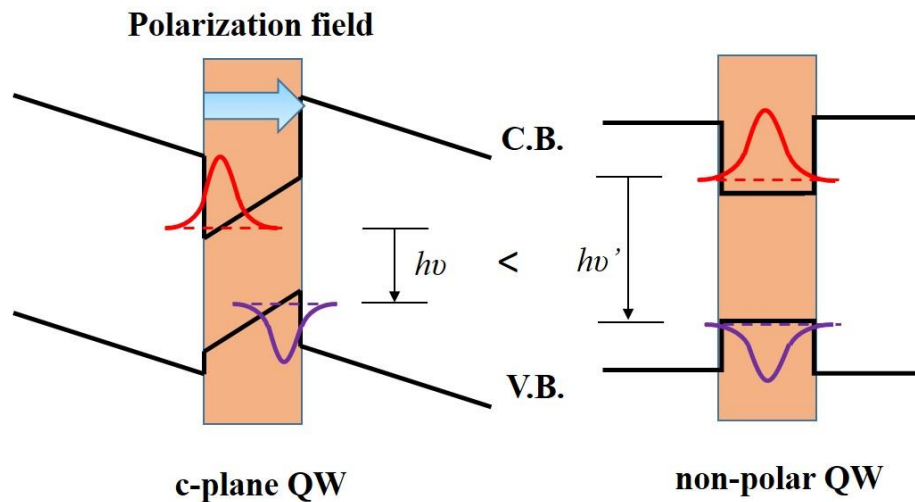


**Figure 1.2 Illustration of QCSE showing the band bending, electron and hole wave functions separation in the active regions of *c*-plane and non-polar structures.**

The quantum-confined Stark effect (QCSE), which is induced by the spontaneous and piezoelectric polarization fields in active regions along the polar direction, is another major obstacle for obtaining high efficiency UV LEDs. The strain owing to the lattice mismatch between the QW and the barrier results in piezoelectric charges at the interfaces, leading to the formation of the piezoelectric field. These polarization fields could cause the bending of the valence and conduction bands, leading to the separation of electron and hole wave functions [27], as shown in Figure 1.2. The fields become stronger with increasing Al content. Consequently, probabilities of the radiative recombination within the active regions decrease and the internal quantum efficiency is to be potentially reduced.

## Doping

In addition to the issues in epitaxial growth, both the n- and p-type doping in AlGa<sub>0.27</sub>N are more difficult than GaN due to the higher ionization energies of donors (e.g. silicon) and acceptors (e.g. magnesium) in AlGa<sub>0.27</sub>N, which leads to lower ionization efficiencies. This becomes more severe in AlGa<sub>0.27</sub>N layers with higher Al compositions as the activation energy also increases, resulting in higher resistivity and non-uniformity of current injection for devices, so-called “current crowding” [26]. P-type doping in high-Al-composition AlGa<sub>0.27</sub>N is even more challenging as the binding energy of Mg acceptors becomes larger, leading to much lower hole concentration. Studies of Mg-doped p-type AlGa<sub>0.27</sub>N layers have shown that activation energy of Mg acceptors increases from 150 meV in GaN to 310 meV in Al<sub>0.27</sub>Ga<sub>0.73</sub>N and will further increase as the Al content increases [28]. In addition to the high resistivity, it is also difficult to achieve an ohmic contact to p-AlGa<sub>0.27</sub>N, which is mainly attributed to the doping issue as well

as the lack of metals with work function larger than p-AlGaN [29]. The Mg-related compensating defects in addition to the background defects in p-AlGaN result in low uncompensated acceptor density (which is equal to  $N_a - N_d$ , where  $N_a$  and  $N_d$  are the doping density of acceptors and donors respectively), which hinders the formation of ohmic contact [30-31]. It is also understood that surface states in AlGaN play an important role for the ohmic contact formation [32].

### **Light extraction**

Another challenge in the UV LEDs is the low light extraction efficiency, which is mainly due to the strong UV absorption of the materials beneath the QWs or above the QWs. The devices grown on either Si or SiC substrates, or on thick GaN templates on sapphire substrates, exhibit strong absorption in UV regions. Indium-tin-oxide (ITO), which is widely used as the current spreading layers in InGaN-based visible LEDs, is not suitable for the UV-emitting devices owing to the strong UV absorption as well. In addition, the absorption of UV light from the p-GaN contact layers and typical semi-transparent metal contacts, e.g. Ni/Au, decreases the extraction efficiency further [26]. Although these contact layers are quite thin, the absorption coefficient increases at the shorter wavelengths.

Another limiting factor to obtain high extraction efficiency involves the light polarization property of the AlN material. Owing to the different symmetry of sub-bands in the topmost valence band in AlN [33], the optical transitions from the top valence sub-band in *c*-plane AlN is polarized parallel to the *c*-axis, e.g.  $\mathbf{E} // \mathbf{c}$ , whereas the corresponding transition in GaN is  $\mathbf{E} \perp \mathbf{c}$ . Such out-of-plane polarization property (e.g.  $\mathbf{E} // \mathbf{c}$ ) in the *c*-plane AlN or high-Al-content AlGaN is a drawback for the light extraction.

## **1.3 Motivation and Aim**

The motivation of this research derives from the wide applications of AlGaN-based UV devices emitting at different UV spectral ranges, as shown in Figure 1.3. The largest potential market for UV LEDs may be water purification/disinfection. Compared with conventional UV light sources, e.g. mercury lamps, UV LEDs show obvious advantages, such as compact and flexible, fast on/off switches, and environmental friendliness. With further improvements, they are expected to have long lifetime and low cost. Such application can be also applied to disinfection in food industry and medical areas as well. As DUV LDs with shorter emission wavelength enable the light beam into a smaller spot, they can be used to significantly increase the information storage density in optical data storage media. In addition, UV curing in dental

products, polymers and adhesives has already found many applications. Other applications such as biochemical detection, short-range communication and special lighting (light source for spectroscopy, illumination for white light and banknote) are also promising.

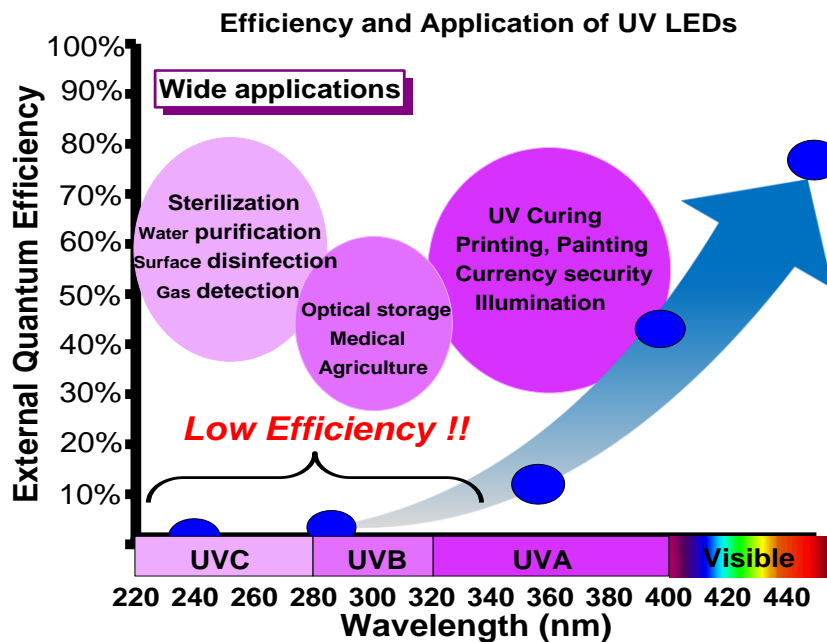


**Figure 1.3** A variety of applications of UV LEDs emitting at different wavelengths and the corresponding quantum efficiencies.

Despite of the wide-range applications mentioned above, critical technical issues have significantly impeded further improvements of AlGaIn-based UV emitters. Therefore, this thesis focuses on the development and studies of the growth of the high-Al-composition AlGaIn epilayers with the metal organic chemical vapour deposition (MOCVD) technique as well as characterization of these AlGaIn layers, in order to exploit their applicability for the UV devices. To address some critical technical issues in the conventional *c*-plane AlGaIn devices, such as cracking, high dislocation densities and severe QCSE, we have performed the AlGaIn growth on a semi-polar direction, i.e. (11-22), with a two-step overgrowth technique.

The aim of this work is to achieve high-quality and crack-free semi-polar (11-22) AlGaIn epilayers with high Al composition, which are highly desired for high efficiency UV emitters. The AlGaIn layers grown with the standard approach on planar substrates and with a two-step overgrowth technique on micro-rod arrayed templates were studied respectively. Also, we performed a comprehensive investigation on the AlGaIn overgrowth layers, aiming to establish an in-depth understanding of their structural and optical properties. Detailed characterization on the defect reduction and strain relaxation as well as optical investigation towards the high-quality semi-polar (11-22) AlGaIn epilayers with high Al composition were performed.

## 1.4 Thesis Organization

This thesis is organized as follows.

Chapter 1 presents a brief introduction on III-nitride-based UV emitters, including the research history, the state-of-the-art and challenges. The motivation and aim of research on semi-polar (11-22) AlGaN is also presented.

In Chapter 2, a general background of III-nitride semiconductors is described, including the physics of III-nitride semiconductors, the basic knowledge of the semi- and non-polar planes, defects and epitaxial growth of III-nitrides.

Chapter 3 introduces the experimental techniques used in this work, comprising of the epitaxy technology, namely MOCVD, as well as characterization techniques including Nomarski microscope, X-ray diffraction, photoluminescence, etc.

Chapter 4 shows the epitaxial growth of semi-polar (11-22) AlGaN epilayers with the standard approach, where AlGaN is directly grown on AlN or GaN buffer layer on *m*-plane sapphire. Semi-polar (11-22) AlGaN MQWs with various QW thickness grown on standard AlGaN templates are also studied to investigate the QCSE within the semi-polar MQWs.

In Chapter 5, a two-step overgrowth technique for semi-polar (11-22) AlGaN growth is developed in order to improve the crystal quality and address the cracking issue. Semi-polar AlGaN with different Al composition grown on overgrown GaN on micro-rod arrayed templates is obtained. Details on template fabrication, overgrowth procedures are present. Basic structural and optical properties of AlGaN overgrowth samples are also present and analysed.

In Chapter 6, structural properties of the high quality semi-polar (11-22) AlGaN layers with the overgrowth technique are further investigated. X-ray diffraction, along with the LT photoluminescence measurements, have been performed to investigate the mechanism of defect reduction in the overgrowth sample. And the strain state of the AlGaN is studied by the XRD calculation and is further investigated by the reciprocal space mapping.

In Chapter 7, optical investigation of high quality semi-polar (11-22) AlGaN is performed systematically. The LT and temperature-dependent photoluminescence as well as room temperature cathodoluminescence measurements have been employed in order to study the optical properties (in particular exciton localization) of both the near-band-edge (NBE) emission and the BSFs-related emission.

Chapter 8 is the summary and outlook.

## References

1. Website: [https://www.nobelprize.org/nobel\\_prizes/physics/](https://www.nobelprize.org/nobel_prizes/physics/).
2. U. K. Mishra, T. E. Kazior and Y. -F. Wu, Proc. IEEE 96, 287 (2008).
3. B. Lu, D. Piedra and T. Palacios, Adv. Semicond. Devices Microsyst., 105 (2010).
4. Refer to the solid-state lighting 2016 R&D plan of the Department of Energy, USA. Website: <https://energy.gov/eere/ssl/downloads/solid-state-lighting-2016-rd-plan>.
5. G. Tamulaitis, Lith. J. Phys. 51, 177 (2011).
6. W. C. Johnson, J. B. Parson, and M. C. Crew, J. Phys. Chem. **36**, 2651 (1932).
7. H. Amano, N. Sawaki, I. Akasaki, and Y. Toyoda, Appl. Phys. Lett. 48, 354 (1986).
8. S. Nakamura, T. Mukai, and M. Senoh, Appl. Phys. Lett. 64, 1687 (1994).
9. H. Amano, M. Kito, K. Hiramutsu, and I. Akasaki, Jpn. J. Appl. Phys. 28, L3112 (1989).
10. S. Nakamura, N. Iwasa, M. Senoh, and T. Mukai, Jpn. J. Appl. Phys. 31, 1258 (1992).
11. J. Han, M. H. Crawford, R. J. Shul, J. J. Figiel, M. Banas, L. Zhang, Y. K. Song, H. Zhou, and A. V. Nurmikko, Appl. Phys. Lett. 73, 1688 (1998).
12. Y. Taniyasu, M. Kasu, and T. Makimoto, Nature 441, 325 (2006).
13. M. A. Khan, T. A. Skogman, G. M. Van Hove, S. Krishnankutty, and R. M. Kolbas, Appl. Phys. Lett. 56, 1257 (1990).
14. T. Nishida, H. Saito, and N. Kodayashi, Appl. Phys. Lett. 79, 711 (2001).
15. M. A. Khan, V. Adivarahan, J. P. Zhang, C. Chen, E. Kuokstis, A. Chitnis, M. Shatalov, J. W. Yang, and G. Simin, Jpn. J. Appl. Phys. 40, L1308 (2001).
16. A. Yasan, R. McClintock, K. Mayes, S. R. Darvish, H. Zhang, P. Kung, and M. Razeghi, Appl. Phys. Lett. 81, 801 (2002).
17. V. Adivarahan, W. H. Sun, A. Chitnis, M. Shatalov, S. Wu, H. P. Maruska, and M. A. Khan, Appl. Phys. Lett. 85, 2175 (2004).
18. M. Kneissl, D. W. Treat, M. Teepe, N. Miyashita, and N. M. Johnson, Appl. Phys. Lett. 82, 4441 (2003).
19. K. Iida, T. Kawashima, A. Miyazaki, H. Kasugai, S. Mishima, A. Honshio, Y. Miyake, M. Iwaya, S. Kamiyama, H. Amano, and I. Akasaki, Jpn. J. Appl. Phys. 43, L499 (2004).
20. M. Shatalov, M. Gaeviski, V. Adivarahan, and A. Khan, Jpn. J. Appl. Phys. 45, L1286 (2004).
21. H. Yoshida, Y. Yamashita, M. Kuwabara, and H. Kan, Appl. Phys. Lett. 93, 241106 (2008).

22. M. Kneissl, J. Rass, III-Nitride Ultraviolet Emitters: Technology and Applications (Springer, Switzerland, 2016).
23. M. Ippommatsu, *Optronics* 2, 71 (2014).
24. T. Takano, T. Mino, J. Sakai, N. Noguchi, K. Tsubaki and H. Hirayama, *Appl. Phys. Express* 10, 031002 (2017).
25. H. Hirayama, S. Fujikawa and N. Kamata, *Electronics and Communications in Japan* 98, 5 (2015).
26. A. Khan, K. Balakrishnan, and T. Katona, *Nat. Photonics* 2, 77 (2008).
27. S. Chichibu, A. Uedono, T. Onuma, B. Haskell, A. Chakraborty, T. Koyama, P. Fini, S. Keller, S. DenBaars, J. Speck, U. Mishra, S. Nakamura, S. Yamaguchi, S. Kamiyama, H. Amano, I. Akasaki, J. Han, and Sota T, *Nat. Mater.* 5, 810 (2006).
28. H. Morkoç, *Handbook of Nitrides Semiconductors and Devices* (Wiley-VCH, Weinheim, 2008).
29. H. -K. Kim, T. -Y. Seong, I. Adesida, C. W. Tang, and K. M. Lau, *Appl. Phys. Lett.* 84, 1710 (2004).
30. S. -R. Jeon, Z. Ren, G. Cui, J. Su, M. Gherasimova, J. Han, H. -K. Cho, and L. Zhou, *Appl. Phys. Lett.* 86, 082107 (2005).
31. T. V. Blank, Y. A. Goldberg, E. V. Kalinina, O. V. Konstantinov, A. E. Nikolaev, A. V. Formin, and A. E. Dherenkoy, *Semiconductors* 35, 529 (2001).
32. R. T. Tung, *Mater. Sci. Eng. R* 35, 1 (2001).
33. M. Suzuki, T. Uenoyama, and A. Yanase, *Phys. Rev. B* 52, 8132 (1995).

# Chapter 2 Background

## 2.1 General Introduction to Semiconductors

Semiconductors are a group of materials with their conductivity between insulators and conductors. The unique behaviour on the electrical conductivity is determined by band structures which consist of the conduction band and the valence band. The conduction band is defined as the lowest unfilled energy band and the valence band is the highest energy band occupied by the valence electrons [1]. These two bands overlap in conductors such as metals, whereas they are separated by a forbidden gap in semiconductors and insulators.

The forbidden gap which refers to the energy difference between the bottom of the conduction band and the top of the valence band, is the band gap [1]. Based on the specific band structure, band gaps of semiconductors are divided into two classes: a direct band gap and an indirect band gap, as shown in Figure 2.1.

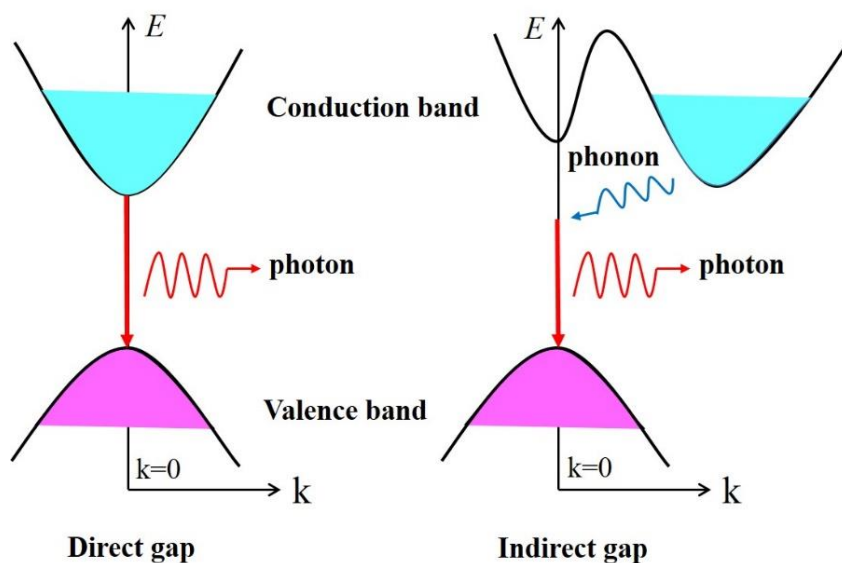


**Figure 2.1 Schematic band structure of the direct and indirect gap. A change in momentum in an optical transition is shown in the indirect gap.**

In direct-band-gap semiconductors such as GaAs, InP and GaN, the top of the valence band has the same value of momentum with the bottom of the conduction band, whereas in indirect-band-gap semiconductors such as Si and Ge the momentums are different. Such difference affects their optical properties significantly. The radiative recombination in a direct-band-gap semiconductor is quite fast as electrons can recombine with holes directly without

changing momentums. However, in the indirect-band-gap semiconductors, such process must be mediated by a phonon (or lattice vibration) in order to either gain or lose momentum, which makes the process far slower. This explains why optoelectronic devices such as LEDs and LDs are almost always made of direct-band-gap materials like GaAs, InP, GaN, etc.

The properties of intrinsic semiconductors could be changed by introducing additional impurities, which are known as dopants. Adding donor impurity atoms with more valence electrons into the solids produces n-type semiconductors as they provide excess valence electrons to the semiconductors, such as phosphorus-doped Si or Ge. Alternatively, adding acceptor impurity atoms with less valence electrons produces p-type semiconductors as they accept electrons from the intrinsic semiconductors and hence generate electron deficiencies, namely “holes”, such as B-doped Si. In both cases, an energy level of donor impurities close to the conduction band and an acceptor impurity level close to the valence band are then introduced respectively into the electronic energy band, which will affect both the electrical and optical performance of semiconductors greatly.

For III-nitride compound semiconductors, the most commonly used n-type and p-type dopants are Si and Mg respectively [2].

## 2.2 Physics of III-nitride Semiconductors

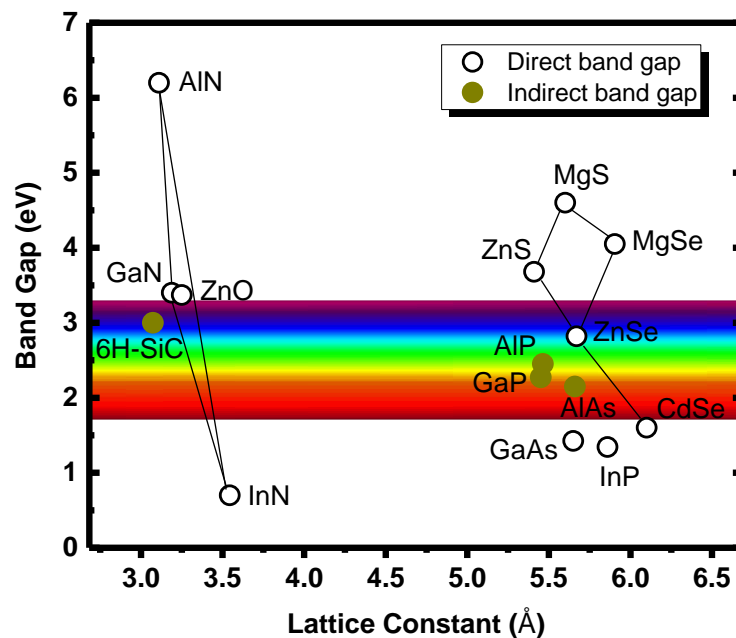


Figure 2.2 Band gaps of the common compound semiconductors versus their in-plane lattice constants. Taken from [3].

### 2.2.1 Material Property

The energy gaps of several compound semiconductors versus their in-plane lattice constants are shown in Figure 2.2.

As we know, II-VI compounds had attracted much attention over a period of time owing to their wide applications in light emitters and detectors [4]. These compounds have the same crystal structure and very close lattice constants to GaAs, which enables the lattice-matched epitaxy and high-quality II-VI layers. However, the severe stability problems e.g. short lifetimes, have prevented II-VI based light emitters from commercialization.

III-nitride compound semiconductors, normally grown at high temperature ( $> 1000$  °C) exhibit excellent chemical and thermal stability. With direct and wide band gaps, the emission spectrum of III-nitrides spans from infrared, visible to ultraviolet, which makes them promising candidates for optoelectronic devices, especially for blue, green and ultraviolet light emitters.

**Table 2.1 Some important parameters of GaN and other semiconductors.**

	<b>GaN</b>	<b>6H-SiC</b>	<b>4H-SiC</b>	<b>GaAs</b>	<b>Si</b>	<b>Diamond</b>
Band gap /eV	3.39	2.86	3.26	1.42	1.12	5.45
Electron saturation velocity / $10^7 \cdot s$	2.5	2.2	2.0	2.0	1.0	2.7
Electron mobility /[ $cm^2/(V \cdot s)$ ]	1200 (Bulk)	400	700	8500	1350	1900
Breakdown voltage/ $10^5 V \cdot cm^{-1}$	26	24	20	6	3	56
Dielectric constant	9	9.7	10	12.5	11.9	5.5
Thermal conductivity /[ $W/(cm \cdot K)$ ]	1.3	4.9	4.9	0.46	1.5	20

In addition, due to the large breakdown voltage and high electron saturation velocity, GaN based high power and high frequency transistors have also gained much attraction and have a wide application field. AlGaIn/GaN based HEMTs have been commercialized since 2006, and have been applied to various wireless infrastructure applications due to their high efficiency and high voltage operation [5].

Table 2.1 lists some basic physical parameters of III-nitride semiconductors and other important semiconductors.

### 2.2.2 Crystal Structure

III-nitride compounds can crystallize in three crystal structures: wurtzite, zinc blende and rock salt. The wurtzite and zinc blende structures can be stabilized in the epitaxial growth while the rock salt structure is only possible under high pressure. As the wurtzite is more stable thermodynamically at ambient conditions, bulk GaN, AlN and InN of wurtzite structure are more common.

The wurtzite and zinc blende structures of GaN are shown in Figure 2.3. Crystallographically, both structures are very similar and closely related. Each Ga (or nitrogen) atom in the lattice is coordinated by four nitrogen (or Ga) atoms. The main difference between the wurtzite lattice and the zinc blende lattice is the stacking sequence in the close-packed planes. The Bravais lattice of the zinc blende structure is cubic, containing four Ga elements and four nitrogen elements in a unit cell. And the stacking sequence for the (111) close-packed planes in this structure is:

$$\dots Ga_A N_A Ga_B N_B Ga_C N_C Ga_A N_A Ga_B N_B Ga_C N_C \dots$$

The wurtzite structure has a hexagonal unit cell, consisting of alternating diatomic close-packed (0001) planes of Ga and N pairs, and the stacking sequence in this direction is changed to:

$$\dots Ga_A N_A Ga_B N_B Ga_A N_A Ga_B N_B Ga_A N_A Ga_B N_B \dots$$

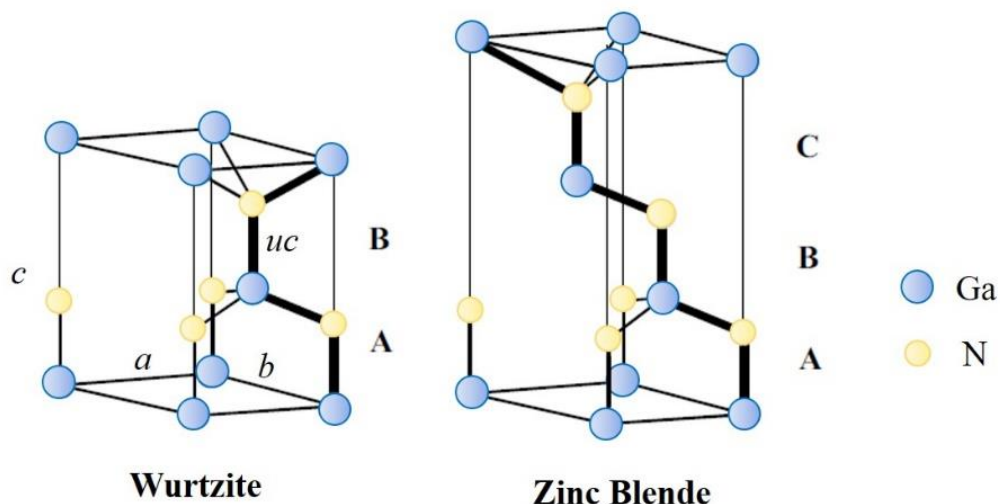


**Figure 2.3 The ball-and-stick model for the wurtzite and zinc blende unit cells in GaN. The different stacking sequence along the c direction is present.**

For the wurtzite structure, the axis that is perpendicular to the hexagonal unit cell is normally labelled as *c*-axis, which has the lattice constant *c*. And in the basal plane, there are

two lattice constants  $a$  and  $b$  which are equal,  $a = b$ . The space group of wurtzite structure is  $C_{6v}^4-P6_3mc$ , and the two inequivalent atom positions in the lattice are  $(1/3, 2/3, 0)$  and  $(1/3, 2/3, u)$ , where  $u$  is the internal structure parameter defined by the anion–cation bond length (or the nearest neighbour) divided by the lattice constant  $c$ . In an ideal wurtzite structure,  $u$  is equal to  $3/8$  and the ratio of  $c/a$  is  $\sqrt{8/3} = 1.633$ . However, a certain degree of deviation will occur if the wurtzite lattice is distorted from the ideal geometry.

Some crystal lattice parameters of the wurtzite III-nitride semiconductors are listed in Table 2.2 below.

**Table 2.2 Some crystal lattice parameters of the wurtzite III-nitrides.**

	Lattice constant/Å		Internal parameter $u$	Bond energy /eV/bond	Bond length / Å
	$a$	$c$			
GaN	3.189	5.185	0.377	2.20	1.94
AlN	3.111	4.978	0.382	2.88	1.89
InN	3.544	5.718	0.379	1.93	2.15

For III-nitride alloys, the lattice parameter dependence on alloy composition obeys the linear Vegard's law [6]. For instance, lattice constants of  $Al_xGa_{1-x}N$  alloys are determined by the lattice constant of both the GaN and the AlN with the following equation:

$$a_{Al_xGa_{1-x}N} = (1 - x) \cdot a_{GaN} + x \cdot a_{AlN} \quad (2.1)$$

where  $a_{AlN}$  and  $a_{GaN}$  are the lattice constant of the AlN and GaN respectively, and  $x$  is the AlN mole fraction.

### 2.2.3 Electronic Band Structure

As III-nitrides can be crystalized either in a wurtzite or zinc blende structure, the corresponding band gap could be different (see Table 2.3). For instance, the energy gap of wurtzite GaN (3.50 eV, 0K) is higher than that of zinc blende GaN (3.30 eV, 0K). It is also found that band gaps will shrink with increasing temperature, which is typically described by the Varshni's empirical expression:

$$E_g(T) = E_g(0) - \alpha T^2 / (\beta + T) \quad (2.2)$$

where  $E_g(T)$  and  $E_g(0)$  are the band gaps at  $T$  K and 0 K respectively, and  $\alpha$  and  $\beta$  are the fitting parameters.

For the ternary alloy like  $\text{Al}_x\text{Ga}_{1-x}\text{N}$ , the energy gap strongly depends on the Al composition. However, the composition dependence of  $\text{Al}_x\text{Ga}_{1-x}\text{N}$  band gap is nonlinear, which is normally approximated by the following empirical expression [7]:

$$E_g(\text{Al}_x\text{Ga}_{1-x}\text{N}) = x \cdot E_g(\text{AlN}) + (1 - x) \cdot E_g(\text{GaN}) - b \cdot x \cdot (1 - x) \quad (2.3)$$

where  $E_g(\text{GaN})$  and  $E_g(\text{AlN})$  are band gaps of the GaN and AlN respectively, and  $b$  is the bowing parameter which accounts for the deviation of the  $\text{Al}_x\text{Ga}_{1-x}\text{N}$  band gap from linearity. The reported values of  $b$  vary in a large range from -0.8 eV to +2.6 eV, which has been attributed to different strain state in epilayers due to substrates and buffer layers used, growth conditions, layer thickness, chemical ordering of the alloy, cracking of the layer, etc [8].

Table 2.3 lists some parameters of the band structure for wurtzite III-nitrides.

**Table 2.3 Some parameters of the band structure in wurtzite III-nitrides [9].**

		GaN	AlN	InN
$E_g$ (0K) /eV	Wurtzite	3.50	6.28	0.69 [10]
	Zinc Blende	3.30	5.35	-
Varshni parameters	$\alpha$ /meV·K <sup>-1</sup>	0.909	1.799	0.245
	$\beta$ /K	830	1462	624
Crystal field splitting $\Delta_{\text{cr}}$ /meV		42	-217	41
Spin-orbit coupling $\Delta_{\text{so}}$ /meV		13	19	1

For optoelectronic applications, the most important band structure of wurtzite nitrides is the direct band gap which allows fast radiative recombination and efficient light emission for LEDs and LDs. Since the structures of the valance and conduction band near the  $\Gamma$ -point ( $k=0$ ) in III-nitrides are strongly non-parabolic, the effective mass approximation which is quite useful for some III-V compounds like GaAs has severe limitation [9]. Also, owing to the crystal field splitting and the spin-orbit coupling, the topmost of the valence band near the  $\Gamma$ -point is split into three sub-bands, usually called A ( $\Gamma_9$ ), B ( $\Gamma_7$ ) and C ( $\Gamma_7$ ) sub-band. Consequently, there are three band gap excitons in wurtzite nitrides, namely A-, B- and C-excitons.

The schematic band structure of wurtzite GaN and AlN near the  $\Gamma$ -point is shown in Figure 2.4.

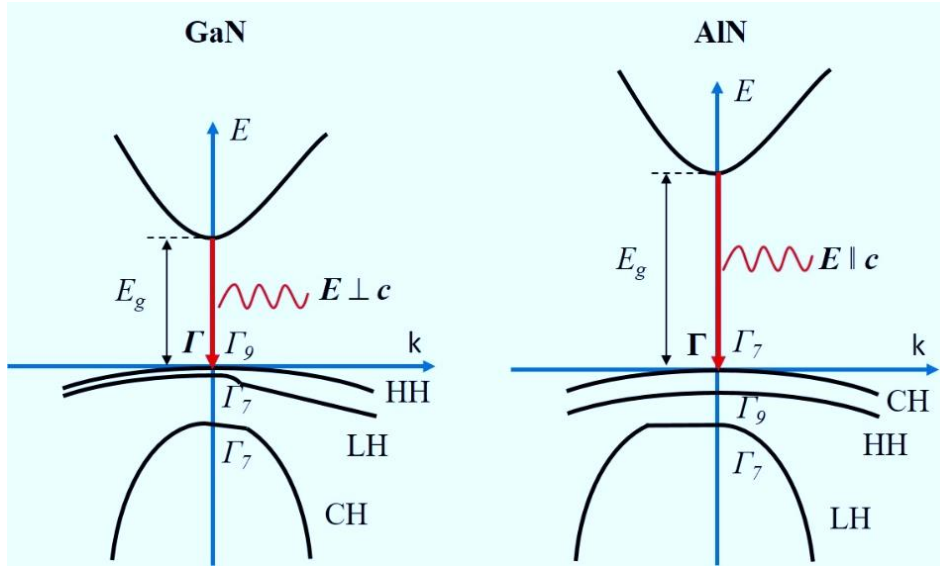


**Figure 2.4 Schematic diagram for the band structure of the wurtzite GaN and AlN. The symmetry of sub-bands is changed from  $\Gamma_9, \Gamma_7, \Gamma_7$  in GaN to  $\Gamma_7, \Gamma_9, \Gamma_7$  in AlN.**

Note that the crystal field splitting energy is a positive value for GaN and a negative value for AlN, as shown in Table 2.3, the hole band sequence near the  $\Gamma$ -point is changed from HH, LH, CH for GaN to CH, HH, LH for AlN, and the corresponding symmetry of sub-bands is changed from  $\Gamma_9, \Gamma_7, \Gamma_7$  for GaN to  $\Gamma_7, \Gamma_9, \Gamma_7$  for AlN [9]. Thus, photons emitted due to optical transition from conduction band to the top valence sub-band in GaN are polarized perpendicular to the  $c$  axis of the crystal ( $\mathbf{E} \perp \mathbf{c}$ ) while the corresponding transition in AlN is parallel to the  $c$  axis ( $\mathbf{E} \parallel \mathbf{c}$ ). This phenomenon results in strongly anisotropic emission properties in AlN but almost isotropic emission properties in GaN, leading to different light extraction efficiency between  $c$ -plane AlGaN-based LEDs and GaN-based LEDs (regardless of the absorption issue in UV LEDs).

For the AlGaN, polarization of the luminescence strongly depends on the Al composition, and it could change from  $\mathbf{E} \perp \mathbf{c}$  to  $\mathbf{E} \parallel \mathbf{c}$  as the Al composition increases from 0 to 1. Such emission property is usually characterized by the polarization degree  $\rho$ , which is defined through intensities of integrated PL components  $\mathbf{E} \perp \mathbf{c}$  ( $I_{\perp}$ ) and  $\mathbf{E} \parallel \mathbf{c}$  ( $I_{\parallel}$ ) as the following equation:

$$\rho = \frac{I_{\perp} - I_{\parallel}}{I_{\perp} + I_{\parallel}} \quad (2.4)$$

Since polarization of the  $c$ -plane AlGaN emission strongly influences the light escape from the epilayers, it is of crucial importance for III-nitride based light emitters, especially for those with high-Al-content AlGaN UVC devices [8].

## 2.3 Semi-polar and Non-polar

### 2.3.1 Polar Plane and Polarity

Owing to the lack of symmetry along the  $c$  axis, the wurtzite III-nitride crystals exhibit crystallographic polarity. This means III-nitride surfaces have either a (Ga, Al, In) polarity (or “face”) with group III atoms terminated, or a N polarity (or “face”) with N atoms terminated. The corresponding planes are denoted as (0001) and (000-1) respectively, as shown in Figure 2.5. For the GaN, (0001) plane is also known as the Ga-polar plane while (000-1) plane known as the N-polar plane [11].

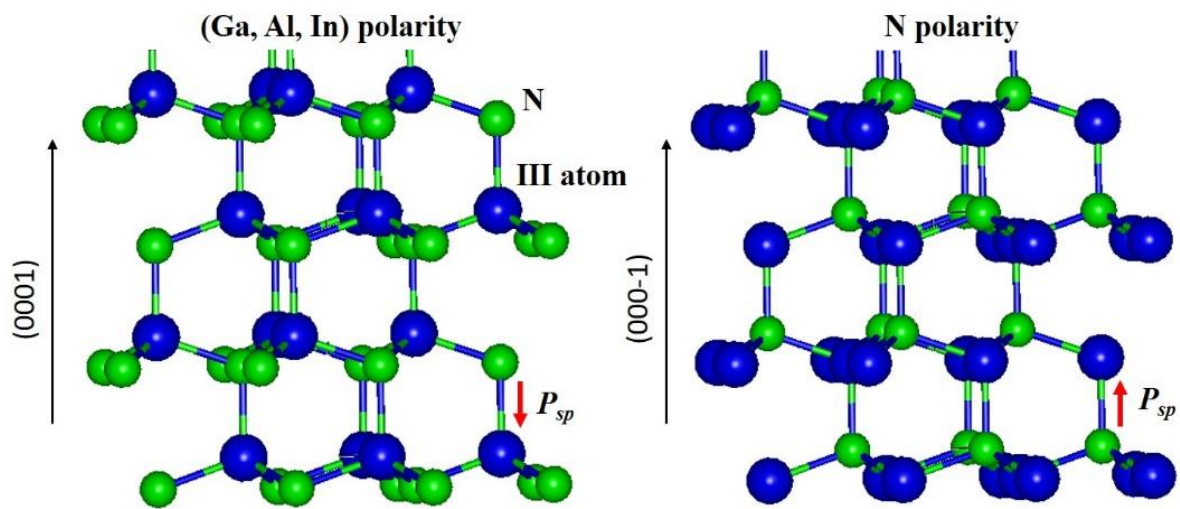


**Figure 2.5** The ball-and-stick model of the crystal structure of wurtzite nitrides with Ga face or N face.

Many properties of the material are affected by its polarity. For instance, the MOCVD-grown GaN with Ga face normally exhibits a smooth surface, whereas a hexagonal-faceted surface is often observed for GaN with N face [12]. The Ga face also exhibits much stronger stability in the wet chemical etching than the N face. Therefore,  $\text{H}_3\text{PO}_4$ - or  $\text{KOH}$ -based etchants are usually used to determine the polarity of III-nitrides as they can etch the N-polar surface easily whereas the surface morphology of the Ga-polar surface almost remains intact [11]. Other material properties such as incorporation of impurities (or doping), defect generation and piezoelectricity are also influenced by the polarity [13].

### 2.3.2 Spontaneous and Piezoelectric Polarization

The polarization in wurtzite III-nitrides due to heterointerfaces (spontaneous component) and strain (piezoelectric component) can be understood with Figure 2.6, where a tetrahedral

bond between Ga atoms and N atoms is illustrated. The direction of polarization vector  $\mathbf{P}_0$  is from N to Ga due to the electron cloud being closer to the N atoms. The cumulative polarization of the triply bonded atoms is along the  $c$ -direction. For an ideal GaN tetrahedron, both the in-plane and vertical component of polarization cancel one another and therefore no net polarization is exhibited.

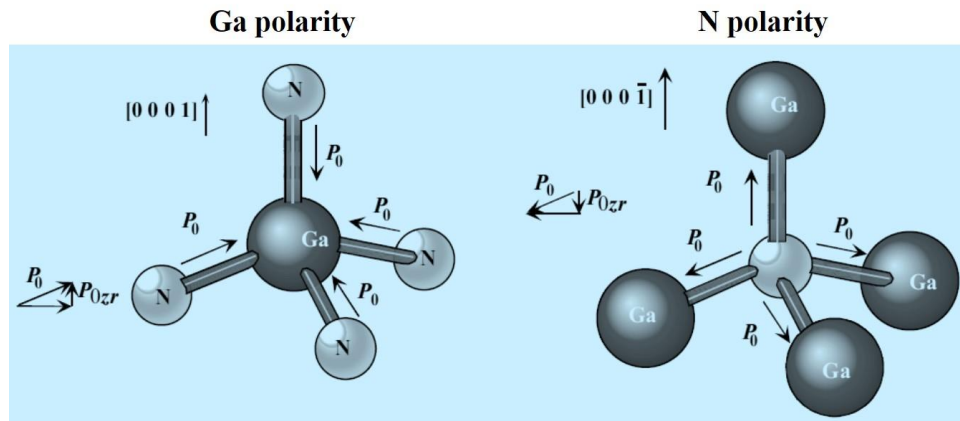


Figure 2.6 The ball-and-stick model of a GaN tetrahedron with Ga polarity and N polarity.  $\mathbf{P}_0$  is the spontaneous polarization vector of the Ga-N bond and  $\mathbf{P}_{0zr}$  is the  $z$ -component (along  $c$ -direction) of  $\mathbf{P}_0$ . Taken from [11].

However, when a heterointerface such as AlN/GaN structure is formed (assuming an AlN bilayer on top of the GaN bilayer with Ga polarity in Figure 2.6), due to the larger electronegativity of AlN than GaN, the net  $z$ -component of the polarization vector in triply bonded N-Al is larger in amplitude than the single Ga-N bond, and consequently there would be a net interfacial polarization in the vertical direction even without strain. Therefore, the spontaneous polarization at the heterointerfaces derives from the change in electronegativity of different materials across the interfaces and its direction can be changed in the Ga-polarity and N-polarity film [11].

On the other hand, if the ideal tetrahedron is under a homogeneous in-plane strain (assuming the tensile strain in a Ga-polarity film in Figure 2.6), the cumulative  $z$ -component of polarization vector involving the triple bonds decreases and cannot cancel the polarization of the single bond any more, resulting in a net polarization along the  $c$ -direction. Therefore, the piezoelectric polarization derives from the strain in an electronegative binary [11]. Obviously, the direction of piezoelectric polarization is related to the strain state either compressive or tensile strain.

As shown in Figure 2.7, the direction of the net polarization (or internal polarization fields) strongly depends on the strain states (compressive or tensile) and growth orientations (Ga face

or N face). The polarization induced built-in electric fields in III-nitrides have been demonstrated to be detrimental to the performance of light emitting devices by leading to the QCSE in the active regions, thus reducing the internal quantum efficiency of devices.

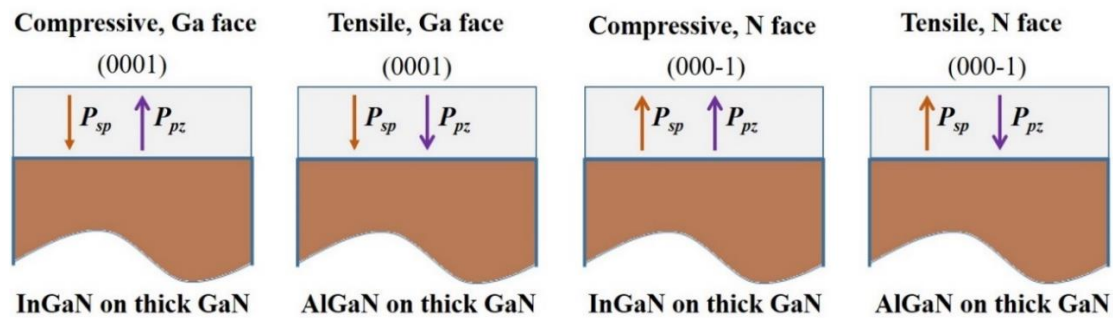


**Figure 2.7** Direction of the polarization field for the spontaneous and piezoelectric polarization in different III-nitride epilayers with a Ga or N face.

### 2.3.3 Semi-polar and Non-polar Planes

In addition to the polar plane, i.e. the (0001) *c*-plane, there are planes perpendicular to the *c*-plane in wurtzite nitrides, called non-polar planes. Such planes include (11-20) or *a*-plane, and (10-10) or *m*-plane. Crystal planes which are between the polar plane and non-polar planes are called semi-polar, such as (10-11), (11-22), (20-21) planes, etc. Some commonly used semi-polar and non-polar planes are sketched in Figure 2.8, and the inclined angle with respect to the *c*-plane is also shown beside.

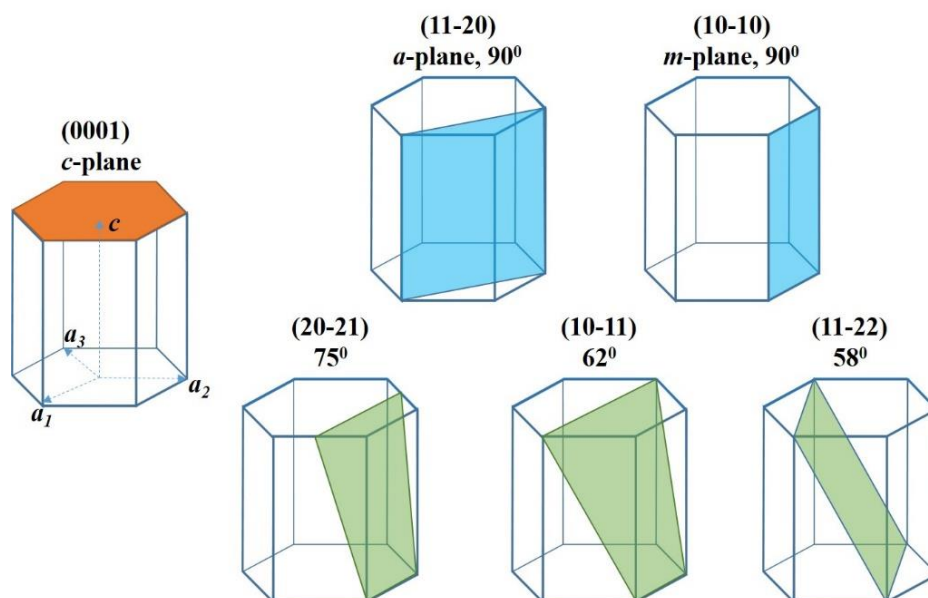


**Figure 2.8** Some commonly used semi-polar and non-polar planes in the hexagonal crystal structure. The inclination angle of each plane with respect to the *c*-plane is also shown.

It has been also found that the polarization electric field is strongly affected by the crystal orientation [14], as shown in Figure 2.9, where the polarization field of the AlGa<sub>x</sub>N on GaN layers with different Al composition is calculated. It can be seen that for a fixed crystal plane (except for non-polar planes and the ~45° inclined plane), the polarization field increases with increasing Al composition. The value of polarization field reaches its maximum at *c*-plane, whereas it is significantly reduced at some semi-polar planes such as (11-22) and (20-21), and even completely eliminated at non-polar planes. As the conventional epitaxy of III-nitrides is performed on *c*-plane which suffers from the severe polarization field induced QCSE, researches from worldwide start to shift their interest to epitaxy on semi-polar or non-polar planes to avoid such effect.

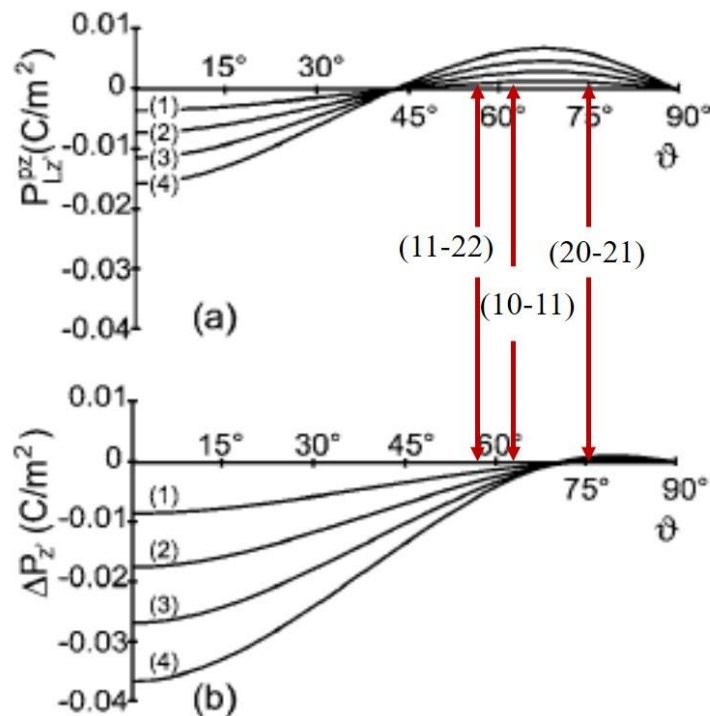


**Figure 2.9** The piezoelectric polarization  $P_{Lz'}^{pz}$  (a) and difference  $\Delta P_z$  of the total polarization (b) as a function of the inclination angle for AlGa<sub>x</sub>N on GaN layers. The Al content  $x = 0.1$  (1), 0.2 (2), 0.3 (3) and 0.4 (4). Taken from [14].

#### 2.3.4 Other Properties

In addition to the polarization electric field, many other properties of semi-polar and non-polar planes could differ from *c*-plane when the crystal orientation varies.

One of them is the efficiency of indium incorporation. Reports have shown that the semi-polar (11-22) GaN surface can accommodate more indium atoms due to the lower chemical potential [15] required for indium incorporation than other planes. Further studies [16] show

that the indium incorporation efficiency into GaN on different semi-polar planes could be summarized as:

$$(10-11) > (11-22) > (0001) = (20-21) = (10-12) \quad (2.5)$$

It is also reported that the efficiency of indium incorporation on a non-polar GaN surface is much lower than that on the *c*-plane [17]. This indicates that growing InGaN/GaN structures on a semi-polar orientation is more favourable to obtain higher In composition for longer wavelength emitters. Actually, InGaN emitters grown on semi-polar (11-22) orientation with the emission wavelength up to amber have been reported [18].

Moreover, semi-polar and/or non-polar GaN may exhibit different doping behaviours. For instance, Tsuchiya *et al* [19] reported that a Mg-doped *a*-plane GaN epilayer exhibited activation energy of 118 meV for Mg acceptors, which is much lower than that for current *c*-plane p-GaN (normally 150–170 meV). A first-principle calculation conducted by Akiyama *et al* [20] also shows that Mg atoms on the surface of (10-1-1) GaN could be more easily incorporated into electrically active substitutional lattice sites.

It has been also reported that the exciton localization energy of semi-polar (20-21) InGaN/GaN MQWs is lower than that of the *c*-plane counterparts [21]. And higher homogeneity of indium content within the InGaN QWs is also obtained on the (20-21) GaN surface [22]. These results indicate that growth on such a semi-polar plane might be a better choice for the green LDs.

## 2.4 Defects in III-nitrides

Defects in crystals can be formed during growth, implantation or thermal treatment. And they are typically classified according to their dimensional extension as:

- Zero-dimensional defects or point defects, such as vacancies, antisites and interstitials;
- One-dimensional defects or line defects, also called dislocations;
- Two-dimensional defects or planar defects, such as stacking faults;
- Three-dimensional defects or bulk defects like voids or pits.

### 2.4.1 Point defects

Point defects in the crystal are generated when an internal atom of the crystal is missing or staying in a non-lattice site, or an external atom is introduced into the lattice. These defects can be classified as vacancies, self-interstitial atoms, interstitial impurities and substitutional (larger or smaller) impurities, as shown in Figure 2.10.

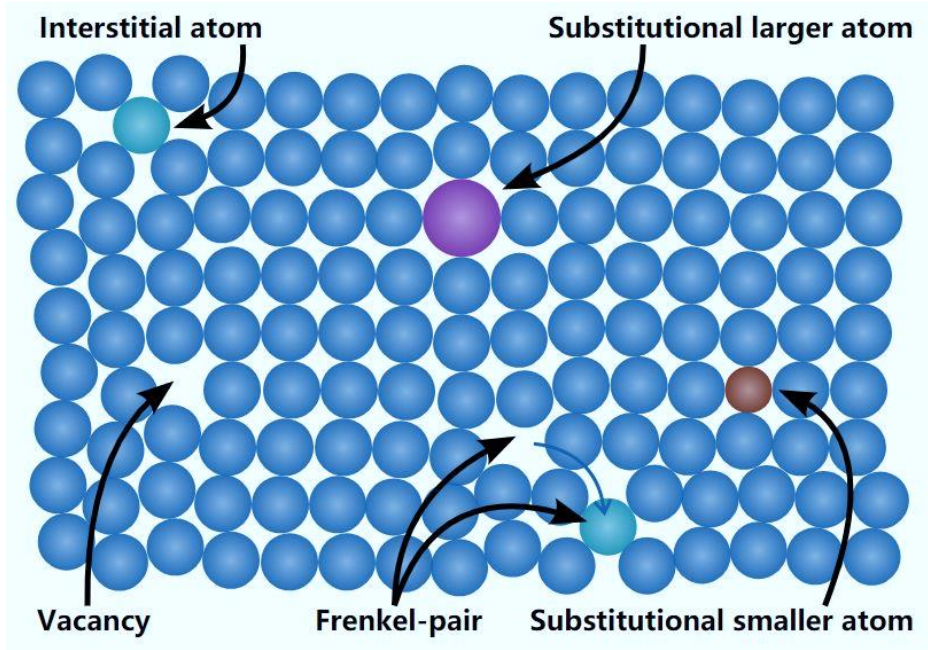


**Figure 2.10** Illustration of some common types of point defects in the crystals. Taken from [23].

Point defects in III-nitride semiconductors - either native defects like N vacancy and Ga vacancy or extrinsic contaminants introduced during growth like silicon, oxygen and carbon impurities - play important roles in both unintentional and intentional doping. They change the electron or hole concentration in n- or p-type semiconductors, affect the mobility of carriers, and form either shallow or deep energy levels within the band gap, which finally influences the electrical and optical behaviours of materials significantly. For instance, it is believed that nitrogen vacancy and/or oxygen contaminants contribute to the unintentional n-type doping in GaN [24]. The so-called ‘yellow-band luminescence’ in GaN is attributed to defects such as Ga vacancies and oxygen donors [25].

#### 2.4.2 Dislocations

In *c*-plane III-nitrides, the most prevalent line defects observed are threading dislocations (TDs), whose density could be up to  $10^8 - 10^{10} \text{ cm}^{-2}$ . Different to dislocations in the basal plane, TDs can propagate to the surface of the films except those that annihilate each other. Generally, TDs in *c*-plane nitrides are divided into three types: edge, screw and mixed dislocations, which are generally characterized by their Burgers vectors  $\mathbf{b}$  that describe the magnitude and direction of the lattice distortion. Dislocation lines and Burgers vectors of different TDs in *c*-plane nitrides are schematically shown in Figure 2.11.

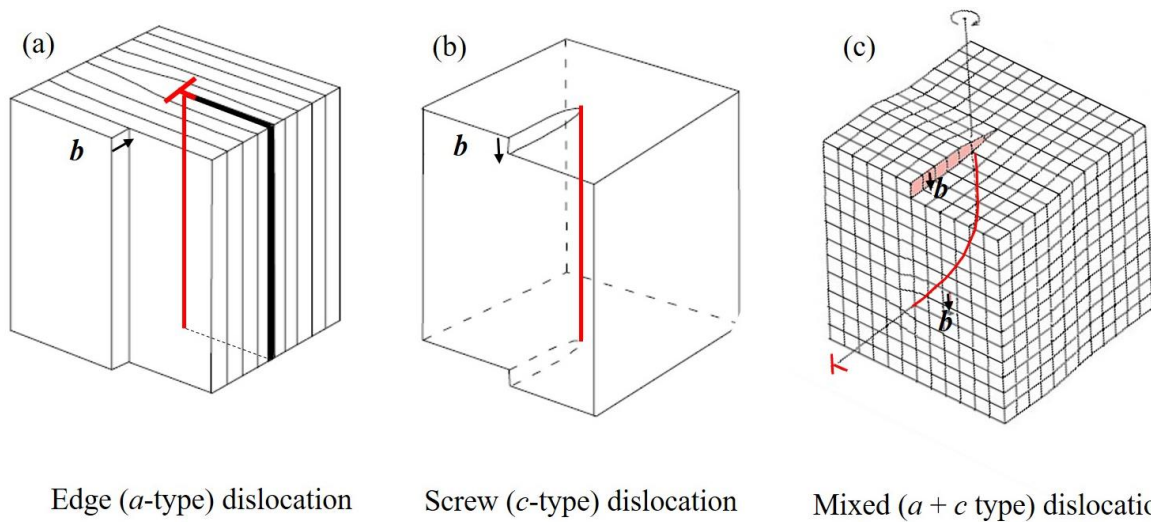


**Figure 2.11 Schematic of the edge (a), screw (b) and mixed (c) threading dislocations in *c*-plane III-nitrides. The corresponding Burgers vector and dislocation line are marked.**

Edge type TDs, also known as *a*-type, are formed by introducing or subtracting an extra half-atom plane in the crystal structure, with a Burgers vector of  $\mathbf{b} = 1/3 \cdot [11-20]$  and the magnitude of  $|\mathbf{b}| = 1/3 \cdot a$ , where  $a$  is the in-plane lattice constant. The screw type TDs, also known as *c*-type, is introduced by slipping a half crystal across another by a lattice vector, and it has a Burgers vector which is parallel to the dislocation line, normally  $\mathbf{b} = [0001]$  or  $[000-1]$  with the magnitude of  $|\mathbf{b}| = c$  where  $c$  is the out-of-plane lattice constant. The mixed type of TDs in III-nitrides, also termed as *c* + *a* type, is the combination of pure edge type and screw type dislocations, and its Burgers vector is  $\mathbf{b} = 1/3 \cdot [11-23]$ , which is  $\sim 10^\circ$  inclined with respect to the dislocation line  $[0001]$ .

In semi-polar and non-polar III-nitrides, however, they also suffer from high density of other defects, e.g. stacking faults and partial dislocations, in addition to the pure TDs mentioned above. The density of stacking faults in the semi/non-polar nitride films can be  $10^5 \sim 10^6 \text{ cm}^{-1}$  and the density of partial dislocations can be up to  $10^{10} \text{ cm}^{-3}$  [26]. Unlike the pure *a*- or *c*- type dislocation, partial dislocations normally have Burgers vectors which are not translation vectors of the lattice and they normally bound to a two-dimensional defect, usually a stacking fault. Typical partial dislocations observed in semi/non-polar III-nitrides include Shockley partials ( $\mathbf{b} = 1/3 \cdot [1-100]$ ), Frank partials ( $\mathbf{b} = 1/2 \cdot [0001]$ ) and Frank-Shockley partials ( $\mathbf{b} = 1/6 \cdot [20-23]$ ) [27].

The misfit dislocation (MD) is another type of line defects in III-nitride semiconductors, as shown in Figure 2.12. MDs are generated due to the in-plane lattice mismatch between the neighbouring layers. As the misfit of in-plane lattice constants increases, the separation of

misfit dislocations decreases and the interface becomes incoherent. Therefore, MDs are very efficient in relieving strain.

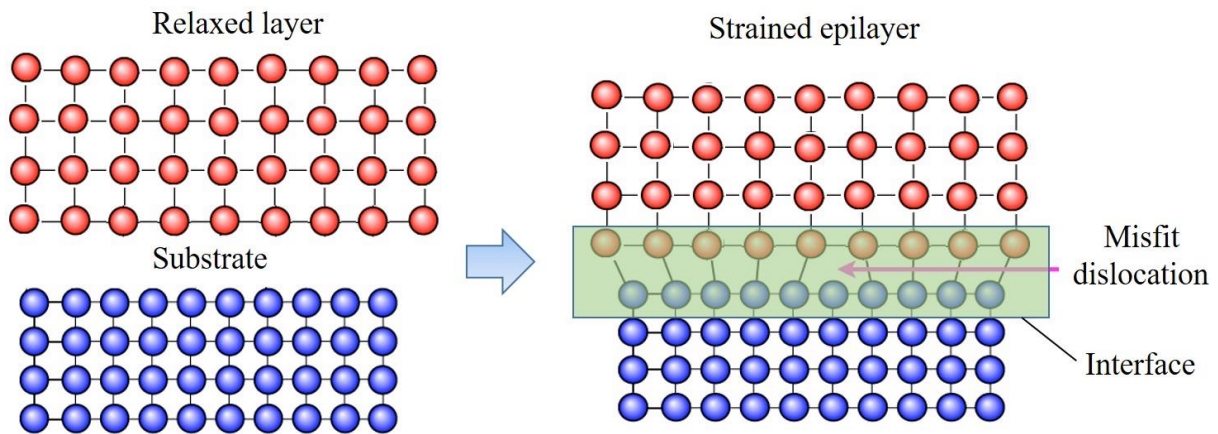


**Figure 2.12 Illustration of the misfit dislocation formation due to the lattice mismatch between the epilayer and the substrate.**

Different to TDs, MDs in  $c$ -plane films are normally confined to the heterointerfaces and are not supposed to propagate toward the surface of epilayers. However, in semi-polar or non-polar III-nitrides, the MD at the interface may connect to a TD resulting from the glide of the TD in the slip plane, i.e. the (0001) basal plane, forming a MD-TD configuration [28], as illustrated in Figure 2.13 (a). Tyagi *et al* pointed out that MDs at the (11-22) heterointerfaces are consistent with the plastic relaxation by the dislocation glide in the basal plane [29]. Also, the MDs have an in-plane Burgers vector component that relieved misfit strain, and a perpendicular component responsible for lattice tilt [30], as shown in Figure 2.13 (b).

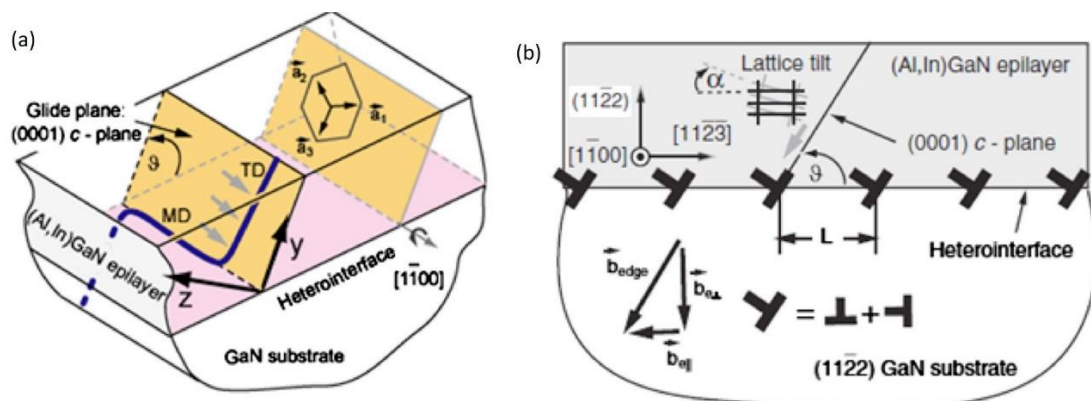


**Figure 2.13 (a) Schematic of the MD-TD configuration in the semi-polar (11-22) (Al, In)GaIn/GaN heterostructure. (b) Cross-section schematic of the edge MDs array and burgers vector decomposition into in-plane components (lattice misfit compensating) and perpendicular components (macroscopic-tilt inducing). Taken from [28].**

### 2.4.3 Stacking Faults (SFs)

Stacking faults (SFs), as a type of planar defects, are often observed in the growth of semi-polar and non-polar III-nitrides as well as the epitaxial laterally overgrowth of  $c$ -plane. Since III-nitrides can crystallize either in a hexagonal wurtzite or a cubic zinc blende structure, the formation of basal-plane stacking faults (BSFs) could be regarded as local changes from the wurtzite phase with the usual ...ABABAB... stacking sequence to the cubic phase with the usual ...ABCABCABC... stacking sequence.

Four types of BSFs can be found in wurtzite III-nitride semiconductors, as shown in Figure 2.14. The three intrinsic BSFs ( $I_1$ ,  $I_2$  and  $I_3$ ) are formed by replacing one hexagonally close-packed plane with another, i.e.  $AB \rightarrow AC$  or  $BC$ , while the extrinsic BSFs (E) result from an additional plane insertion. The displacement vectors of four BSFs are also present in Figure 2.14.

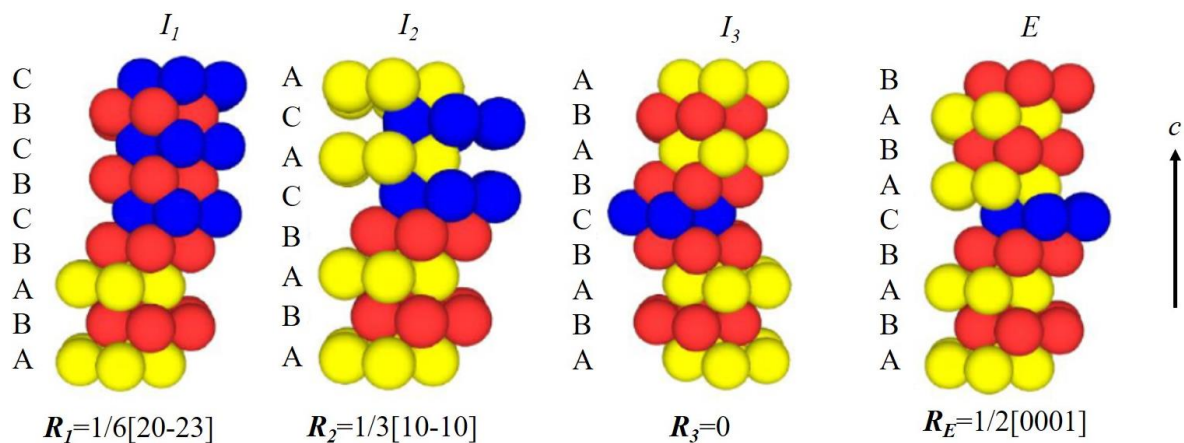


**Figure 2.14 Different stacking sequence and displacement vector in three intrinsic BSFs ( $I_1$ ,  $I_2$  and  $I_3$ ) and the extrinsic BSFs (E). Taken from [31].**

$I_1$  BSFs are formed by the insertion of an additional basal plane  $1/2 \cdot [0001]$  with a further slip of  $1/3 \cdot [1-100]$ , and bounded by Frank-Shockley partial dislocations. It is found that ~ 90% BSFs observed in III-nitrides are  $I_1$  type, which is due to their lowest formation energy.

$I_2$  BSFs are formed by a slip of  $1/3 \cdot [1-100]$  in the basal plane, and bounded by Shockley partial dislocations.  $I_3$  BSFs occur from an isolated stacking error and have no bounded dislocations. E type BSFs surrounded by Frank dislocations are much less observed experimentally as they have the highest formation energy.

Although SFs are typically bounded by different types of partial dislocations, they can also be terminated by other types of stacking faults, free surfaces or interfaces (normally the

overgrowth interfaces rather than the planar interfaces). Figure 2.15 shows images of different types of SFs in the (11-20) *a*-plane GaN epilayer taken by the transmission electron microscope.

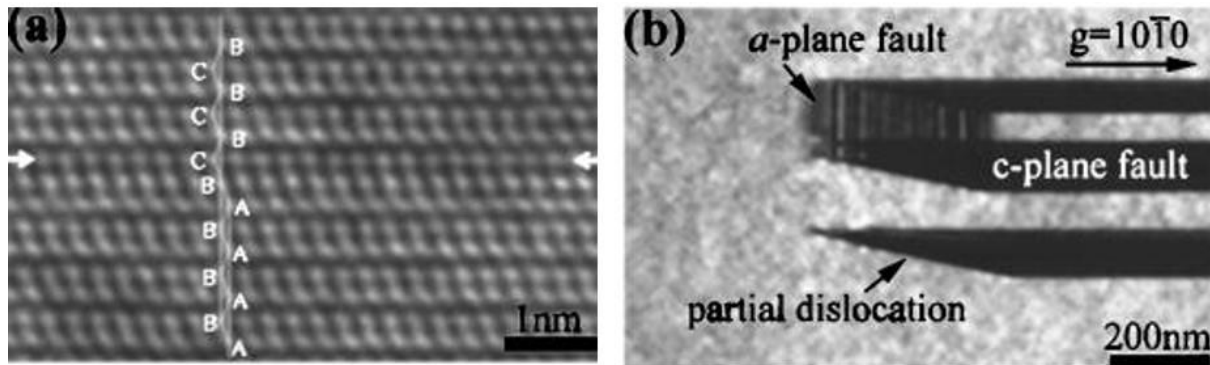


**Figure 2.15** Transmission electron microscope images of a single  $I_1$ -type BSF (a) and (b) prismatic *a*-plane SFs and partial dislocations. Taken from [32].

In addition to the basal-plane SFs, prismatic SFs (PSFs) which occur on prismatic (11-20) planes are also found in wurtzite III-nitrides. PSFs are typically bounded by two intersected  $I_1$  BSFs with stair-rod dislocations. The displacement vectors and bounded partial dislocations for different SFs are summarized in Table 2.4.

**Table 2.4** Displacement vectors, stacking sequence and bounded partial dislocations for different SFs in semi-polar and non-polar nitrides. Taken from [27].

SFs type	Displacement vector, $R$	Stacking sequence	Bounded dislocation type	Burgers vector, $b$
$I_1$	$1/6 \cdot [20-23]$	ABABCBCBC	Frank-Shockley partial	$1/6 \cdot [20-23]$
$I_2$	$1/3 \cdot [1-100]$	ABABCACAC	Shockley partial	$1/3 \cdot [1-100]$
$I_3$	None	ABABCBABA	None	None
E	$1/2 \cdot [0001]$	ABABCABAB	Frank partial	$1/2 \cdot [0001]$
Prismatic	$1/2 \cdot [10-11]$	Occurs in $\{-12-10\}$ planes	Stair rod	$1/6 \cdot [20-23]$ , $1/6 \cdot [32-50]$

## 2.5 Epitaxial Growth

### 2.5.1 Substrate and Lattice Mismatch

The crystal growth of III-nitrides can be performed either on their bulk substrates or foreign substrates, and the lattice and thermal expansion parameters for III-nitrides grown onto commonly used substrates are listed in Table 2.5.

As the free-standing substrates of both GaN and AlN are limited by the size, price and commercial availability, most researchers and companies are still focusing on heteroepitaxial growth on foreign substrates in despite of large lattice and thermal expansion mismatch.

**Table 2.5 Lattice mismatch and thermal expansion mismatch between III-nitrides and common substrates.**

Substrates	Lattice constant /Å	Lattice mismatch to GaN / %	Thermal expansion coefficient / $10^{-6}\cdot\text{K}^{-1}$	Thermal mismatch to GaN / %
GaN	$a = 3.189$	0	5.59	0
	$c = 5.185$		3.17	
AlN	$a = 3.112$	2.4	4.2	33
	$c = 4.982$		5.3	
Sapphire	$a = 4.758$	16.1	7.5	25
	$c = 12.991$		8.5	
6H-SiC	$a = 3.080$	3.5	4.2	
	$c = 15.120$		4.68	
(111) Si	$a = 5.430$	20	3.59	56

The hexagonal sapphire is the most commonly used substrate for III-nitrides epitaxy owing to its high chemical and thermal stability as well as economic cost. The growth of  $c$ -plane AlN onto a (0001) sapphire substrate is schematically shown in Figure 2.16. It can be seen that AlN grown on  $c$ -sapphire is still directed along  $c$  direction, but rotated by  $30^\circ$  around the  $c$  axis of the substrate. And the large in-plane lattice mismatch between sapphire and the AlN is clearly present. The epitaxial relationship for AlN on sapphire is (0001) AlN || (0001) Al<sub>2</sub>O<sub>3</sub> and [2-1-10] AlN || [1-100] Al<sub>2</sub>O<sub>3</sub>.

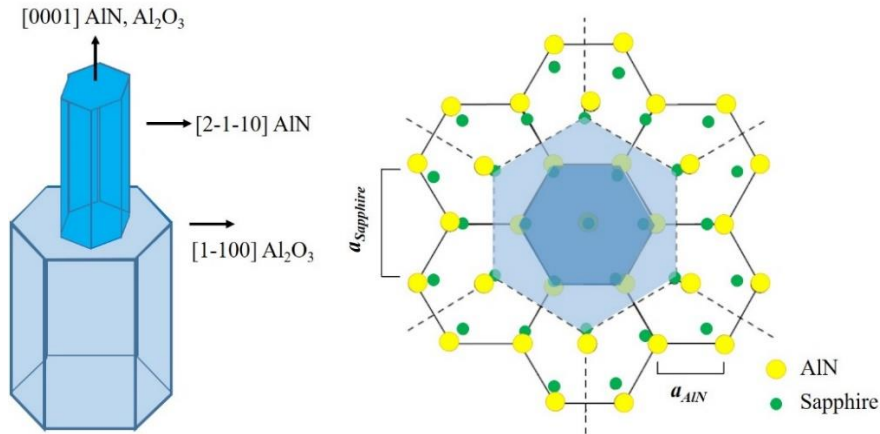


**Figure 2.16 Schematic diagram of the growth of *c*-plane AlN on *c*-plane sapphire. The in-plane direction of the AlN is rotated by 30° with respect to the sapphire.**

SiC is also used for the growth of III-nitrides due to the smaller lattice mismatch and higher thermal conductivity of substrates. However, it is limited by the high cost of the SiC wafers. III-nitrides growth has also been performed onto Si substrates as its large size can reduce the cost dramatically, whereas the even larger lattice and thermal mismatch generate high density of defects and even wafer cracking in epilayers.

### 2.5.2 Traditional Two-step Growth

In the heteroepitaxial growth of III-nitrides, a LT GaN or AlN buffer layer is normally used to obtain high quality materials. Figure 2.17 shows the typical in-situ reflectivity of the growth of *c*-plane GaN on sapphire with a LT GaN buffer layer.

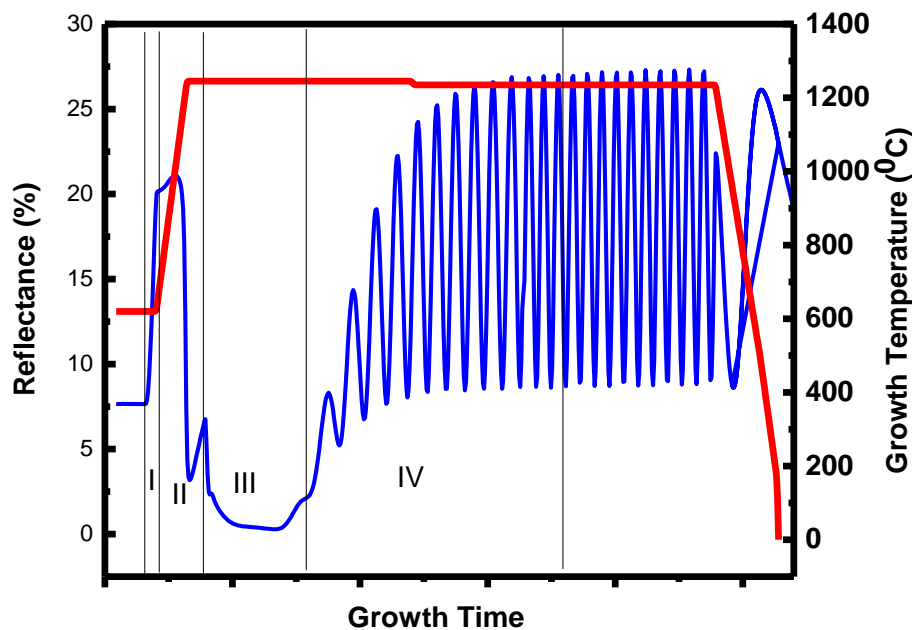


**Figure 2.17 In-situ laser reflectivity and temperature profile of the *c*-plane GaN growth with a LT GaN buffer layer.**

As shown in Figure 2.17, in the traditional two-step growth, a thin GaN nucleation layer is first deposited on the substrate at the low temperature (normally around 550°C), followed by a high temperature annealing. After the temperature is ramped to be around 1000°C, the GaN growth is started. The mechanism for this method to obtain high quality GaN could be explained by Figure 2.18.

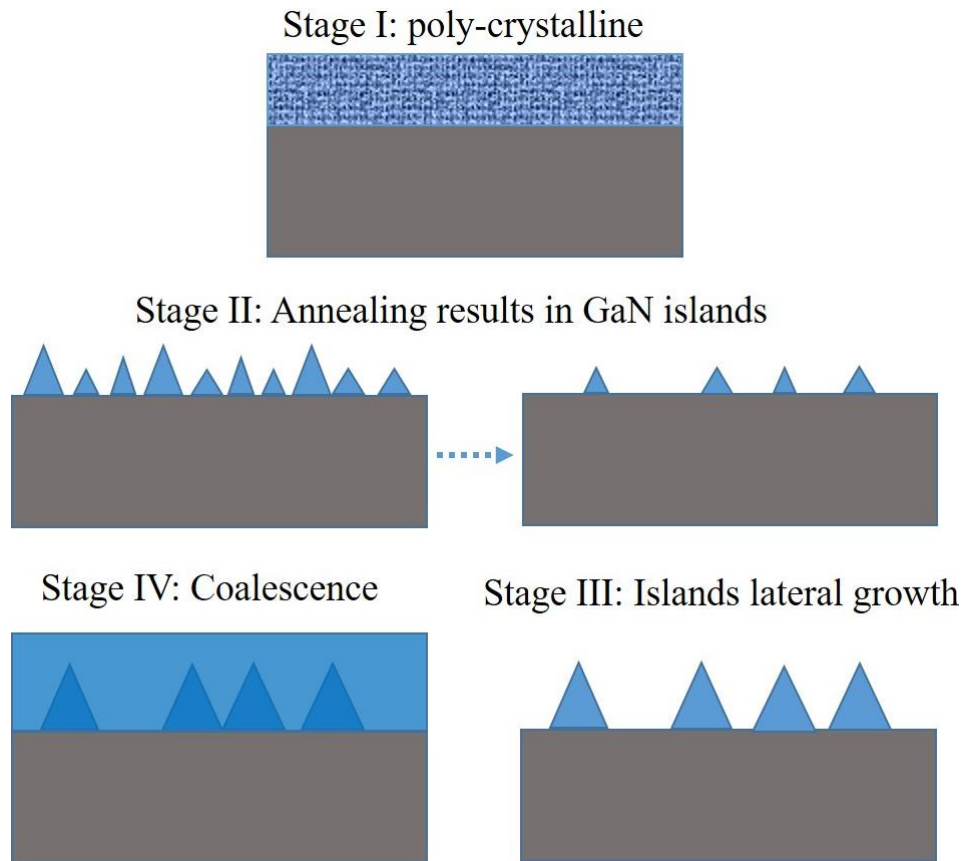


**Figure 2.18 Illustration of the traditional two-step growth process with a LT GaN buffer.**

In stage I, the LT GaN buffer layer formed is in polycrystalline phase. With high temperature annealing in stage II, the GaN layer starts to decompose and form many islands (which is also called recrystallization). With further annealing, GaN islands left on the surface become less. In the initial growth stage of GaN (stage III), the lateral growth of GaN islands occurs, followed by the complete coalescence and quasi-2D growth finally (stage IV). Since threading dislocations could be significantly reduced during the lateral growth and coalescence process, the high quality GaN epilayers are enabled [33].

### 2.5.3 Epitaxial Laterally Overgrowth (ELOG)

The epitaxial laterally overgrowth (ELOG) technique, is a powerful way to obtain GaN with low density of threading dislocations in the heteroepitaxy of III-nitrides on sapphire substrates. The key advantage of the ELOG technique is that dislocations in the epilayers under

the masks cannot propagate into the laterally overgrown epilayers, and therefore, the defect density could be considerably reduced.

By using various patterns or designs, different ELOG approaches have been proposed, such as facet-controlled ELOG [34], air-bridged ELOG [35] and grooved or striped structures [36]. With a facet-controlled ELOG technique, AlGaN-based UV LDs grown on the ELOG GaN template with an emission of 336 nm have been achieved [37].

The standard ELOG technique is illustrated in Figure 2.19.

Prior to growth the GaN template is coated by the patterned mask films (normally  $\text{SiO}_2$  or  $\text{SiN}_x$ ) which could be obtained by standard photolithography. Growth of the ELOG GaN only takes place at the window areas which are not covered by the mask. After the growth front reaches the top of masks, the lateral overgrowth process occurs, followed by the coalescence between neighbouring layers.

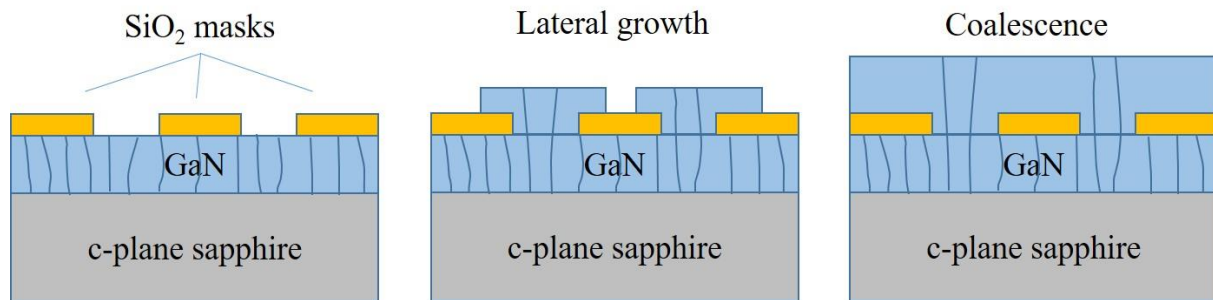


**Figure 2.19 Illustration of the standard ELOG technique. The dislocations are filtered by the patterned masks on top of GaN.**

It has been found that facet structures are normally formed during the initial stage of the ELOG growth, which plays an important role in changing the propagation orientation of threading dislocations. Dislocations tend to bend and then be terminated either by boundaries or interface, or by another dislocation, which finally results in the great reduction of the dislocation density.

Many factors could affect the structure of the ELOG GaN, such as growth temperature [38], reactor pressure [39], mask size and mask direction [40], etc.

#### 2.5.4 Semi-polar and Non-polar Growth

Research of the epitaxial growth of semi-polar and non-polar III-nitrides is far behind that of *c*-plane material. Obviously, semi-polar or non-polar nitrides could be epitaxially grown on their free-standing substrates, which can be obtained by slicing the bulk material along a semi- or non- polar direction. It is also reported that semi-polar or non- polar nitrides can be achieved by growing on the (1-102) *r*-plane or (10-10) *m*-plane sapphire using the conventional two-step

growth method [41], or on patterned Si substrates [42] using the laterally overgrowth technique. Table 2.6 summarises some foreign substrates used for semi- or non-polar nitrides growth and the epitaxial relationship for GaN on different substrates.

The epitaxial relationship in semi-polar and non-polar growth is not as straightforward as that in *c*-plane, and it normally involves multi-phases and poor surface morphology. For example, both (11-22) and (10-13) orientated GaN can be formed on the planar *m*-plane sapphire substrate which depends on the growth conditions [43].

**Table 2.6 Foreign substrates used for semi-polar and non-polar growth and their epitaxial relationship.**

Planes	Angle to <i>c</i> -axis	Foreign substrate	Epitaxial relationship
(11-20)	90°	<i>r</i> -plane sapphire	(11-20)GaN    (1-102)Al <sub>2</sub> O <sub>3</sub> [0001]GaN    [1-101]Al <sub>2</sub> O <sub>3</sub>
		<i>a</i> -plane SiC [44]	(11-20)GaN    (11-20)SiC [0001]GaN    [0001]SiC
(1-100)	90°	<i>m</i> -plane SiC [45]	
		$\gamma$ -LiAlO <sub>2</sub> [46]	(1-100)GaN    (100)LiAlO <sub>2</sub> [0001]GaN    [010]LiAlO <sub>2</sub>
(11-22)	58°	<i>m</i> -plane sapphire	(11-22)GaN    (1-100)Al <sub>2</sub> O <sub>3</sub> [-1-123]GaN    [0001]Al <sub>2</sub> O <sub>3</sub>
		patterned <i>r</i> -plane sapphire [47]	
		patterned (113) Si [48]	
(20-21)	75°	patterned (22-43) sapphire [49]	
		(114) Si with 1° offcut [50]	
(10-13)	32°	<i>m</i> -plane sapphire	(1-103)GaN    (1-100)Al <sub>2</sub> O <sub>3</sub> [11-20]GaN    [0001]Al <sub>2</sub> O <sub>3</sub>
(10-12)	43°	(001) Si with 2°-6° offcut [51]	
(10-11)	62°	(30-38) 4H-SiC [52]	
		patterned (001) Si [53]	
		patterned (11-23) sapphire [54]	

For the growth on patterned substrates, the initial growth is actually still along the conventional  $c$  direction [47-48], i.e. on the  $c$ -plane of sapphire or (111) plane of Si, and flat semi-polar surfaces are then formed after coalescence. Similar to the growth in  $c$ -plane nitrides, buffer layers (either GaN or AlN) [41], interlayers such as SiN<sub>x</sub> [55], or short-period superlattice layers [56] are also used to release the strain and improve the crystal quality of semi-polar and non-polar structures.

## References

1. Wikipedia <https://en.wikipedia.org/wiki/Semiconductor>.
2. P. Pampili and P. J. Parbrook, *Mater. Sci. Semicond. Process.* 62, 180 (2017).
3. Website <http://www-opto.e-technik.uni-ulm.de/lehre/cs/>.
4. T.-Y. Seong, J. Han, H. Amano, and H. Morkoç, *III-Nitride Based Light Emitting Diodes and Applications* (Springer, Singapore, 2017).
5. U. K. Mishra, S. Likun, T. E. Kazior, and Y. F. Wu, *Proc. IEEE* 96, 287 (2008).
6. Wikipedia [https://en.wikipedia.org/wiki/Vegard%27s\\_law](https://en.wikipedia.org/wiki/Vegard%27s_law).
7. S. R. Lee, A. F. Wright, M. H. Crawford, G. A. Petersen, J. Han, and R. M. Biefeld, *Appl. Phys. Lett.* 74, 31 (1999).
8. G. Tamulaitis, *Lith. J. Phys.* 51, 177 (2011).
9. S. Nakamura, S. Pearton, and G. Fasol, *The Blue Laser Diode: The Complete Story* (Springer-Verlag, Berlin, 2000).
10. V. Y. Davydov, A. A. Klochikhin, R. P. Seisyan, V. V. Emtsev, S. V. Ivanov, F. Bechstedt, J. Furthmüller, H. Harima, A. V. Mudryi, J. Aderhold, O. Semchinova, and J. Graul, *Phys. Stat. Sol. (b)* 229, R1 (2002).
11. H. Morkoç, *Handbook of Nitride Semiconductors and Devices* (Wiley-VCH, Weinheim, 2008).
12. J. Marini, J. Leathersich, I. Mahaboob, J. Bulmer, N. Newman, and F. Shahedipour-Sandvik, *J. Cryst. Growth* 442, 25 (2016).
13. M. Sumiya and S. Fuke, *MRS Internet J. Nitride Semicond. Res.* 9, 1 (2004).
14. A. E. Romanov, T. Baker, S. Nakamura, and J. S. Speck, *J. Appl. Phys.* 100, 023522 (2006).
15. J. E. Northrup, *Appl. Phys. Lett.* 95, 133107 (2009).
16. T. Wernicke, L. Schade, C. Netzel, J. Rass, V. Hoffmann, S. Ploch, A. Knauer, M. Weyers, U. Schwarz, and M. Kneissl, *Semicond. Sci. Technol.* 27, 024014 (2012).
17. D. D. Koleske, S. R. Lee, M. H. Crawford, M. E. Coltrin, and P. T. Fini, *Sandia Report*, June (2013).
18. J. Bai, B. Xu, F. G. Guzman, K. Xing, Y. Gong, Y. Hou, and T. Wang, *Appl. Phys. Lett.* 107, 261103 (2015).
19. Y. Tsuchiya, Y. Okadome, A. Honshio, Y. Miyake, T. Kawashima, M. Iwaya, S. Kamiyama, H. Amano, and I. Akasaki, *Jpn. J. Appl. Phys.* 44, L1516 (2005).
20. T. Akiyama, D. Ammi, K. Nakamura, and T. Ito, *Jpn. J. Appl. Phys.* 48, 110202 (2009).

21. M. Funato, A. Kaneta, Y. Kawakami, Y. Enya, K. Nishizuka, M. Ueno, and T. Nakamura, *Appl. Phys. Express* 3, 021002 (2010).
22. M. Adachi, *Jpn. J. Appl. Phys.* 53, 100207 (2014).
23. [https://commons.wikimedia.org/wiki/File:Point\\_defects\\_in\\_crystal\\_structures.svg](https://commons.wikimedia.org/wiki/File:Point_defects_in_crystal_structures.svg).
24. J. Neugebauer and C. G. Van de Walle, *Phys. Rev. B* 50, 8067 (1994).
25. S. Ito, T. Nakagita, N. Sawaki, H. S. Ahn, M. Irie, T. Hikosaka, Y. Honda, M. Yamaguchi, and H. Amano, *Jpn. J. Appl. Phys.* 53, 11RC02 (2014).
26. D. N. Zakharov, Z. Liliental-Weber, B. Wagner, Z. J. Reitmeier, E. A. Preble, and R. F. Davis, *Phys. Rev. B* 71, 235334 (2005).
27. M. A. Moram and M. E. Vickers, *Rep. Prog. Phys.* 72, 036502 (2009).
28. F. Wu, A. Tyagi, E. C. Young, A. E. Romanov, K. Fujito, S. P. DenBaars, S. Nakamura, and J. S. Speck, *J. Appl. Phys.* 109, 033505 (2011).
29. A. Tyagi, F. Wu, E. C. Young, A. Chakraborty, H. Ohta, R. Bhat, K. Fujito, S. P. DenBaars, S. Nakamura, and J. S. Speck, *Appl. Phys. Lett.* 95, 251905 (2009).
30. E. C. Young, F. Wu, A. E. Romanov, A. Tyagi, C. S. Gallinat, S. P. DenBaars, S. Nakamura, and J. S. Speck, *Appl. Phys. Express* 3, 011004 (2010).
31. S. Lazarev, PhD thesis: X-ray Investigation of Defects in III-nitrides and Their Alloys, (2013).
32. R. Liu, A. Bell, F. A. Ponce, C. Q. Chen, J. W. Yang, and M. A. Khan, *Appl. Phys. Lett.* 86, 021908 (2005).
33. D. D. Koleske, M. E. Coltrin, K. C. Cross, C. C. Mitchell, and A. A. Allerman, *J. Cryst. Growth* 273, 86 (2004).
34. K. Hiramatsu, K. Nishiyama, A. Motogaito, H. Miyake, Y. Iyechika, and T. Maeda, *Phys. Stat. Sol. A* 176, 535 (1999).
35. I. Kidoguchi, A. Ishibashi, G. Sugahara, A. Tsujimura, and Y. Ban, *Jpn. J. Appl. Phys.* 39 L453 (2000).
36. T. Detchprohm, M. Yano, S. Sano, R. Nakamura, S. Mochiduki, T. Nakamura, H. Amano, and I. Akasaki, *Jpn. J. Appl. Phys.* 40, L16 (2001).
37. H. Yoshida, Y. Yamashita, M. Kuwabara, and H. Kan, *Appl. Phys. Lett.* 93, 241106 (2008).
38. H. Miyake, A. Motogaito, and K. Hiramatsu, *Jpn. J. Appl. Phys.* 38, L1000 (1999).
39. K. Hiramatsu, *J. Phys.: Condens. Matter* 13, 6961 (2001).
40. Y. Kato, S. Kitamura, K. Hiramatsu, and N. Sawaki, *J. Cryst. Growth* 144, 133 (1994).
41. Q. Sun, B. Leung, C. D. Yerino, Y. Zhang, and J. Han, *Appl. Phys. Lett.* 95, 231904 (2009).

42. J. Bai, X. Yu, Y. Gong, Y. N. Hou, Y. Zhang, and T. Wang, *Semicond. Sci. Technol.* 30 065012 (2015).
43. T. Wernicke, C. Netzel, M. Weyers, and M. Kneissl, *Phys. Stat. Sol. (c)* 5, 1815 (2008).
44. M. D. Craven, F. Wu, A. Chakraborty, B. Imer, U. K. Mishra, S. P. DenBaars, and J. S. Speck, *Appl. Phys. Lett.* 84, 1281 (2004).
45. X. Ni, Ü. Özgüra , S. Chevtchenkoa , J. Niewa , H. Morkoça , R. P. Devatyb, and W. J. Choykeb, *Proc. of SPIE* 6894, 689420-1 (2008).
46. P. Waltereit, O. Brandt, M. Ramsteiner, R. Uecker, P. Reiche, and K.H. Ploog, *J. Cryst. Growth* 218, 143 (2000).
47. H. Furuya, N. Okada, and K. Tadamoto, *Phys. Stat. Sol. (c)* 9, 568 (2012).
48. T. Hikosaka, T. Tanikawa, Y. Honda, M. Yamaguchi, and N. Sawaki, *Phys. Stat. Sol. (c)* 5, 2234 (2008).
49. N. Okada, H. Oshita, K. Yamane, and K. Tadamoto, *Appl. Phys. Lett.* 99, 242103 (2011).
50. M. Khoury, M. Leroux, M. Nemoz, G. Feuillet, J. Zúñiga-Pérez, and P. Vennéguès, *J. Cryst. Growth* 419, 88 (2015).
51. F. Schulze, A. Dadgar, J. Bläsing, and A. Krost, *Appl. Phys. Lett.* 84, 4747 (2004).
52. S. Kamiyama, A. Honshio, T. Kitano, M. Iwaya, H. Amano, I. Akasaki, H. Kinoshita, and H. Shiomi, *Phys. Stat. Sol. (c)* 2, 2121 (2005).
53. T. Hikosaka, T. Narita, Y. Honda, M. Yamaguchi, and N. Sawaki, *Appl. Phys. Lett.* 84, 4717 (2004).
54. S. Schwaiger, I. Argut, T. Wunderer, R. Rösch, F. Lipski, J. Biskupek, U. Kaiser, and F. Scholz, *Appl. Phys. Lett.* 96, 231905 (2010).
55. J. Jeong, J. Jang, J. Hwang, C. Jung, J. Kim, K. Lee, H. Lim, and O. Nam, *J. Cryst. Growth* 370, 114 (2013).
56. K. Balakrishnan, V. Adivarahan, Q. Fareed, M. Lachab, B. Zhang, and A. Khan, *Jpn. J. Appl. Phys.* 49, 0402061 (2010).

# Chapter 3 Experimental Techniques

In this chapter, the experimental techniques used in this thesis are described, including the crystal growth technology, namely the metal organic chemical vapour deposition and characterization techniques, such as Nomarski microscope, X-ray diffraction, scanning electron microscope, cathodoluminescence and photoluminescence.

## 3.1 Metal Organic Chemical Vapour Deposition (MOCVD)



**Figure 3.1 Aixtron 3 × 2” close-coupled showerhead MOCVD system.**

### 3.1.1 Introduction

Metal organic chemical vapour deposition (MOCVD), also named metal organic vapour phase epitaxy (MOVPE), has evolved into a leading technique for production of III-V compound semiconductor optoelectronic devices and electronic devices. Owing to the achievement of high brightness blue LEDs and the large scale manufacturing potential, MOCVD technique has emerged as the leading candidate in commercial GaN based device applications [1]. It is also noteworthy that epitaxial growth using MOCVD technique now is not only limited to semiconductor areas, but has extended to many other material fields such as metals, dielectrics and multiple materials system, becoming the most significant manufacturing process of modern technologies.

Currently, several types of MOCVD reactor geometries are available in the market for mass production of GaN-based materials and devices. Three typical types of MOCVD reactors are used, which are high-speed rotation vertical reactor [2], close-coupled showerhead (CCS)

reactor [3] and planetary rotation horizontal reactor [3]. Two reactors are used in this thesis. Samples whose number begins with the letter A are grown by the Thomas Swan 3×2” vertical CCS reactor while samples with the number beginning with the letter B are grown by the Aixtron 3×2” flip-top CCS reactor shown in Figure 3.1. Note that although the main configuration of two CCS systems are similar, the chamber size as well as the heater system are actually different, which might affect the optimal growth conditions consequently. In this section, we will give a descriptive overview of the MOCVD process and present the main configurations of the MOCVD machine.

### 3.1.2 System Principle

In MOCVD system, all sources are vaporized and transported into the reactor with carrier gas. These injected gases are ultra-pure and can be finely controlled. The Figure 3.2 illustrates typical reaction steps of III-V semiconductors taking place in the MOCVD process:

1. Transport of the group III and group V precursors in the gas phase to the substrate and then diffusion through the phase interface;
2. Adsorption of molecules/atoms onto the substrate surface;
3. Migration of the molecules/atoms to crystallization zones and chemical reaction between group III and V reagents;
4. Decomposition and/or desorption of the by-products and diffusion and convection out from the boundary layer;
5. Evacuation of the by-product out from the reactor.

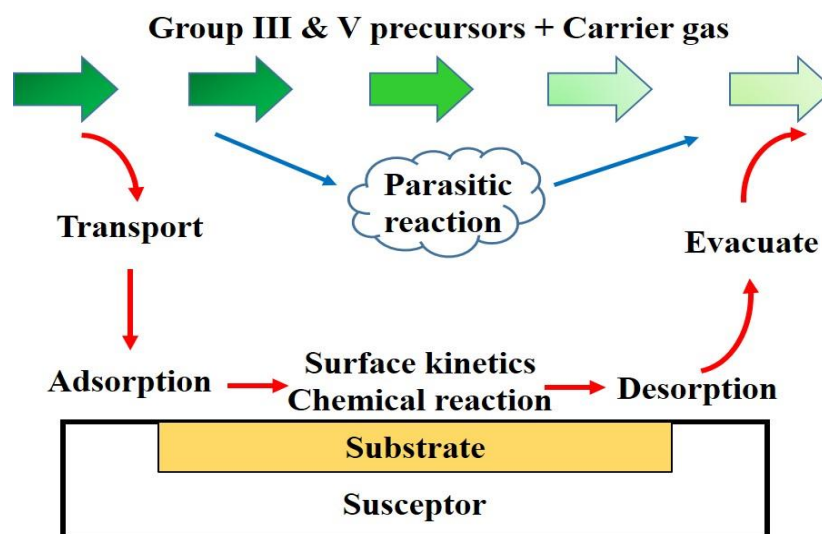


**Figure 3.2 Typical reaction steps taking place in the MOCVD reactor.**

The growth rate of thin films is mainly determined by the rate of pyrolysis and diffusion of group III sources. However, the parasitic reaction between different gas precursors such as solid adduct formation between trimethylaluminium (TMAI) and ammonia would decrease growth rate by reducing the effective flux of group III source to the substrate surface [1].

In III-nitrides MOCVD growth, metal organic (MO) compounds such as trimethylgallium (TMGa), trimethylaluminium (TMAI) and trimethylindium (TMIn) are typically used as the sources of Group III, while ammonia (NH<sub>3</sub>) is used as the source of nitrogen (Group V). For n- and p-type doping, bis(cyclopentadienyl)magnesium (Cp<sub>2</sub>Mg) is commonly used as a p-type dopant while silane (SiH<sub>4</sub>) or disilane (Si<sub>2</sub>H<sub>6</sub>) is used for n-type doping. The carrier gases are normally pure H<sub>2</sub> or pure N<sub>2</sub> or H<sub>2</sub> + N<sub>2</sub> mixed gas.

Generally, in the GaN growth, carrier gas goes through the bubbler with TMGa, carrying the TMGa vapour to the reactor where it is mixed with NH<sub>3</sub>, and then the reaction takes place on the surface of heated substrate (e.g. Sapphire or Si):



The arrow in the equation shows that solid GaN epilayers are deposited on the substrate. If TMAI is injected to the reactor in the meantime, and then AlGaN alloys could be obtained following the reaction below:



Note that the chemical reaction above only happens in the ideal situation where the parasitic reaction and the implication of temperature resulting in nonlinear incorporation of two binary alloys are not taken into account. The adduct formation between Al(CH<sub>3</sub>)<sub>3</sub> and ammonia in gas phase, which not only influences the growth rate and the alloy composition but also deteriorates the crystal quality of epilayers, could be described by following reaction [4]:



### 3.1.3 Gas Delivery

Figure 3.3 sketches a typical MOCVD gas delivery system equipped with a CCS reactor. The gas delivery system consists of carrier gases supply system, hydride supply system and MO sources supply system.

#### **Carrier gas**

The function of carrier gases is to transport reactant gases to the chamber. Both N<sub>2</sub> and H<sub>2</sub> are commonly used as carrier gas. As all gases must be ultra-pure, carrier gases normally stored in cylinders need to go through their purifiers first before injecting to the reactor.

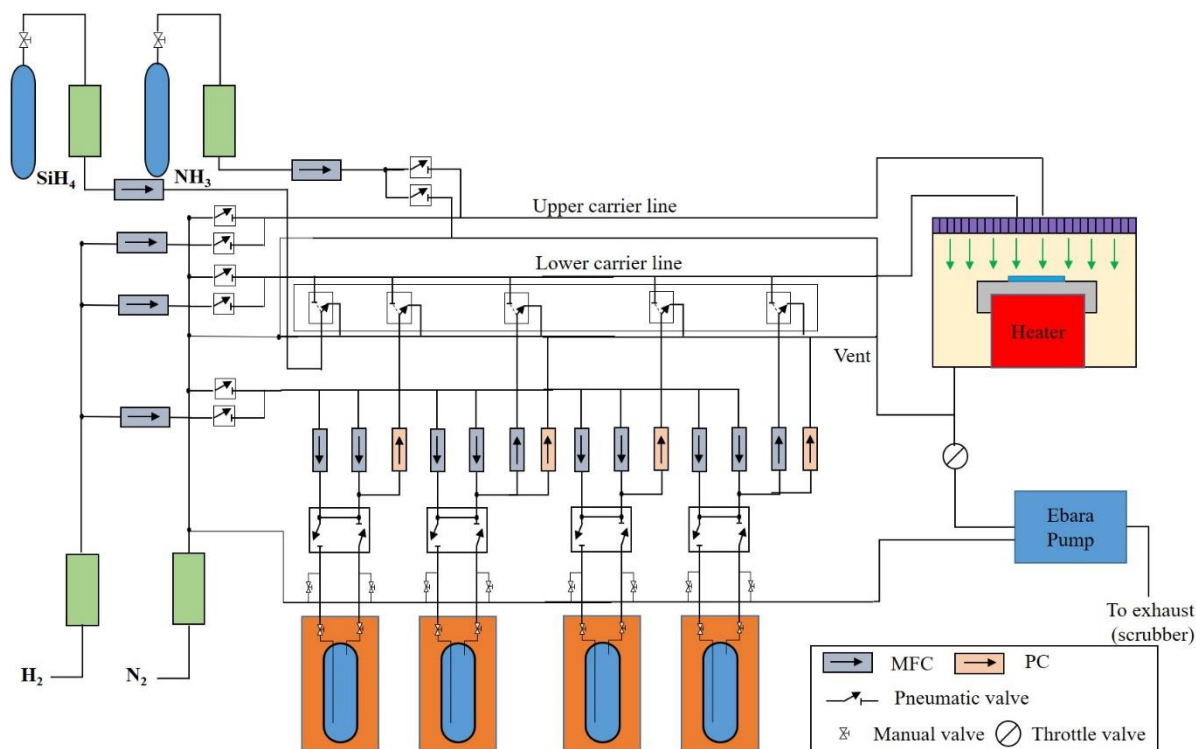


**Figure 3.3 Schematic gas diagram and showerhead reactor in a MOCVD system.**

Due to its more active chemical property,  $\text{H}_2$  is easier to be purified than  $\text{N}_2$ . Normally, palladium (Pd) membrane purifier is used for  $\text{H}_2$  purification [5], which operates on the principle of diffusion to purify hydrogen. When the process  $\text{H}_2$  flows into the Pd cell normally at  $300\sim 400^\circ\text{C}$ , only hydrogen atoms could diffuse through the Pd metal lattice to the pure side while trapped impurities are vented through the bleed gas line. Impurity levels for all impurities including  $\text{O}_2$ ,  $\text{CO}$ ,  $\text{CO}_2$ ,  $\text{H}_2\text{O}$  and  $\text{N}_2$  can be reduced to low parts per billion (ppb) levels. For  $\text{N}_2$  purification, chemically and physically adsorption purifier is normally used such as Zr-based or Ni-based gettering alloy purifiers. In addition to being used as carrier gas,  $\text{N}_2$  is often used to replace  $\text{H}_2$  within the system when unloading samples, replacing MO bubblers and performing maintenance.

### Hydride

Hydride gas, e.g.  $\text{NH}_3$ , is used as nitrogen source material. It is normally stored in high-pressure gas cylinder and special cabinet outside the system. The cylinder is normally mounted onto an electronic scale to monitor gas consumption.  $\text{NH}_3$  gas is further purified by  $\text{NH}_3$  purifier before it is fed into the reactor via a hydride gas line, as shown in Figure 3.4.

In a standard hydride gas line, a mass flow controller (MFC) is used to control the gas flow rate. The flow rate of the MFC is normally indicated using sccm (standard cubic centimetres per minute) or slm (standard litres per minute). The molar flux of  $\text{NH}_3$ ,  $n(\text{NH}_3)$  (unit: mol/min) in standard line could be calculated by:

$$n(\text{NH}_3) = f(\text{NH}_3) / V_m \quad (3.4)$$

where  $f(\text{NH}_3)$  is the  $\text{NH}_3$  flow rate (sccm) and  $V_m$  is the molar volume of an ideal gas at standard condition, which is  $22414 \text{ cm}^3/\text{mol}$ .

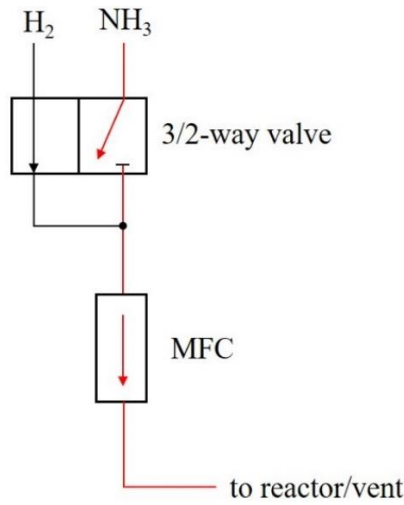


**Figure 3.4 Schematic gas line for the hydride ( $\text{NH}_3$ ) feed.**

Another hydride gas which is used as the source of silicon is  $\text{SiH}_4$  or  $\text{Si}_2\text{H}_6$ . They are normally diluted in hydrogen and stored in the high-pressure gas cylinder. In our MOCVD systems,  $\text{Si}_2\text{H}_6$  with the concentration of 10 ppm is used.

### 3.1.4 MO Sources

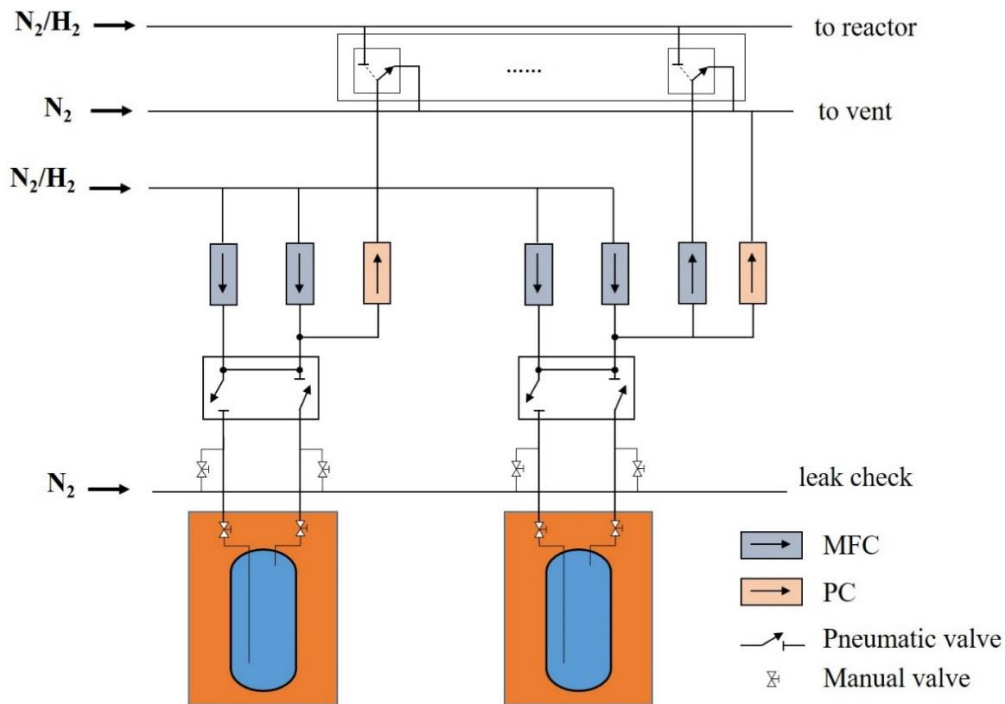


**Figure 3.5 Schematic gas diagram for MO sources with the standard line (left) and dilution source line (right).**

MO sources, either solid or liquid, are stored in the stainless steel bubblers, from which the MO vapours are picked up by the carrier gas and then delivered to the vent or reactor lines. There are two typical types of MO source channels, which are illustrated in Figure 3.5.

In a standard MO source channel, which is used for high flow MO sources such as TMAI for the deposition of AlN, two MFCs - one is source MFC and another is pusher MFC - in the inlet side are used to control the flow rate of MO source while the pressure controller (PC) in the outlet is used to control the pressure within the bubbler. For very low flow MO sources such as TMGa for the deposition of InGaN QWs, however, a dilute gas channel with a third MFC added in the outlet side is used. The proportion of the mixed gas (MO + H<sub>2</sub>) is controlled by the source MFC and dilute MFC, and the output of MO flux into the reactor is determined by the third output MFC, following the expression:

$$f(MO) = f_{inj} \times \frac{f_{so}}{f_{so} + f_{dil}} \quad (3.5)$$

where  $f(MO)$  is the flow rate of MO source injected into the reactor, and  $f_{so}$ ,  $f_{dil}$ , and  $f_{inj}$  are flow rates of source MFC, dilute MFC and inject MFC, respectively.

The concentration of MO sources in the carrier gas is also affected by the temperature and pressure of the bubblers. To achieve stable and controllable MO flux, MO bubblers are mounted in the thermostatically controlled bath (e.g. thermal bath) where the ambient temperature is kept constant, and the PC connected to the bubbler outlet is used to keep the pressure constant. The MO molar flux  $n(MO)$  (unit: mol/min) could be calculated by :

$$n(MO) = \frac{f_{MO} \times P_{MO}}{V_m \times (P_{bub} - P_{MO})} \quad (3.6)$$

where  $f_{MO}$  is the flow rate of carrier gas into the bubbler,  $P_{bub}$  is the bubbler pressure,  $P_{MO}$  is the partial pressure of MO source and  $V_m$  is 22414 cm<sup>3</sup>/mol.

**Table 3.1 Properties of the commonly used MO sources for III-nitrides growth [6-9].**

MO sources	Molecular formula	Melting point °C	Boiling point °C	Partial pressure $lgP(Torr) = B - A/T(K)$	
				A	B
TMGa	Ga(CH <sub>3</sub> ) <sub>3</sub>	-15.8	55.7	8.07	1703
TMAI	Al(CH <sub>3</sub> ) <sub>3</sub>	15.4	127	8.22	2134
TMIn	In(CH <sub>3</sub> ) <sub>3</sub>	88.4	133.8	11.09	3246
Cp <sub>2</sub> Mg	Mg(C <sub>2</sub> H <sub>5</sub> ) <sub>2</sub>	176	150/133.3Pa	25.14 - 4198/T - 2.18lnT	

Table 3.1 lists the MO sources we use for III-nitrides growth and their properties [6-9]. It can be known from this table that TMGa and TMAI are liquid sources at room temperature (RT) while TMI<sub>n</sub> and Cp<sub>2</sub>Mg are solid. Therefore, when installing the solid TMI<sub>n</sub> bubbler, the input and output sides are normally in the opposite position in order to get more stable gas flow [10]. When the carrier-gas and MO vapour gas mixture leaves the bubbler, it is strongly diluted by adding additional carrier gas. Such design is to prevent precipitation and possible deposition of the MO precursor on the inner wall of the gas lines [11]. Additionally, gas lines from outlet side of bubblers to the reactor are wrapped with heater tapes to prevent possible condensation of MO sources on the inner walls of pipes.

### 3.1.5 Close-coupled Showerhead Reactor

The reactor is the most important component for a MOCVD system. In a close-coupled showerhead design, the hydride and MO source gases are injected into the stainless steel, quartz lined reactor through a water-cooled showerhead close to the substrate. The spacing between the showerhead and susceptor could be as close as 5 ~ 25 mm (typically e.g. 11 mm). Figure 3.6 illustrates the structure of a CCS reactor, which consists of susceptor, showerhead, heater, susceptor support, quartz liner and double O-ring system.

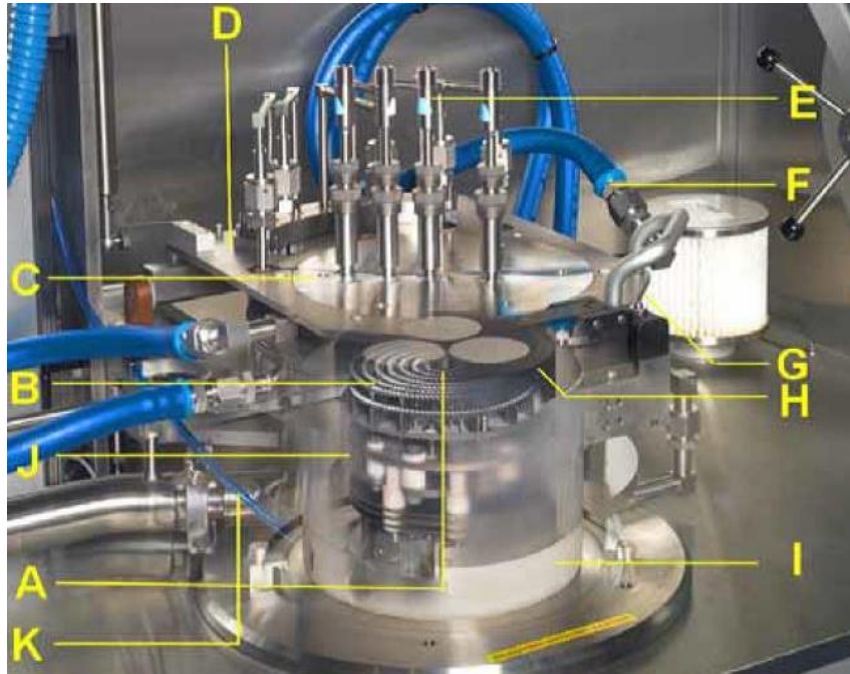


**Figure 3.6 Close-coupled showerhead reactor. The main components include: A: Thermocouple; B: Tungsten heater; C: Showerhead; D: Reactor lid; E: Optical probe; F Showerhead water cooling; G: Double O-ring seal; H: Susceptor; I: Quartz liner; J: Susceptor support; K: Exhaust. Taken from [11].**

The showerhead consists of tubes array with the density of 100 tubes/inch<sup>2</sup> and tube diameter of 0.6 mm, as shown in Figure 3.7. Inside the showerhead, it normally has two plenums: one is for group III (MO precursors) and another is for group V (NH<sub>3</sub>). The hydride and MO sources led by the carrier gas (H<sub>2</sub> or N<sub>2</sub>) are injected to the chamber through the lower and upper plenum of the showerhead, respectively, and mixed up on the top of susceptor. Both the showerhead and chamber walls are cooled by closed-cycled water loops to avoid high temperature damage.

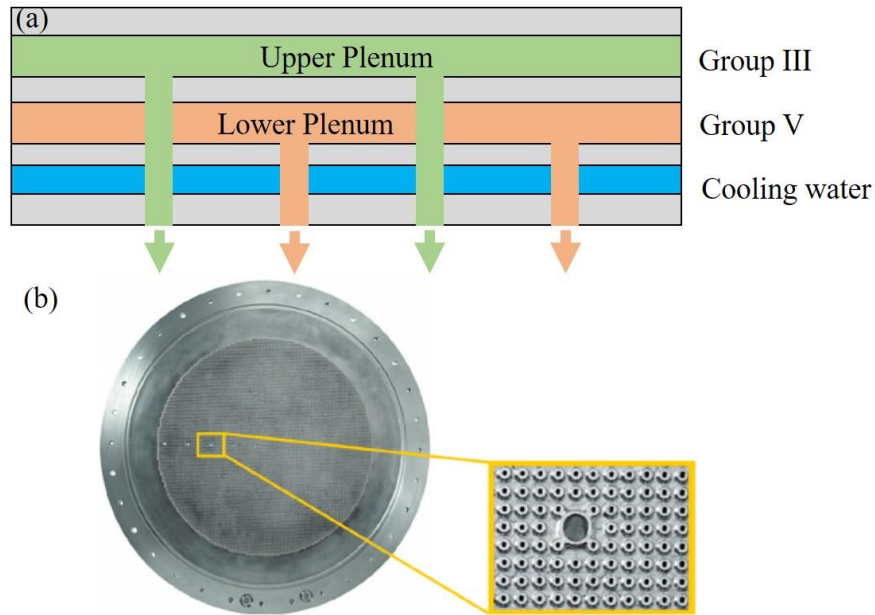


**Figure 3.7 Schematic cross-sectional structure (a) and image (b) of the showerhead. Diameter of the tubes is 0.6 mm and the density is 100 tubes/inch<sup>2</sup>. Taken from [11].**

The susceptor is generally a SiC-coated graphite disk mounted on top of susceptor support. It is rotated by a motor drive underneath to ensure homogeneous temperature during the process. The heater, which is located inside of the susceptor support, is used to heat up the susceptor to high temperature. For the GaN system, the heater consists of three sets of coils normally made of tungsten, enabling to achieve high growth temperature > 1000<sup>0</sup>C. The heater temperature is controlled by an Eurotherm temperature controller through a thermal couple located at the center of heater coils under the bottom of susceptor.

### 3.1.6 In-situ Monitoring

#### **ARGUS**

The temperature profile across the susceptor can be measured either by a pyrometer through three pyrometer ports on the showerhead (used in the Thomas Swan reactor), or by an ARGUS dual-wavelength multiple point pyrometric profiling system (used in the Aixtron

reactor). The ARGUS system shown in Figure 3.8 (a), looking through the showerhead holes, is able to provide temperature measurement across the whole surface of susceptor and allow thermal mapping of the wafer and carrier surface. Through reactor temperature correction by finely adjusting the heater zone setting, derived from the ARGUS display, wafer property profiles (e.g. thickness, emission wavelength etc.) can be significantly improved [11].

The principle of ARGUS is based on the Planck's Law in which the radiative energy distribution with respect to black body temperature is described [11]. A small amount of radiation passes through the holes in the showerhead and is collected and measured by photodetectors fixed in ARGUS. While the susceptor rotates, the whole susceptor is scanned, and a temperature map can be displayed through the system software. The ARGUS is calibrated by mounting it over a black body calibrator which is scanned across all the detectors.

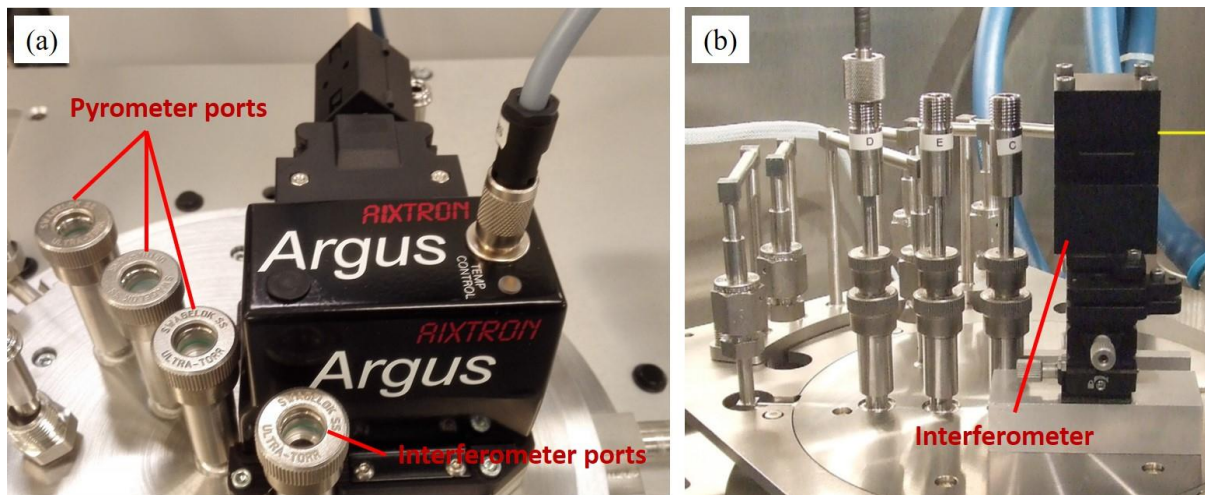


Figure 3.8 Images of the ARGUS system (a) and Interferometer (b).

### Interferometer

An interferometer or reflectometer, which is also mounted on the showerhead lid, is normally used for in-situ layer thickness and surface morphology measurement, as shown in Figure 3.8 (b).

The interferometer uses Fabry-Perot reflectance interferometry to monitor and analyze the MOCVD growth of thin-film materials [11]. When the laser light is reflected at near-normal incidence from the epilayer, an interference pattern, i.e. oscillations, resulting from the two beams reflected from the air/film and film/substrate interfaces can be observed. The thickness of epilayers equivalent to one oscillation can then be calculated by the equation below:

$$t = \lambda / 2n \quad (3.7)$$

where  $t$  is the thickness,  $\lambda$  is the laser wavelength and  $n$  is the refractive index of the epilayer.

For GaN growth, one oscillation from 635 nm laser is equivalent to 133 nm in thickness while for AlN it is 150 nm.

## 3.2 Characterization Techniques

### 3.2.1 Nomarski Microscopy

Nomarski or differential interference contrast (DIC) microscopy is an optical microscopy technique especially used for imaging the unstained and transparent samples with enhanced contrast. The mechanism could be explained as follows:

- A linearly polarized light is separated into two beams, which take slightly different optical paths when reflected by a specimen depending on its thickness and/or refractive index.
- The beams are then recombined at the image plane, where the interference may occur and can be visualized as change in darkness [12].

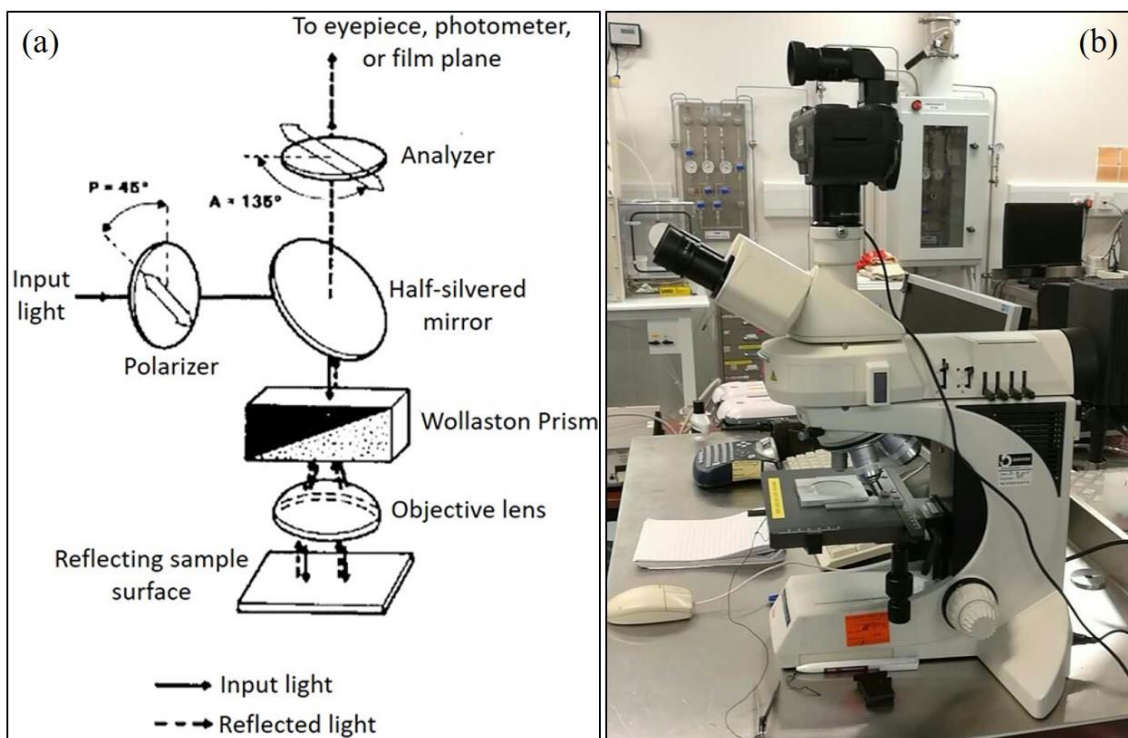


**Figure 3.9 Schematic structure and optical path in a Nomarski microscope (a) [13] and the image of the Nomarski microscope used in our lab (b).**

The optical path in a Nomarski microscope is illustrated in Figure 3.9. The light from the lamp is linearly polarized after passing through a polariser, and then separated into two orthogonal components by a Wollaston prism. The sheared orthogonal components are then reflected by the specimen before being collected by the objective lens and focused onto the

interference plane of the Wollaston prism. Recombined beams emerge from the prism and pass through the analyzer to complete their journey through the virtual Nomarski microscope. The image contrast can be modified by altering the path difference between two separate components.

### 3.2.2 X-ray Diffraction (XRD)

X-rays are electromagnetic waves with a wavelength of  $10^{-9} - 10^{-10}$  m. As the wavelength corresponds to the dimension of atomic plane interspacing in the crystals, it gives researchers an opportunity to investigate the crystalline structures with X-rays [14]. Owing to its rapid and non-destructive properties, X-ray diffraction (XRD) has become a popular technique widely used to characterize films and device structures. It can provide much structural information including lattice parameters, chemical composition, strain state of epilayers, defects information, and layer thicknesses of thin films and superlattice or QWs.

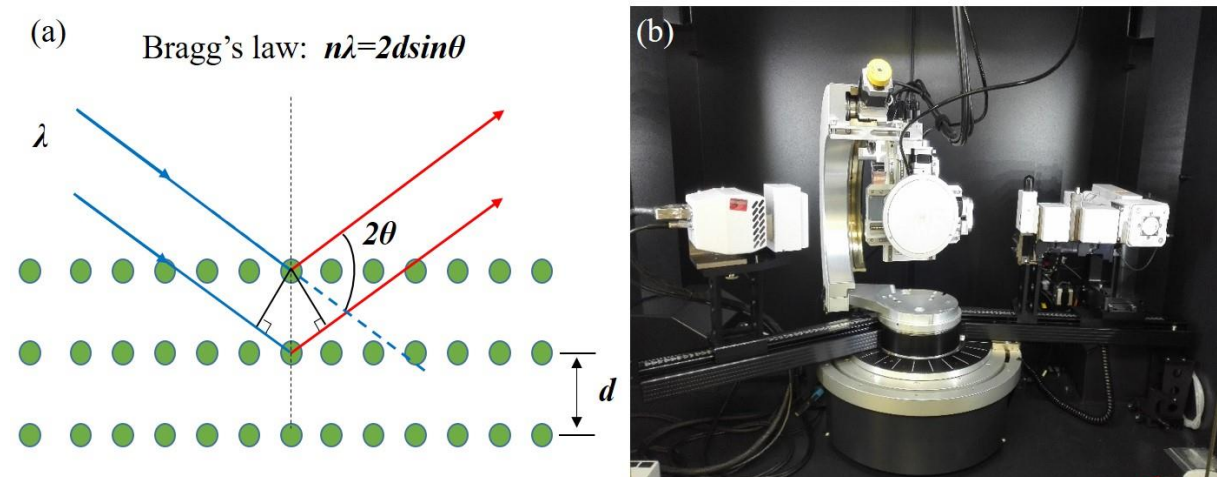


**Figure 3.10 Illustration of the X-ray diffraction with Bragg's law (a) [15] and image of the Bruker D8 diffractometer used for XRD measurements (b).**

The principle of XRD can be explained by Bragg's reflection, as depicted in Figure 3.10 (a). The incident X-ray beam is diffracted by the ordered crystalline structures, and constructive interference occurs between the scattered X-rays when the path difference  $2d \sin \theta$  is equivalent to  $n\lambda$  [15]. This can be expressed by Bragg's law:

$$n\lambda = 2d \sin \theta \quad (3.8)$$

where  $\lambda$  is the wavelength of X-ray,  $d$  is the interspacing of the atomic plane,  $n$  is an integer and  $2\theta$  is the angle of incident beam with respect to the diffracted beam normally obtained experimentally.

In a hexagonal crystal structure, the interspacing of the atomic plane ( $h k l$ ) can be calculated by their Miller indices ( $h k l$ ) and lattice parameters  $a$  and  $c$ :

$$\frac{1}{d_{hkl}^2} = \frac{4}{3} \cdot \frac{h^2 + k^2 + hk}{a^2} + \frac{l^2}{c^2} \quad (3.9)$$

### Reciprocal Space Mapping (RSM)

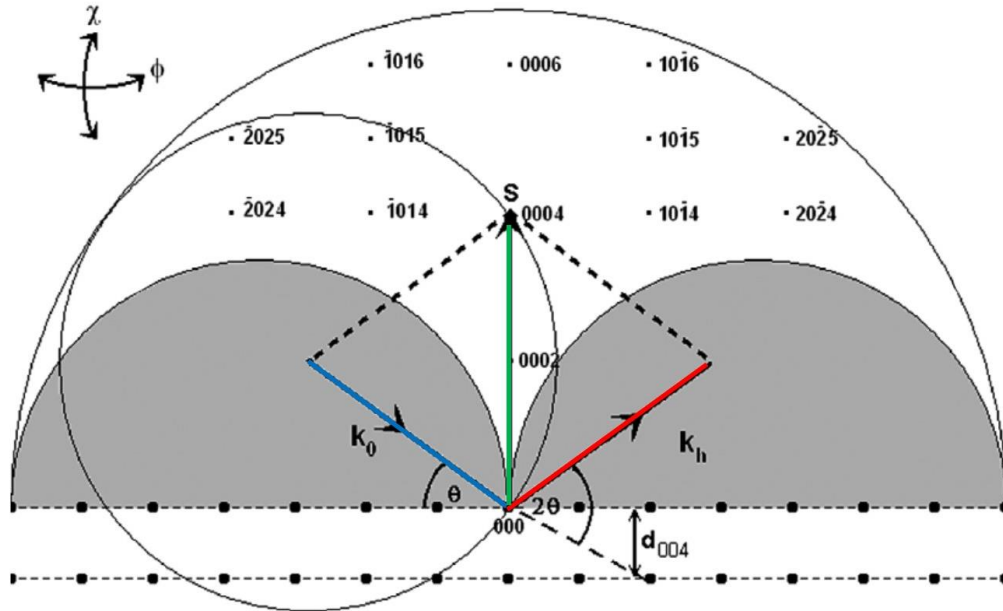


**Figure 3.11** Illustration of the X-ray diffraction in an Ewald sphere and available regions in the reciprocal space of a (0001)-oriented AlN film. Taken from [15].

X-ray diffraction can also be understood with a Ewald sphere in the context of reciprocal space, where each set of crystal planes will produce a diffraction spot associated with a reciprocal lattice point, as illustrated in Figure 3.11. When the incident beam  $k_0$  and diffracted beam  $k_h$  both have proper angles with respect to the crystal, the scattering vector  $S$  which is equal to  $k_h - k_0$  will end at a reciprocal lattice point [15].

Figure 3.11 also shows the accessible areas (or reciprocal lattice points) in  $c$ -plane AlN at a certain azimuth angle. The grey areas are inaccessible regions where either the incoming or outgoing beams are blocked by the sample in the asymmetric scans.

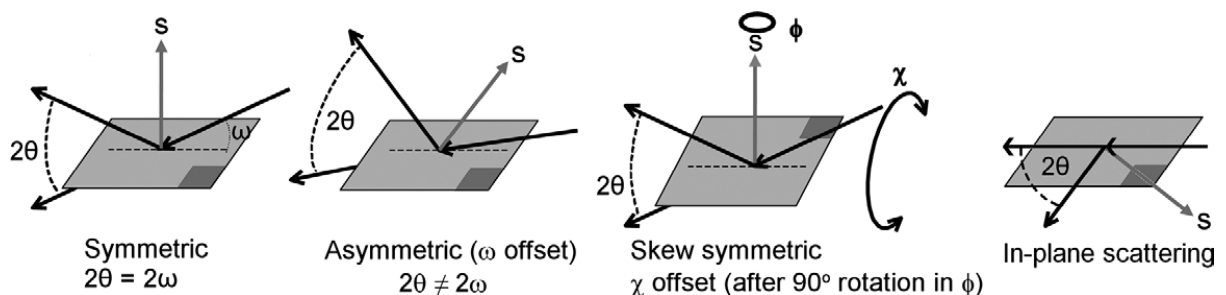


**Figure 3.12** Commonly used diffraction geometries in XRD. Taken from [15].

However, diffraction spots within the inaccessible regions may be accessible using alternative measurement geometry. As illustrated in Figure 3.12, the sample could be rotated by  $90^\circ$  in  $\phi$  and a  $\chi$  offset is used to give a skew symmetry. Also, by using very small incident angle (or scattering angle), the grazing incidence diffraction geometry (almost in-plane scattering) can be established, which is normally used to detect the diffraction spots very close to the surface.

There are three typical scan types in XRD measurements:  $\omega$  scan (also named as rocking curve),  $\omega/2\theta$  scan (or  $2\theta/\omega$  scan) and  $2\theta$  scan. In a  $\omega$  scan, the detector is fixed at a specific Bragg angle and the sample is tilted for scanning. This scan results in the change of angular positions of scattering vector  $S$  in the reciprocal space. In a  $\omega/2\theta$  scan, the step size for the  $2\theta$  angle,  $\delta 2\theta$ , has twice the value of the change in incident beam angle  $\omega$ , i.e.  $\delta 2\theta = 2\delta\omega$ , which leads to the scattering vector  $S$  scanning radially outwards from the reciprocal space origin. In a  $2\theta$  scan, the detector is moved while the incident angle is fixed. Such scan results in an arc along the Ewald sphere circumference.

The trace of scattering vector  $S$  in these scan types are illustrated in Figure 3.13 (a). Combination of different scans allow to introduce grid of detector positions around the reciprocal lattice point and yield the reciprocal space mapping (RSM) as shown in Figure 3.13 (b), which is very useful to investigate the strain state and dislocations in the crystals.

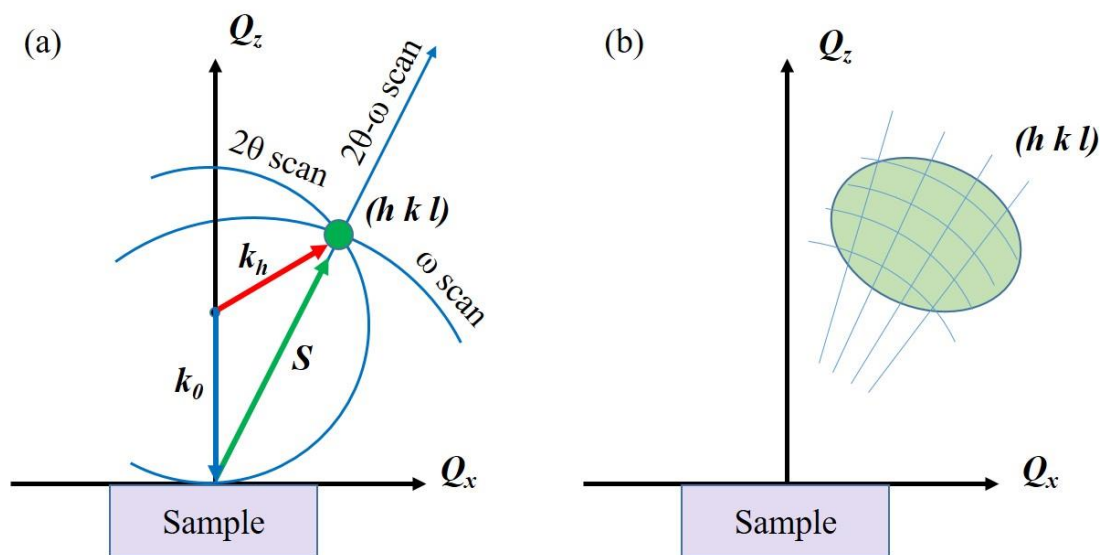


**Figure 3.13 Schematic trace of the diffraction vector  $S$  in different scan types (a) and combination of different scans in a reciprocal space map (b).**

The XRD system used in our lab is a Bruker D8 X-ray diffractometer. The X-ray with a wavelength of  $1.5418\text{\AA}$  is generated from the Cu  $K\text{-}\alpha$  radiation, and the wavelength and size of the beam is further constrained by Gobel mirrors, a monochromator crystal and a slit,

respectively. The diffracted beam is collected by either an open detector or a detector equipped with a slit or an analyzer crystal. Such configurations allow us to obtain a high-resolution of  $\sim 0.001^\circ$ .

### 3.2.3 Scanning Electron Microscopy (SEM)

The scanning electron microscope (SEM) is a type of electron microscope that uses a focused beam of high-energy electrons to produce images of a sample [16].

The SEM system used in this work is a field-emission SEM from Raith, and the structure inside the SEM column is sketched in Figure 3.14 (a). Typically, a beam of electrons is produced by an electron gun or field emission gun located at the top of the column, and then pass through several electromagnetic fields and condenser lenses, focusing the electron beam down toward the surface of the sample. When electrons hit the sample, different signals are generated from the surface and then detected by different types of detectors.

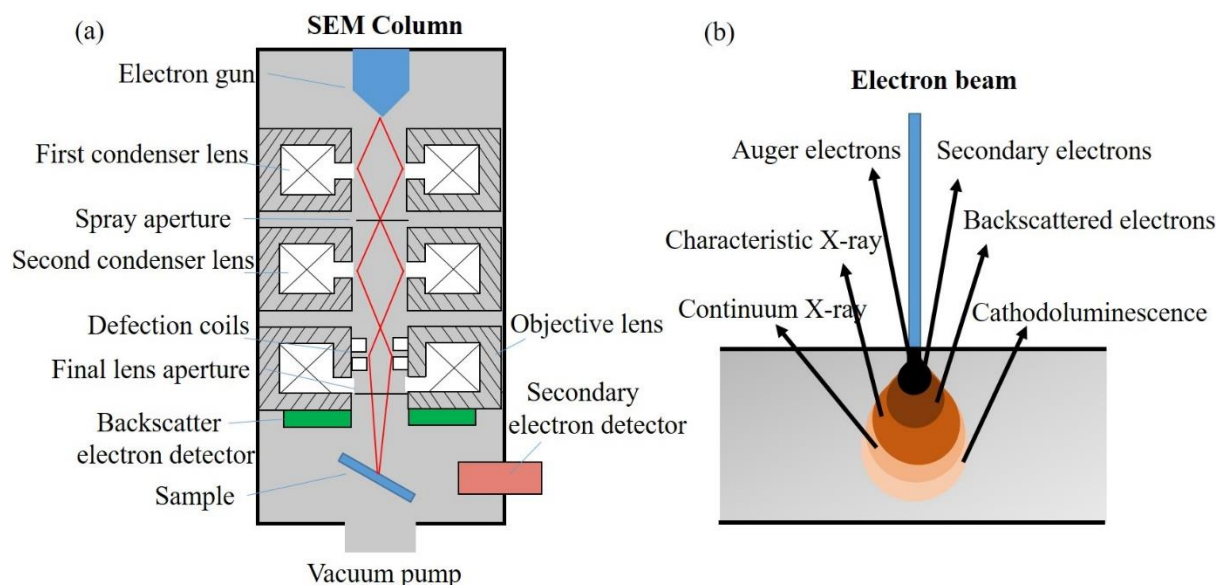


**Figure 3.14 Schematic structure of the SEM column (a) and various signals from the electron-sample interactions (b). Taken from [16].**

The signals used by a SEM to create images derive from electron-sample interactions [9], which reveals information about the sample surface topography as well as the chemical composition. Various types of signals, such as auger electrons, secondary electrons, backscattered electrons and characteristic X-rays, can be produced as a result of the electron-sample interaction, as shown in Figure 3.14 (b). The most commonly used signals in a SEM are secondary electrons and backscattered electrons. While secondary electrons are most useful

for revealing the morphology and topography of samples, backscattered electrons are most valuable for illustrating composition contrasts in samples with multiple phases [16].

The highest resolution of a SEM depends on several factors, such as the spot size of the electron beams and the interaction volume between electrons and samples. Typically, modern full-sized SEMs are able to provide resolution between 1-20 nm whereas desktop systems provide a resolution of ~20 nm [16].

#### 3.2.4 Cathodoluminescence (CL)

Cathodoluminescence (CL) is the emission of light when a material is stimulated by a high-energy electron beam. As shown in Figure 3.14 (b), electron-sample interactions can generate cathodoluminescence. A cathodoluminescence detector normally attached to a SEM, termed as SEM-CL, is capable of producing high resolution CL images of materials. SEM-CL has become a unique tool to characterize the optical and electronic properties of materials, then correlate them with morphology, microstructure, composition and chemistry at the micro- and sub-nanoscale [17].

The CL measurements are carried out in this work using a field-emission gun SEM equipped with a 0.125 m spectrometer and electron multiplying charge-coupled detector (CCD) and using a Cassegrain reflecting objective to collect luminescence down to 200 nm. Measurements of CL are performed by collaborators from the University of Strathclyde whereas the data is analysed by both sides.

#### 3.2.5 Photoluminescence (PL)

Photoluminescence (PL) is a type of luminescence that involves the absorption and then emission of photons between different electronic energy levels in the material. It is initiated by photo-excitation (normally excited by lasers), followed by various relaxation processes in which other photons are re-radiated.

PL spectroscopy is a non-contact and non-destructive analysis method which has been widely used to investigate the optical properties of materials. It is particularly useful for the determination of certain impurities in semiconductors [18]. For instance, the peak energy of PL can be used to probe the energy level of impurities and the emission intensity depends on the defects or doping density. However, measurement of the impurity concentration by using PL is difficult.

PL can be also used to determine the band gap energy of semiconductors as well as the alloy composition, though other factors such as strain, electric field and compositional

fluctuation should be taken into account when doing so. In addition, the PL intensity and linewidth could be used as an indicator of the material quality [19].

The mechanism of PL can be explained by the multiple recombination processes within the material. According to the fact if there are photons emission, the recombination process can be classed into non-radiative and radiative, which are two opposite and competitive processes. There are two types of non-radiative recombination process, Shockley-Read-Hall recombination (recombination through defects) and Auger recombination (recombination involves three carriers), neither of which has photon emission. For radiative recombination, however, they emit photons through several possible transition paths [20], as shown in Figure 3.15. They are (a) band-to-band transition, which involves free electrons and holes, (b) free exciton (FX) transition, (c) Donor-bound exciton ( $D^0X$ ) recombination, (d) Acceptor-bound exciton ( $A^0X$ ) recombination and (e) Donor-acceptor pairs (DAP) recombination.

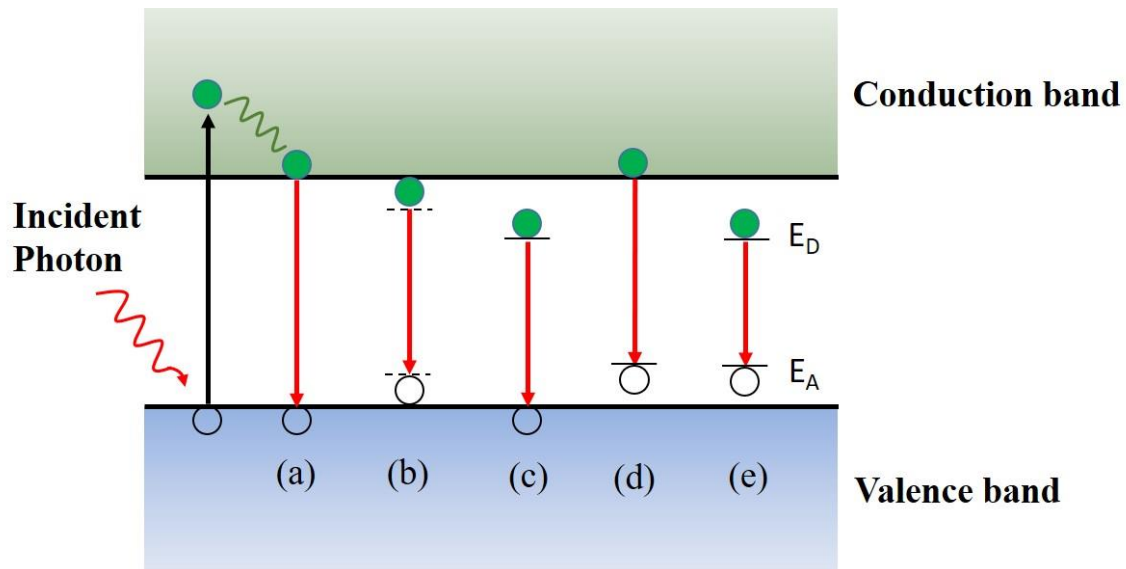


**Figure 3.15 Possible transition mechanisms in the radiative recombination: Band-to-band transition (a); FX transition (b);  $D^0X$  recombination (c);  $A^0X$  recombination (d) and DAP recombination (e).**

Figure 3.16 illustrates the setup of the PL system in this work. The excitation source used for AlGaIn layers is a doubled-frequency Argon ion laser (244 nm, Coherent) while a He-Cd laser (325 nm, Kimmon) is used for GaN layers. The laser beam is reflected by mirrors and then focused by a lens into a spot with a diameter of 100 ~ 200  $\mu\text{m}$  on the sample surface. The photoluminescence is then collected into a monochromator, and further analysed by a thermoelectrically cooled CCD detector.

To perform LT and temperature-dependent PL measurements, samples are held in a helium closed-circuit cryostat where the temperature can be controlled from 10 to 300 K. For

power-dependent PL measurements, a neutral density attenuator is normally used to tune the excitation power continuously.

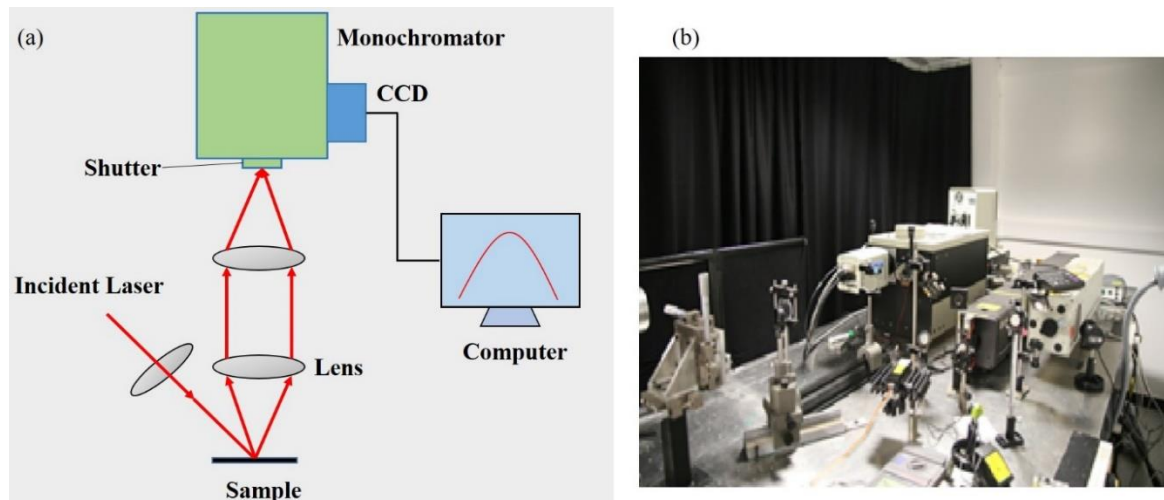


**Figure 3.16 Schematic setup of a PL system (a) and the PL bench used in this work (b).**

### **Photoluminescence excitation**

Photoluminescence excitation (PLE) is a specific type of photoluminescence and an useful method to reveal information of the electronic band gap of semiconductors. In the PLE measurement, the energy of excitation source is varied while the detection energy for the photoluminescence is fixed. This provides information on absorption properties of materials but with improved signal-to-noise ratio compared to conventional absorption measurements in transmission geometry [21]. Typical applications of PLE spectroscopy in semiconductors include the characterization of the effective band gap, i.e. the absorption edge, and the Stokes shift, which is defined as the energy difference between the maxima of absorption and emission spectra.

The experimental setup of a PLE system is quite similar to the standard PL system apart from the excitation source part. Normally a Xenon lamp (or a broadband laser-driven light source in this work) is used as the tunable light source dispersed by a monochromator. The PL is disperse by another monochromator and then collected by a photomultiplier tube (PMT). The detection energy is usually fixed at the PL peak position which is studied.

## References

1. S. J. Pearton, GaN and related materials II (Gordon & Breach, Amsterdam, 1999).
2. R. C. Walker, A. G. Thompson, G. S. Tompa, P. A. Zawadzki, and A. Gurary, Proc. SPIE 2364, Second International Conference on Thin Film Physics and Applications (1994).
3. [https://www.aixtron.com/fileadmin/documents/Brochures/How\\_MOCVD\\_works.pdf](https://www.aixtron.com/fileadmin/documents/Brochures/How_MOCVD_works.pdf).
4. T. G. Mihopoulos, V. Gupta, and K. F. Jensen, J. Cryst. Growth 195, 733 (1998).
5. Wikipedia [https://en.wikipedia.org/wiki/Hydrogen\\_purifier](https://en.wikipedia.org/wiki/Hydrogen_purifier).
6. [https://www.akzonobel.com/hpmo/system/images/AkzoNobel\\_TMGa%20SSG\\_hpmo\\_glo\\_eng\\_pds\\_tcm36-18136.pdf](https://www.akzonobel.com/hpmo/system/images/AkzoNobel_TMGa%20SSG_hpmo_glo_eng_pds_tcm36-18136.pdf).
7. [https://www.akzonobel.com/hpmo/system/images/AkzoNobel\\_TMAI%20SSG\\_hpmo\\_glo\\_eng\\_pds\\_tcm36-18134.pdf](https://www.akzonobel.com/hpmo/system/images/AkzoNobel_TMAI%20SSG_hpmo_glo_eng_pds_tcm36-18134.pdf).
8. [https://www.akzonobel.com/hpmo/system/images/AkzoNobel\\_TMIn%20SSG\\_hpmo\\_glo\\_eng\\_pds\\_tcm36-18135.pdf](https://www.akzonobel.com/hpmo/system/images/AkzoNobel_TMIn%20SSG_hpmo_glo_eng_pds_tcm36-18135.pdf).
9. [https://www.akzonobel.com/hpmo/system/images/AkzoNobel\\_Cp2Mg%20SSG\\_hpmo\\_glo\\_eng\\_pds\\_tcm36-18205.pdf](https://www.akzonobel.com/hpmo/system/images/AkzoNobel_Cp2Mg%20SSG_hpmo_glo_eng_pds_tcm36-18205.pdf).
10. R. Odedra, A. J. Kingsley, T. Leese, A. Purdie, K. M. Coward, L. M. Smith, S. A. Rushworth, G. Williams, and R. K. Kanjolia, 16<sup>th</sup> International Conference on Indium Phosphide and Related Materials (2004).
11. AIXTRON 3×2 FT CCS System Manual (2013).
12. J. S. Hartman, R. L. Gordon, and D. L. Lessor, Appl. Optics 19, 2998 (1980).
13. D. L. Lessor, J. S. Hartman, and R. L. Gordon, J. Opt. Soc. Am. 69, 357 (1979).
14. J. Als-Nielsen and D. McMorrow, Elements of Modern X-ray Physics 2<sup>nd</sup> edition (Wiley, 2011).
15. M. A. Moram and M. E. Vickers, Rep. Prog. Phys. 72, 036502 (2009).
16. Wikipedia [https://en.wikipedia.org/wiki/Scanning\\_electron\\_microscope](https://en.wikipedia.org/wiki/Scanning_electron_microscope).
17. Website <http://www.gatan.com/techniques/cathodoluminescence>.
18. H. B. Bebb and E. W. Williams, Photoluminescence I: Theory in Semiconductors and Semimetals (R. K. Willardson and A. C. Beer, eds.). New York: Academic Press (1972).
19. J. E. Toney, Photoluminescence Spectroscopy in Characterization of Materials, (John Wiley & Sons, 2002).
20. Goldberg, Luminescence of Inorganic Solids. New York: Academic Press (1966).
21. Wikipedia [https://en.wikipedia.org/wiki/Photoluminescence\\_excitation](https://en.wikipedia.org/wiki/Photoluminescence_excitation).

# Chapter 4 Epitaxial Growth of Semi-polar (11-22) AlGaN on Planar Substrates

## 4.1 Introduction

Al-containing (Al, Ga, In)N alloy semiconductors are promising candidates for UV emitters due to their wide and direct band gaps. However, AlGaN-based devices grown in *c*-plane normally suffer from strong spontaneous and piezoelectric fields, which decreases the optical efficiency. Therefore, more and more researchers shift their interest to semi-polar or non-polar orientations, in which the polarization electric fields are expected to be significantly reduced or completely eliminated.

So far, most studies on the epitaxial growth of III-nitrides on *m*-plane sapphire substrate focus on semi-polar (11-22) GaN and InGaN materials, which are mainly used for visible LEDs and LDs [1-2]. For high efficiency UV emitters, semi-polar AlGaN epilayers with different Al compositions are required. However, reports about epitaxial growth of semi-polar AlGaN are quite limited [3-4], and studies on semi-polar AlGaN MQWs are even less [5].

In this chapter, semi-polar (11-22) AlGaN epilayers with different Al composition grown on planar (10-10) *m*-plane sapphire are obtained by MOCVD with a standard growth method. The surface morphology, crystal quality and optical properties of (11-22) AlGaN epilayers are investigated. Furthermore, semi-polar AlGaN MQWs with various QW thicknesses grown on the standard AlGaN templates are studied to investigate the QCSE. Based on the excitation-power dependent PL measurements, the QCSE within semi-polar AlGaN MQWs is found to be significantly reduced.

## 4.2 Semi-polar (11-22) AlGaN Epilayer Growth

### 4.2.1 Growth Parameters

Semi-polar (11-22) AlGaN layers are grown on the (10-10) *m*-plane sapphire substrates

using MOCVD with the AlN and GaN buffers, respectively. Series A is directly grown in m-sapphire while series B is grown on the prepared GaN templates. The structure of these two series of AlGaN samples is illustrated in Figure 4.1.

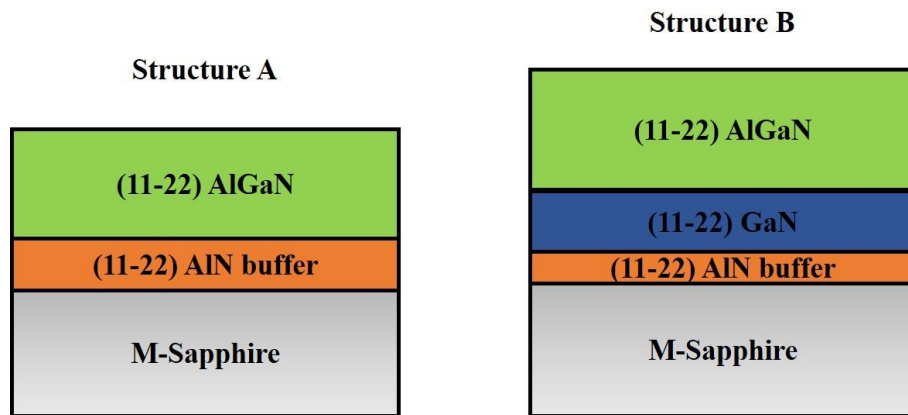


**Figure 4.1 Sample structure A: AlGaN/AlN/m-sapphire; B: AlGaN/GaN/AlN/m-sapphire.**

Details of the growth parameters are listed in Table 4.1. The AlN buffer layer with a thickness of 250 nm for structure A and 50 nm for B is obtained with the high-temperature AlN buffer technique [6]. The thickness of AlGaN layers is  $\sim 2 \mu\text{m}$  and  $\sim 500 \text{ nm}$  for structure A and B, respectively. The Al content of AlGaN samples is changed by varying the flow rates of either  $\text{NH}_3$ , TMGa or TMAI. Note that two series of AlGaN samples are grown in two different MOCVD CCS reactors, therefore the growth parameters are slightly different. The temperature presented in this thesis is surface temperature which derives from the calibration of pyrometer in the Thomas Swan reactor while it is directly from the ARGUS reading in the Aixtron reactor.

**Table 4.1 Growth parameters for the structure A and B.**

<b>A</b>	Temp. $^{\circ}\text{C}$	Press. torr	$\text{NH}_3$ mmol/min	TMGa $\mu\text{mol}/\text{min}$	TMAI $\mu\text{mol}/\text{min}$	PL@RT nm	Gas phase Al%
<b>A1</b>	1040	65	134	98.4	13.9	323	12%
<b>A2</b>	1040	65	134	86.1	15.3	318	15%
<b>A3</b>	1060	65	134	73.8	16.7	310	18%
<b>A4</b>	1060	65	134	61.5	18.1	303	23%
<b>A5</b>	1060	65	134	61.5	18.1	300	23%
<b>B</b>							
<b>B1</b>	1045	75	67	66.4	18.9	309	22%
<b>B2</b>	1060	75	45	54.1	36.2	278	40%
<b>B3</b>	1060	75	45	49.2	37.6	273	43%
<b>B4</b>	1070	75	45	49.2	37.6	273	43%
<b>B5</b>	1070	75	45	44.3	37.6	268	45%
<b>B6</b>	1070	75	45	40.6	37.6	265	48%
<b>B7</b>	1070	75	45	35.7	37.6	261	51%

The typical in-situ reflectivity of semi-polar AlGaN growth are shown in Figure 4.2. The almost constant amplitude of reflectance oscillations are exhibited, which indicates a 2D growth mode with homogeneous growth rate.

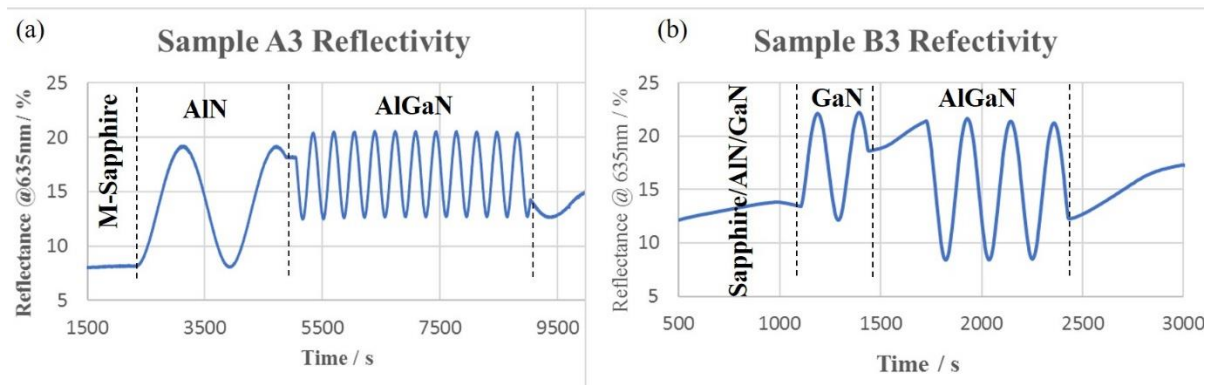


**Figure 4.2 In-situ reflectivity of sample A3 (a) and B3 (b), showing constant amplitude of oscillations.**

The growth rates extracted from the reflectivity oscillations exhibit a linear relationship with the total flux of MO precursors (TMAI + TMGa) for both structures, as shown in Figure 4.3. The difference of growth rates between two structures mainly derives from two different MOCVD reactors, which is not the topic discussed here.

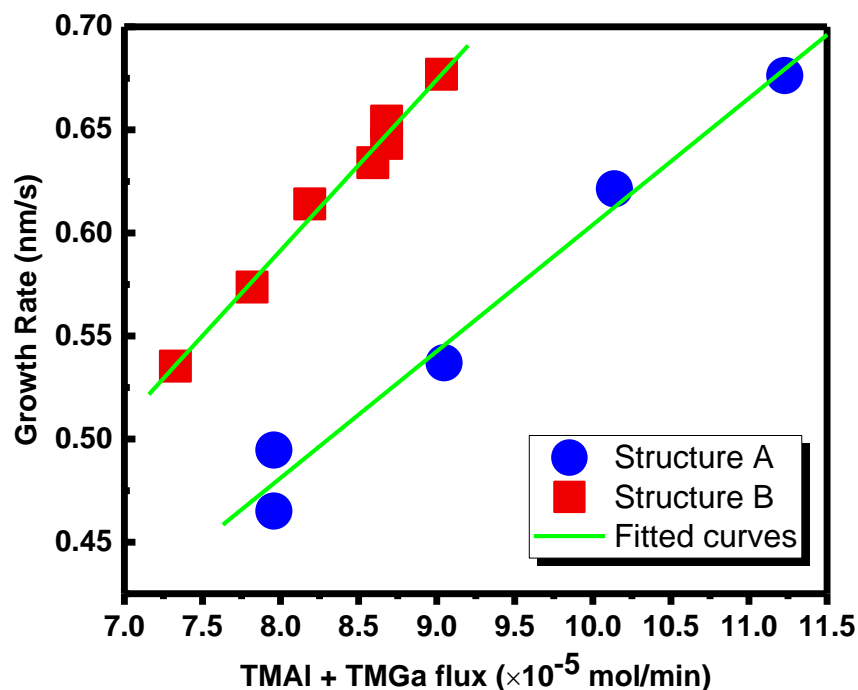


**Figure 4.3 Growth rate of the semi-polar (11-22) AlGaN layers with two different structures as a function of TMAI + TMGa flux.**

#### 4.2.2 Structural Characterization

The surface morphology of AlGaN samples is characterized by Nomarski optical microscope, as shown in Figure 4.4. Serious wafer cracking orientated along [11-2-3] direction is observed on all samples with structure B (typical cracking image is shown in Figure 4.4 (d)), while slightly cracking particularly in the edge part observed in the structure A. Such cracking issue in AlGaN-on-GaN samples is due to the tensile strain within the epilayers and will become more severe when the Al composition is higher. The density of cracking, which is roughly estimated by counting the lines along the m-direction, is from  $\sim 40 \text{ cm}^{-1}$  in B1 to  $\sim 100 \text{ cm}^{-1}$  in B5. But the cracking suffered by AlGaN-on-AlN samples might be attributed to other factors, e.g. the non-uniformity of temperature profile. It has been known that wafer cracking could result in serious problems in device fabrication and finally deteriorate the device performance.

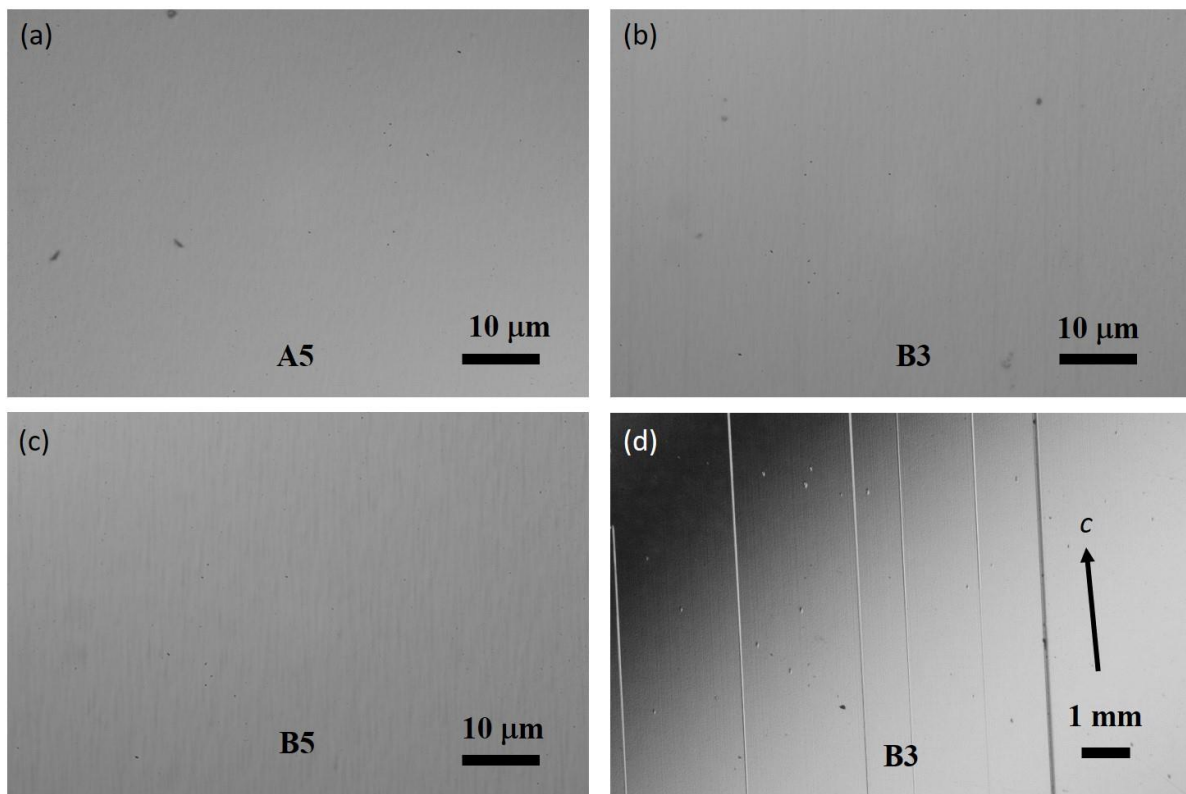


**Figure 4.4 1000X optical images of standard (11-2-2) AlGaN samples A5 (a), B3 (b) and B5 (c), and 50X image showing cracking along [11-2-3] in sample B3 (d).**

Apart from the cracks, we can see that either with AlN buffer or GaN buffer, semi-polar (11-2-2) AlGaN layers with different Al content could form smooth surface, which correlates well with a flat oscillation observed in in-situ reflectivity shown in Figure 4.2. However, very weak arrow-like features are also observed, which become pronounced in high-Al-content

AlGa<sub>N</sub> samples. Such arrow-like features are very common in semi-polar epilayers owing to the special growth mechanism (*c*-direction grows faster), and have been observed by many other groups [7-8].

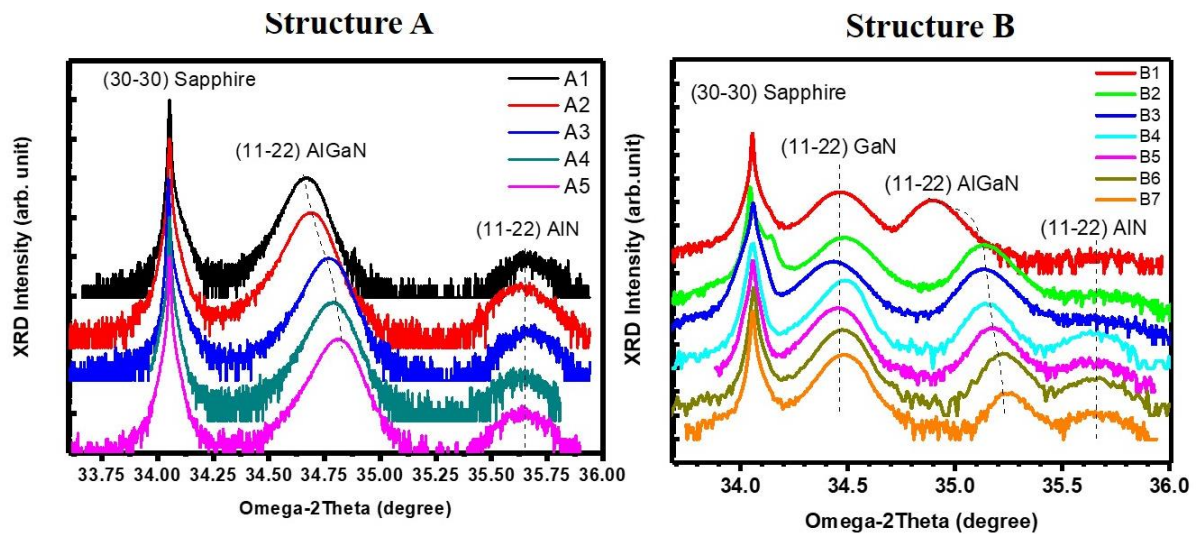


**Figure 4.5 XRD  $\omega/2\theta$  scans for all the standard AlGa<sub>N</sub> samples.**

The  $\omega/2\theta$  scans for all standard AlGa<sub>N</sub> samples are carried out and shown in Figure 4.5. Diffraction peaks from (30-30) sapphire, (11-22) AlN, GaN and AlGa<sub>N</sub> can be clearly recognised. While the peak positions of sapphire, GaN and AlN are almost constant, the AlGa<sub>N</sub> peaks shift with the changing of Al content. Some deviations observed for GaN or AlN peaks could be attributed to different strain state and/or layer tilt in AlGa<sub>N</sub> samples.

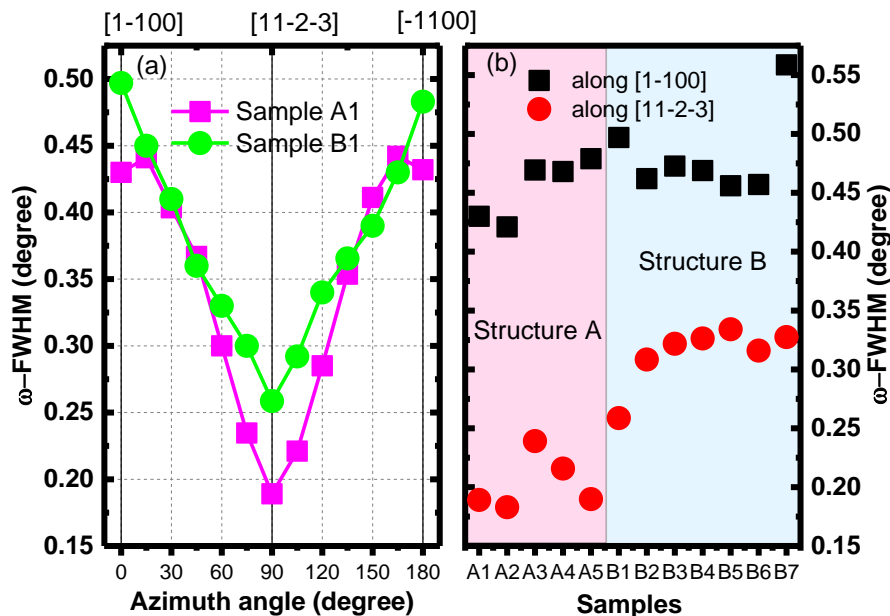


**Figure 4.6 (a) Azimuth dependent XRD rocking curve FWHMs for sample A1 and B1. (b) FWHMs of XRD rocking curve along [1-100] and [11-2-3] directions for all samples.**

The (11-22) on-axis rocking curve measurements are also performed to check the crystal quality. The full width at half maximum (FWHM) of rocking curves measured along different azimuth angles for all samples exhibits the anisotropic behaviour, as shown in Figure 4.6 (a) where the data of two typical samples, i.e. A1 and B1, is presented. The FWHM along two primary in-plane directions for all samples is shown in Figure 4.6 (b). It can be seen that the average FWHM is  $0.4\text{-}0.5^\circ$  along [1-100] direction and  $0.2\text{-}0.3^\circ$  along [11-2-3] direction, although they strongly depend on the Al content and layer thickness (note that AlGa<sub>N</sub> thickness in series A and B is different). These values are quite typical for semi-polar AlGa<sub>N</sub> layers grown on planar templates or substrates [9-11], but they are far away from satisfaction for UV devices.

#### 4.2.3 Optical Properties

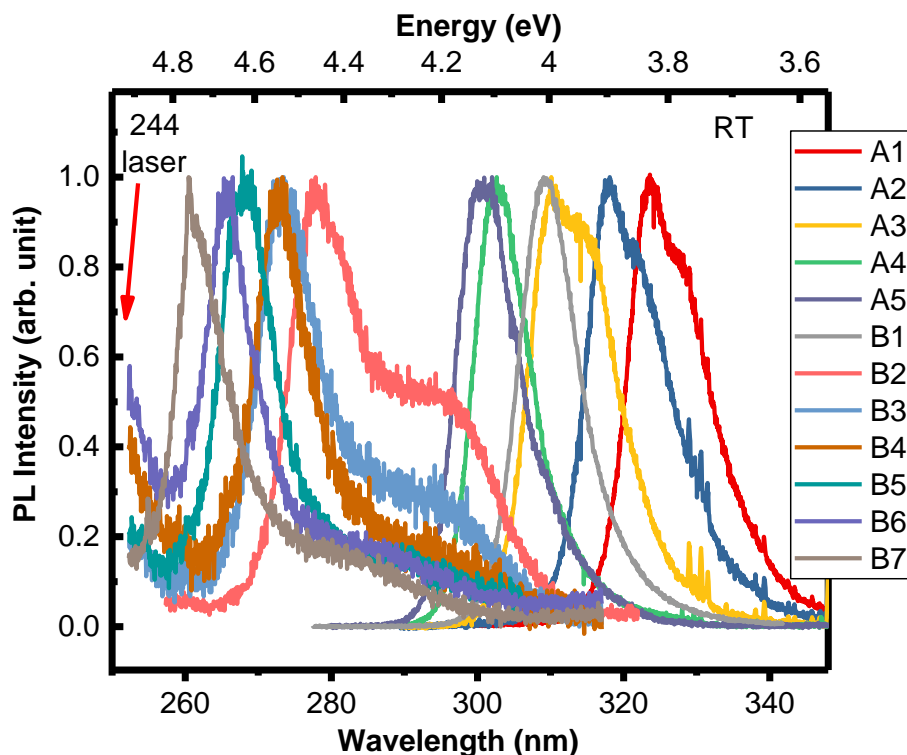


**Figure 4.7 Normalized PL spectra measured at RT for all the standard AlGa<sub>N</sub> samples.**

Figure 4.7 shows the PL spectra measured at RT. The emission wavelength ranges from 323 nm down to 261 nm, spanning a large composition range. A distinct shoulder at the low energy side of the spectrum can be seen in each AlGa<sub>N</sub> samples. Due to the very broad spectra it is difficult to assign to any possible reasons (e.g. Al content fluctuation, BSFs emission or phonon replica).

The Al content of all AlGa<sub>N</sub> samples is estimated from the PL emission energy using the formula below:

$$E_g(\text{Al}_x\text{Ga}_{1-x}\text{N}) = xE_g(\text{AlN}) + (1-x)E_g(\text{GaN}) - bx(1-x) \quad (4.1)$$

where band gaps of GaN (3.428 eV [12]) and AlN (6.015 eV [13]) at RT are used. The bowing parameter of  $b = +1$  eV, which has been widely used in the literature, is selected here, in spite of various values reported [12]. Note that the Al content evaluated might be lower than the real value since the deviation between the emission energy and the absorption edge, namely Stokes shift, is not taken into account. Assuming an average Stokes shift of 30-50 meV, the estimated value with the equation above will be 1-2% lower than the real one. Limitation of the evaluation also rises from the non-analysed strain state as well as the variety of bowing parameters reported [12], leading to an estimation incertitude of  $\pm 2\%$ .

The Al composition and the PL wavelength as the function of TMAI mole fraction in gas phase TMAI/ (TMAI + TMGa) is shown in Figure 4.8. It shows that the Al composition ( PL wavelength) is linearly increased (decreased) from 19.4% to 59.2% with increasing TMAI/ (TMAI + TMGa) ratio.

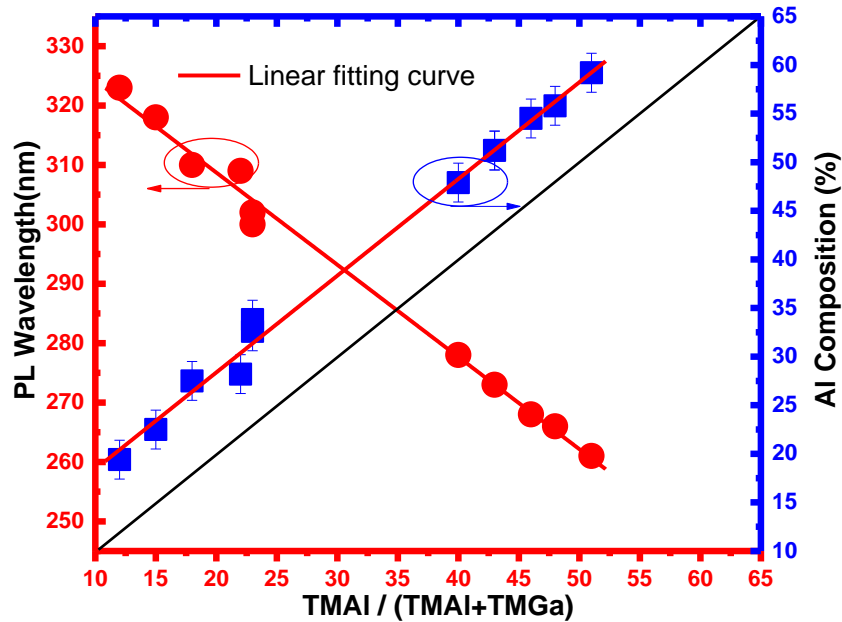


**Figure 4.8 PL emission wavelength and Al composition estimated from RT PL as a function of the TMAI / (TMAI + TMGa) ratio.**

It is also noticeable that the alloy composition in solid phase is about 5-7% higher than that in gas phase. Such behaviour was also observed by Han *et al* [14] and Kim *et al* [15]. It has been understood that the Al incorporation during AlGaN growth is mainly governed by two process: the pre-reaction effect in gas phase between TMAI and  $\text{NH}_3$ , and the desorption rate of group-III atoms from the surface [16]. Since the low reactor pressure is used in this work, the parasitic reaction is expected to be limited effectively. Therefore, high desorption

rate of Ga atoms due to the high growth temperature dominates the Al incorporation, leading to higher alloy concentration than that in gas phase.

### 4.3 Semi-polar (11-22) AlGa<sub>N</sub> MQWs

In order to investigate the QCSE within semi-polar AlGa<sub>N</sub> MQWs, a series of (11-22) AlGa<sub>N</sub> MQW samples with different QW thickness are grown on standard AlGa<sub>N</sub> templates with the structure B. The QW emission is aimed at 280 nm and corresponding gas flows for QW growth derive from the calculation based on linear relationship between the wavelength and the TMAI ratio in gas phase illustrated in Figure 4.8. The nominal Al composition in AlGa<sub>N</sub> QW is estimated to be 46%. The QW growth conditions are summarized in Table 4.2. Growth condition of AlGa<sub>N</sub> quantum barrier (QB) stems from sample B5 with Al composition of 54.5% from PL calculation. The thickness of QB is designed for 10 nm, i.e. 17 sec in growth time, which is estimated by correlating with the reference sample. The temperature and pressure are fixed at 1070 °C and 75 Torr respectively during the whole MQW growth.

**Table 4.2 Growth conditions of semi-polar (11-22) AlGa<sub>N</sub> MQWs.**

	Time	NH <sub>3</sub>	TMGa	TMAI	PL@RT	Estimated QW
	s	mmol/min	μmol/min	μmol/min	nm	Thickness / nm
AQW1	3	45	66.4	37.6	276	2.1
AQW2	4	45	66.4	37.6	278	2.5
AQW3	5	45	66.4	37.6	279	2.9

The thickness of QW is altered by varying the growth time. And the total thickness for a QW/QB pair is 12.1, 12.5 and 12.9 nm for Sample AQW1, AQW2 and AQW3, respectively, which is estimated by the QW satellite peaks in XRD  $\omega/2\theta$  scans performed along the [11-2-3] direction. Therefore, the corresponding QW thickness for AQW1, AQW2 and AQW3 is 2.1, 2.5 and 2.9 nm, respectively.

#### 4.3.1 RT and LT PL

RT PL spectra of semi-polar (11-22) AlGa<sub>N</sub> MQWs samples are shown in Figure 4.9 (a). Emissions from both MQWs and AlGa<sub>N</sub> barriers (~261 nm) can be recognised. As the QW thickness increases, the QW emission peak shifts from 276 nm to 279 nm, and the PL intensity increases by ~3 times, as shown in Figure 4.9 (b). The PL intensity tends to saturate when the QW thickness is larger than 2.5 nm.

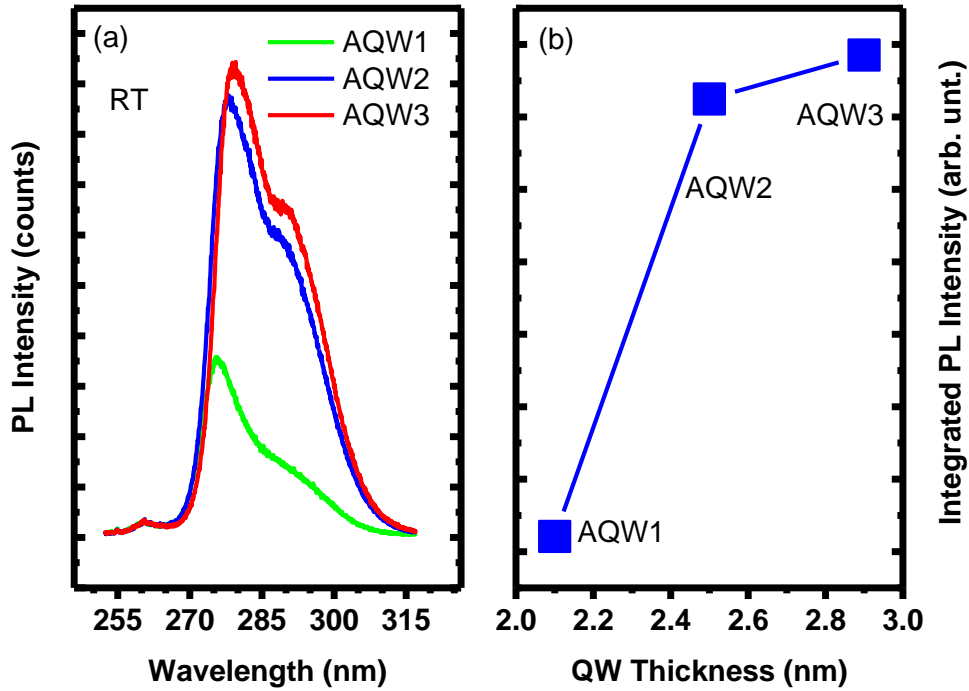


**Figure 4.9** RT PL (a) and integrated PL intensity (b) of semi-polar (11-22) AlGaIn MQWs.

PL spectra measured at LT (10K) are shown in Figure 4.10. All samples exhibit a single peak with a linewidth of 91, 92 and 89 meV for AQW1, AQW2 and AQW3, respectively. The intensity shows a linear increase with the increasing thickness of QWs, which is similar to the results observed in RT PL.

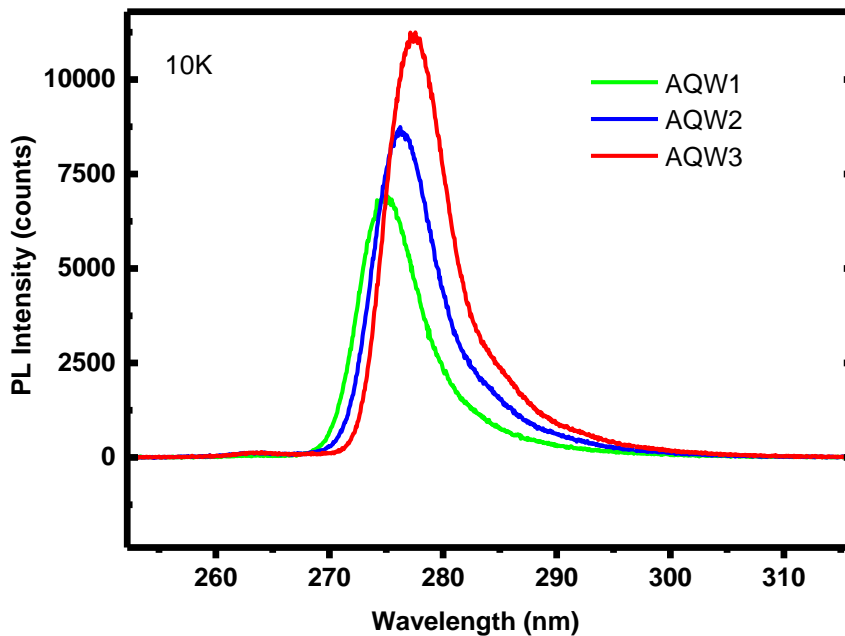


**Figure 4.10** LT PL of semi-polar (11-22) AlGaIn MQWs.

Given the weak polarization electric field within semi-polar (11-22) AlGaIn MQWs, we attribute the redshift of QW peaks to the decreased energy levels within the QWs (i.e., e1 for electrons and h1 for holes) due to the larger thickness. Based on a simple one-dimensional

finite potential well model, without taking the excitonic effect or polarization field into account, energy levels for e1 and h1 are calculated. From AQW1 to AQW3, the e1 energy level decreases from 122 to 81 meV while the h1 level decreases from 19 to 9 meV. These results indicate the confinement effect of the QWs becomes stronger with increasing thickness, which contributes to the enhanced PL intensity at RT. Such confinement effect, however, possibly cannot explain the increased PL intensity at LT as the thermal energy is too low to make carriers escape from the QWs. But thicker QWs are supposed to have less carrier leakage due to reduced carrier density [17], therefore the radiative recombination efficiency can be enhanced, which possibly contributes to the increase of LT PL intensity.

#### 4.3.2 Power dependent PL

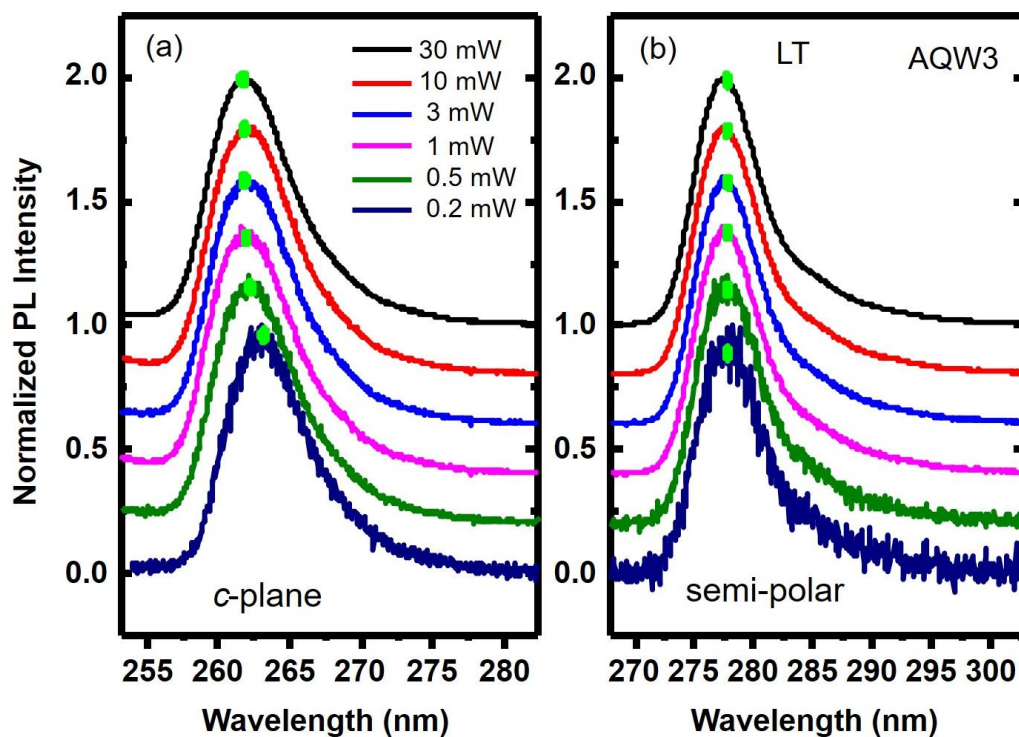


**Figure 4.11** Excitation-power dependent PL spectra of the reference *c*-plane AlGaIn MQWs (a) and semi-polar (11-22) AlGaIn MQWs sample AQW3 (b).

The excitation-power dependent PL measurements are performed in all semi-polar AlGaIn samples in order to investigate the QCSE within the MQWs. All measurements are performed at 10 K. A reference *c*-plane AlGaIn MQW sample is also studied for comparison. It can be seen from Figure 4.11 that, as the excitation energy increases from 0.2 mW to 30 mW, which is varied over two orders of magnitude, the spectra profiles of both semi-polar and *c*-plane samples remain unchanged. However, the semi-polar (11-22) AlGaIn MQWs do not show a clear change in peak positions whereas an obvious blue shift is observed in *c*-plane AlGaIn

MQWs. It has been understood that, such a blueshift in the polar sample is attributed to the carrier-induced screening of the polarization electric field, indicating the presence of QCSE within the active regions. Therefore, it can be concluded that QCSE in semi-polar (11-22) AlGa<sub>N</sub> MQWs is significantly reduced or almost eliminated.

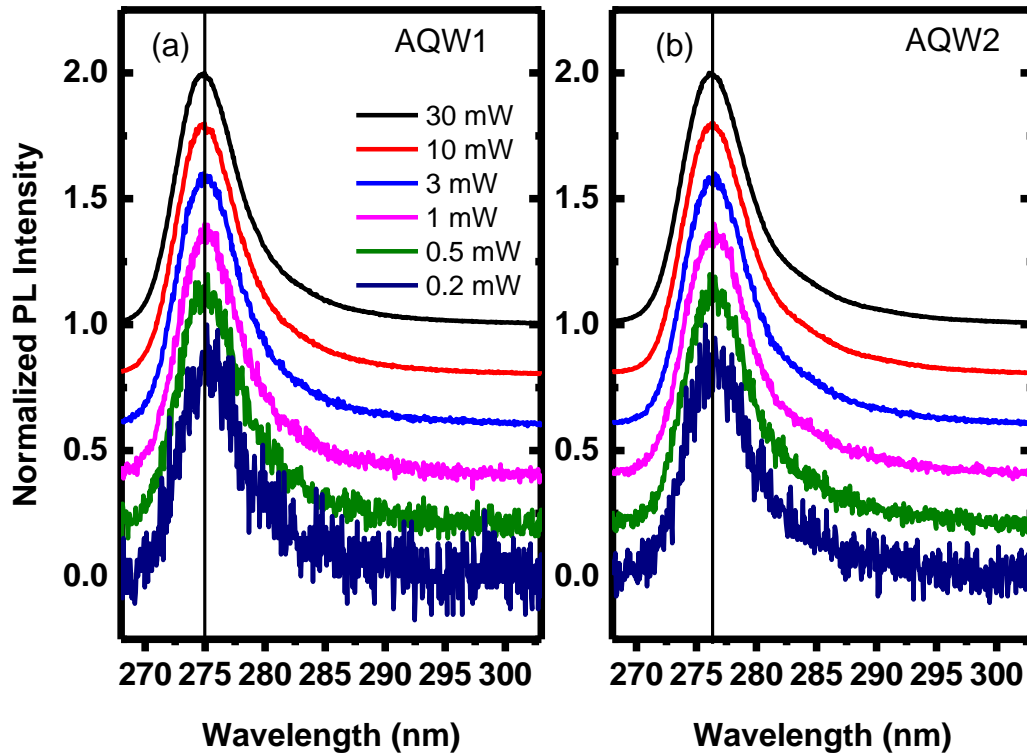


**Figure 4.12** Excitation-power dependent PL (measured at LT) for semi-polar (11-22) AlGa<sub>N</sub> MQWs sample AQW1 (a) and sample AQW2 (b).

The results of excitation-power dependent PL measurements in other AlGa<sub>N</sub> samples with various QW thickness are shown in Figure 4.12. Both semi-polar (11-22) AlGa<sub>N</sub> MQWs samples show similar behaviours with increasing power to sample AQW3, namely no clear peak position shift.

The peak positions are further extracted as a function of excitation power, as shown in Figure 4.13. With increasing QW width, semi-polar (11-22) AlGa<sub>N</sub> MQWs do not exhibit a larger deviation of peak positions, although this is normally expected in *c*-plane AlGa<sub>N</sub> MQWs [18]. It has been understood that in polar samples as the QW width increases, the separation of electrons wavefunction and holes wavefunction would become larger, resulting in stronger QCSE within the QWs. Therefore, the unique behaviour of semi-polar AlGa<sub>N</sub> MQWs with increasing QW thickness further confirms the absence of QCSE.

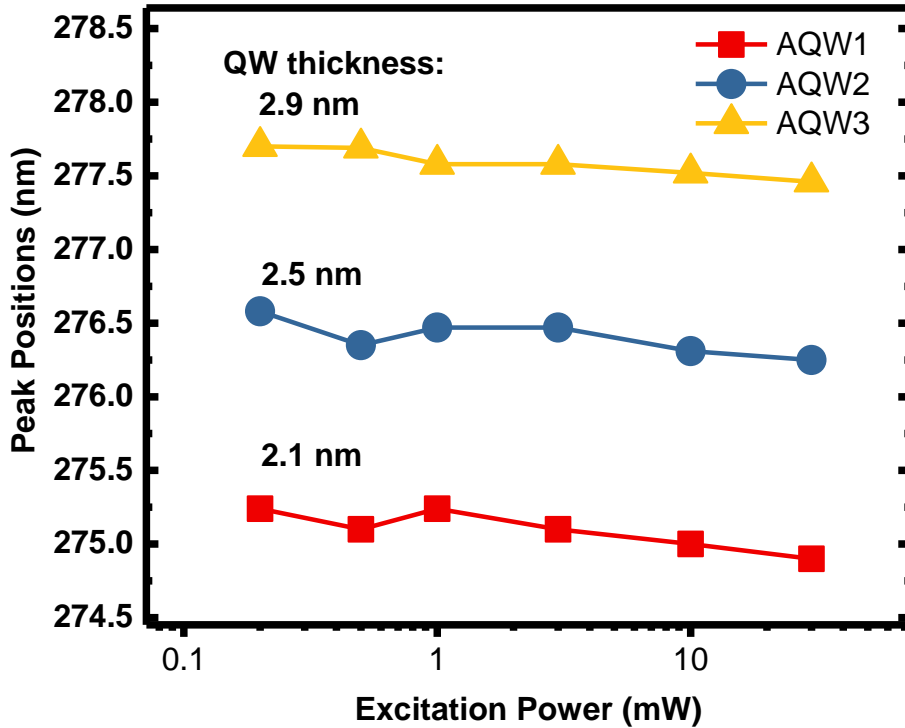


**Figure 4.13** Peak positions of semi-polar (11-22) AlGaIn MQWs as a function of excitation power.

## 4.4 Conclusion

Semi-polar (11-22) AlGaIn layers with different Al composition is obtained with either AlN or GaN buffer layer on the *m*-plane sapphire substrate using MOCVD. The Al composition estimated with RT PL is increased from 19.4% to 59.2% while the PL emission wavelength is decreased from 323 nm to 261 nm. A smooth surface with typical arrow-like features is observed in all samples. It is worth noting that AlGaIn samples with GaN buffer (AlGaIn on GaN) exhibit serious wafer cracking, which is not favourable for the device fabrication in the future. Also, the crystal quality of the standard AlGaIn, which is typically 0.4-0.5° along [1-100] direction and 0.2-0.3° along [11-2-3] direction, is far from satisfactory for UV devices.

Besides, semi-polar (11-22) AlGaIn MQWs with various QW thickness grown on standard AlGaIn templates are also studied to investigate the QCSE in the MQWs. Compared to the reference *c*-plane AlGaIn MQWs, semi-polar AlGaIn MQWs exhibit no clear blueshift of peak positions with increasing excitation power. Also, the deviation of peak positions of semi-polar AlGaIn MQWs is found not being affected by the increased thickness of QWs. These results confirm the significantly reduced of QCSE within the semi-polar (11-22) AlGaIn MQWs.

## References

1. J. Jang, S. Woo, D. Min, and O. Nam, *J. Nanosci. Nanotechnol.* 15, 1895 (2015).
2. K. Katayama, N. Saga, M. Ueno, T. Ikegami, and T. Nakamura, *Electronics and Communications in Japan* 98, 9 (2015).
3. H. Luan, X. Zhang, Z. Liang, Y. Wang, Q. Dai, H. Yang, Z. Wu, J. Zhao, and Y. Cui, *Phys. Stat. Sol. (a)* 214, 1600802 (2017).
4. S. Jo, I. Oshima, T. Matsumoto, N. Maeda, N. Kamata, and H. Hirayama, *Phys. Stat. Sol. (c)* 14, 1600248 (2017).
5. T. Wunderer, Z. Yang, M. Feneberg, M. Batres, M. Teepe, and N. Johnson, *Appl. Phys. Lett.* 111, 111101 (2017).
6. T. Wang, J. Bai, P. J. Parbrook, and A. G. Cullis, *Appl. Phys. Lett.* 87, 151906 (2005).
7. S. Ploch, M. Frentrup, T. Wernicke, M. Pristovsek, M. Weyers, and M. Kneissl, *J. Cryst. Growth* 312, 2171 (2010).
8. D. V. Dinh, M. Conroy, V.Z. Zubialeovich, N. Petkov, J. D. Holmes, and P. J. Parbrook, *J. Cryst. Growth* 414, 94 (2015).
9. K. Balakrishnan, M. Lachab, H. C. Chen, D. Blom, V. Adivarahan, I. Ahmad, Q. Fareed, and M. A. Khan, *Phys. Stat. Sol. (a)* 208, 2724 (2011).
10. J. Stellmach, F. Mehnke, M. Frentrup, C. Reich, J. Schlegel, M. Pristovsek, T. Wernicke, and M. Kneissl, *J. Cryst. Growth* 367, 42 (2013).
11. N. Hatui, A. A. Rahman, C. B. Maliakkal, and A. Bhattacharya, *J. Cryst. Growth* 437, 1 (2016).
12. I. Vurgaftman and J. R. Meyer, *J. Appl. Phys.* 94, 3675 (2003).
13. M. Feneberg, R. A. R. Leute, B. Neuschl, K. Thonke, and M. Bickermann, *Phys. Rev. B.* 82, 075208 (2010).
14. D. -Y. Han, H. -J. Li, G. -J. Zhao, H. -Y. Wei, S. -Y. Yang, and L. -S. Wang, *Chin. Phys. B* 25, 048105 (2016).
15. S. Kim, J. Seo, K. Lee, H. Lee, and K. Park, *J. Korean Phys. Soc.* 41, 726 (2002).
16. M. Dauelsberg, D. Brien, H. Rauf, F. Reiher, J. Baumgartl, O. Häberlen, A. S. Segal, A. V. Lobanova, E. V. Yakovlev, R. A. Talalaev, *J. Cryst. Growth* 393, 103 (2014).
17. G. Verzellesi, D. Saguatti, M. Meneghini, F. Bertazzi, M. Goano, G. Meneghesso, and E. Zanoni, *J. Appl. Phys.* 114, 071101 (2013).
18. H. M. Ng, R. Harel, S. N. G. Chu, and A. Y. Cho, *J. Electron. Mater.* 30, 134 (2001).

# Chapter 5 Epitaxial Growth of Semi-polar (11-22) AlGa<sub>N</sub> with Overgrowth Technique

## 5.1 Introduction

As we discussed in Chapter 1, there is an increasing demand in developing UV emitters, in particular, deep UV emitters for applications in water purification, environmental protection, medical instrumentation, non-line-of-sight communications, etc, where AlGa<sub>N</sub> with high Al composition would be a promising semiconductor candidate. So far, the studies on AlGa<sub>N</sub> based UV emitters are mainly limited to polar-oriented AlGa<sub>N</sub> grown on *c*-plane sapphire [1], where their active regions suffer from notable spontaneous and piezoelectric polarization induced electrical fields leading to a reduction in optical efficiency, the so-called quantum-confined stark effect. Furthermore, as we have shown in last chapter, AlGa<sub>N</sub> grown on GaN generally suffers from large tensile strain due to the lattice mismatch between AlGa<sub>N</sub> and GaN, leading to extensive cracks of AlGa<sub>N</sub> often observed on *c*-plane AlGa<sub>N</sub>. Both the QCSE and the cracking issue become more severe when Al composition is increased in order to move towards the deep UV spectral region.

The growth of AlGa<sub>N</sub> layers along a semi-polar or non-polar direction would be a promising solution, which can potentially minimize or even eliminate the QCSE and hence improve optical efficiency. However, the great challenge lies in that the crystal quality of semi-polar AlGa<sub>N</sub> is still far away from satisfactory.

Various methods have been developed to obtain high-quality AlGa<sub>N</sub> grown on *c*-plane sapphire (i.e., polar orientation), such as migration-enhanced metalorganic chemical vapor deposition [2] and ammonia pulsed-flow multilayer growth technique [3]. In the meantime, various approaches have been developed in order to manage the strain of thick AlGa<sub>N</sub> films grown on *c*-plane substrates, such as using interlayers [4] or superlattice layers [5].

However, there are only a few reports on improving the crystal quality and addressing the cracking issue in semi-polar AlGa<sub>N</sub> so far [6-8]. Balakrishnan *et al* [6-7] obtained thick

and crack-free n-AlGaN (11-22) films by inserting a strain relieving AlN/AlGaN short-period superlattice structure on *m*-plane sapphire. Young *et al* [8] reported the compositionally graded semi-polar AlGaN epilayers on very expensive freestanding semi-polar (20-21) GaN substrates, where the strain is relaxed by generating misfit dislocations through primary (basal) slip and secondary (non-basal) slip systems.

So far, it is a great challenge to achieve thick and crack-free semi-polar AlGaN with high crystal quality on cost-effective sapphire substrates. Previously, our group developed a different overgrowth approach of semi-polar (11-22) GaN on micro-rod arrayed templates, leading to significantly improved crystal quality of semi-polar (11-22) GaN on sapphire [9-11]. As a result, high performance semi-polar LEDs with a long emission wavelength of up to amber have been achieved [11].

In this chapter, a two-step overgrowth technique is developed to improve the crystal quality and address the cracking issue for semi-polar AlGaN. Thick and crack-free semi-polar (11-22) AlGaN epilayers with different Al composition grown on overgrown GaN on micro-rod arrayed templates are obtained, exhibiting a very good crystal quality which was not reported before. The surface morphology and optical properties of the AlGaN layers are investigated and discussed in detail.

## 5.2 Experimental Details

### 5.2.1 Template Fabrication

In order to address the cracking issue and improve the material quality of semi-polar (11-22) AlGaN, a two-step overgrowth approach is developed based on the previous overgrowth technique developed by our group on semi-polar (11-22) GaN [9-11]. In this new overgrowth technique, non-coalesced GaN is first grown on the micro-rod arrayed template with the overgrowth technique, and the AlGaN layers are then deposited on the top.

The micro-rod arrayed (11-22) GaN template is obtained with an effective and controllable approach with the standard UV photolithography technology. The fabrication procedure is illustrated in Figure 5.1.

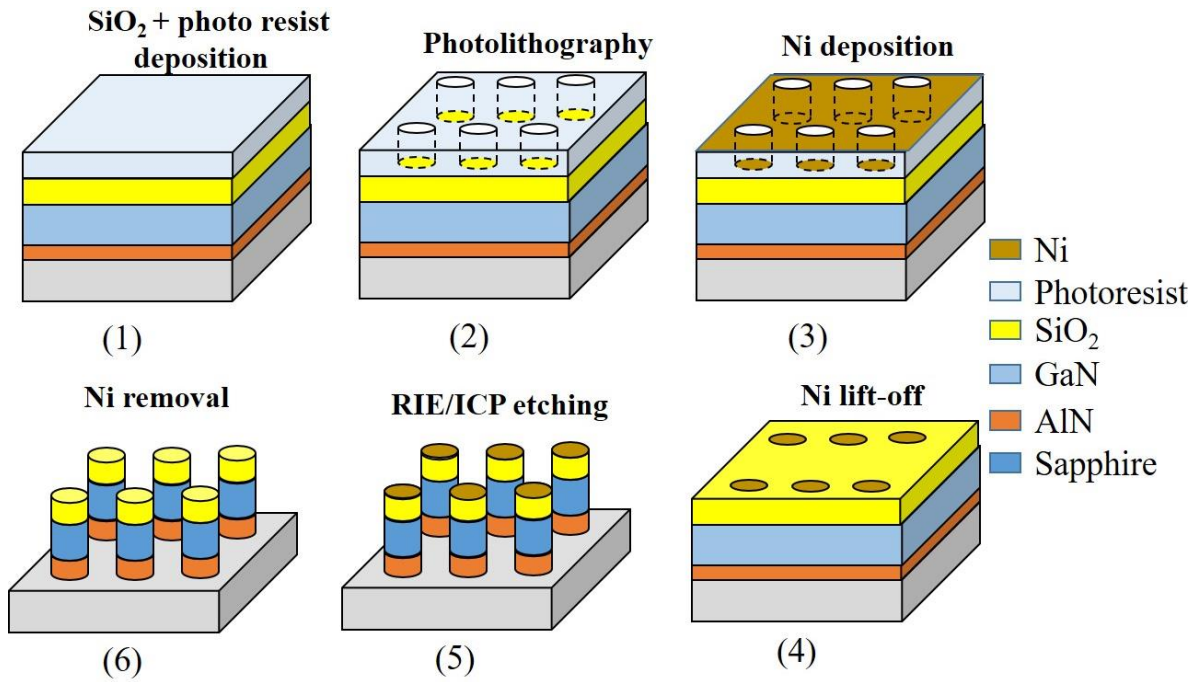


**Figure 5.1 Schematic fabrication procedures of the micro-rod arrayed template.**

First, a 520-nm-thick SiO<sub>2</sub> layer is deposited on the as-grown (11-22) GaN template (400 nm GaN/50 nm AlN/m-sapphire) with the plasma-enhanced chemical vapour deposition, followed by spin-coating of a ~1- $\mu$ m-thick photoresist layer. With the standard UV photolithography technology, the photo resist is patterned. Subsequently, the 50-nm-thick Ni is deposited with the e-beam evaporator and then lifted off by acetone. The residual Ni patterns act as etching masks for SiO<sub>2</sub> etching with reactive-ion etching, and then for GaN/AlN etching with the inductively coupled plasma etching.

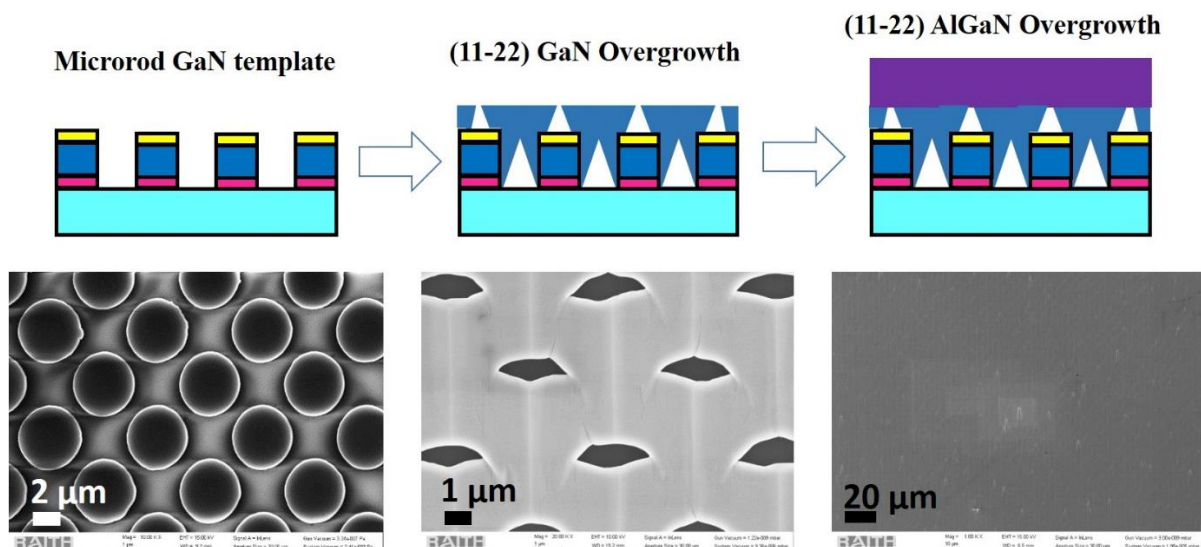


**Figure 5.2 Schematic growth procedures of the two-step overgrowth technique. Mr. L. Jiu is acknowledged for provision of the SEM image (bottom left) of micro-rod templates.**

### 5.2.2 Overgrowth Procedures

A top-view SEM image of the micro-rod template is present in Figure 5.2, showing GaN micro-rod arrays with high uniformity. Both the size and the gap between the neighbouring rods are 4  $\mu\text{m}$ . The template is then reloaded into the MOCVD reactor to proceed the growth with the overgrowth technique. In Figure 5.2 we can see that the GaN layer is not completely coalesced after overgrowth, and many residual voids with  $\sim 1 \mu\text{m}$  width along  $c$  direction can be seen on the surface. AlGaN is then deposited on the non-coalesced GaN layer, forming flat surface finally (Figure 5.2).

In the GaN overgrowth, it is grown for 2900 sec with the growth temperature of 1020  $^{\circ}\text{C}$  and the reactor pressure of 75 torr. The flux of  $\text{NH}_3$  and TMGa is 152 mmol/min and 98.4  $\mu\text{mol}/\text{min}$  respectively with corresponding V/III ratio of 1540.

For the AlGaN growth, the growth temperature and reactor pressure are fixed at 1040  $^{\circ}\text{C}$  and 65 torr, respectively. The Al composition are tuned by changing the flux of  $\text{NH}_3$ , TMAI and TMGa. Growth parameters for each AlGaN sample with the corresponding V/III ratio and PL emission wavelength are summarized in Table 5.1 below.

**Table 5.1 Growth parameters for the AlGaN overgrowth samples.**

No.	Temp. $^{\circ}\text{C}$	Press. torr	$\text{NH}_3$ mmol/min	TMGa $\mu\text{mol}/\text{min}$	TMAI $\mu\text{mol}/\text{min}$	V/III ratio	RT PL nm	Gas phase Al%
<b>AO1</b>	1040	65	107	98.4	22.3	886	309	18%
<b>AO2</b>	1040	65	85	98.4	22.3	704	308	18%
<b>AO3</b>	1040	65	85	98.4	26.5	681	303	21%
<b>AO4</b>	1040	65	67	86.1	26.5	595	299	23%
<b>AO5</b>	1040	65	58	86.1	33.4	534	291	28%
<b>AO6</b>	1040	65	49	73.8	34.8	451	283	32%
<b>AO7</b>	1040	65	45	61.5	36.2	461	276	37%
<b>AO8</b>	1040	65	45	54.1	36.2	498	271	40%

The typical cross-sectional structure of the overgrowth samples is shown in Figure 5.3.

The thickness of overgrown GaN and AlGaN are 2.7  $\mu\text{m}$  and 2.1  $\mu\text{m}$ , respectively. As illustrated in Figure 5.3, the overgrowth of GaN starts from the side wall of micro-rods along  $c$  direction. The first type of voids are formed between the neighbouring rods when  $+c$  orientated GaN meets with  $-c$  or  $a$  orientated GaN. And the second type of voids are formed at

top of  $\text{SiO}_2$ , where the final coalescence process takes place. From Figure 5.3, it can be also seen that the underlying GaN is not fully coalesced.

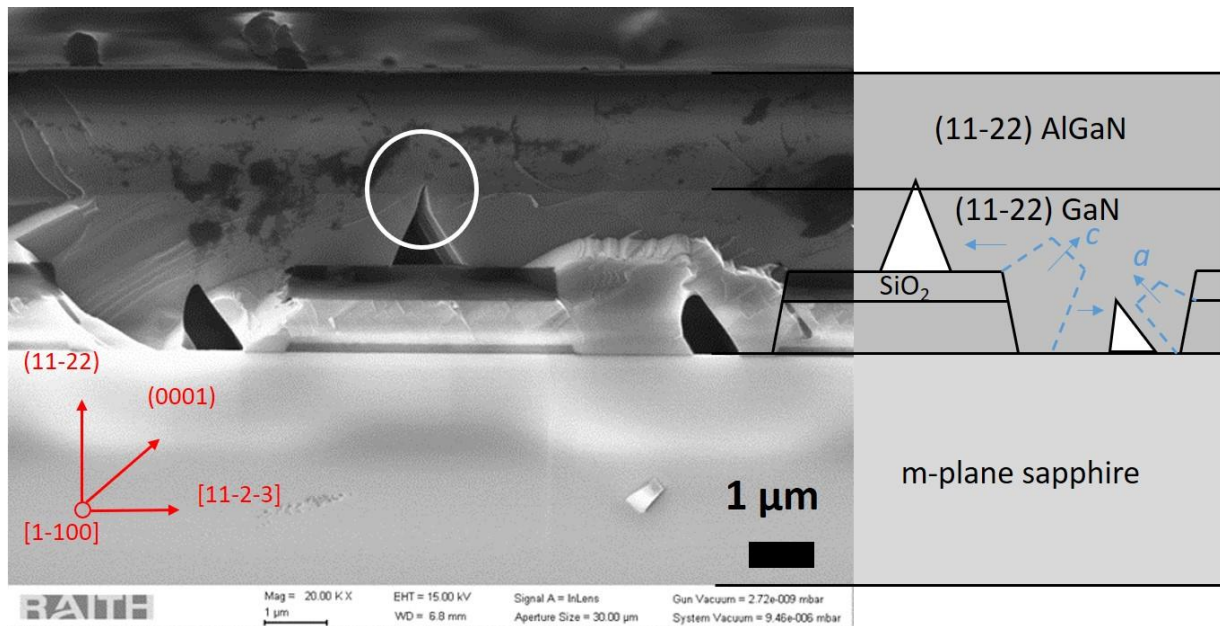


**Figure 5.3** A typical cross-sectional structure of semi-polar (11-22) AlGaN overgrowth samples. The circle shows the non-coalesced GaN voids. The overgrowth revolution is also illustrated on the right side.

## 5.3 Characterization and Discussions

### 5.3.1 Surface morphology

The surface morphology investigated by SEM is shown in Figure 5.4. The typical undulated surface with arrow-like features is observed in all samples. Overall, the surface of the AlGaN samples with the overgrowth technique is rougher than that of the standard AlGaN on planar substrate studied in Chapter 4.2. Larger and deeper arrow-like features are observed in overgrowth samples.

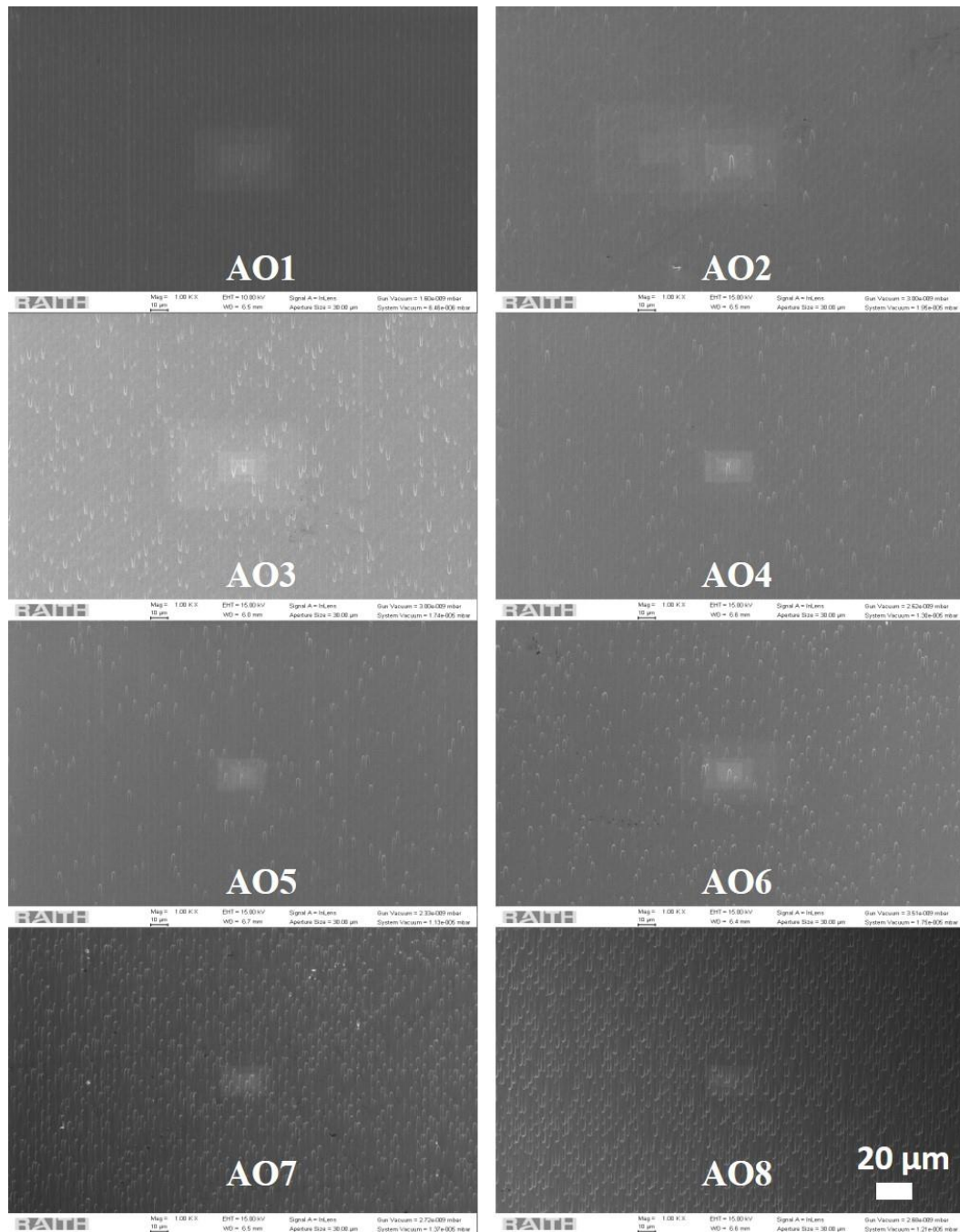


**Figure 5.4 Top-view SEM images of (11-22) AlGaN overgrowth samples AO1-AO8.**

For lower-Al-content samples (e.g. AO1,AO2 and AO4), arrow-like features are weaker and exhibit lower density, while for higher-Al-content samples (e.g. AO7 and AO8) these features become stronger with higher density. As arrow-like features are attributed to the anisotropic growth mode along different crystalline orientations, it can be concluded that the anisotropic growth rates become more severe with increasing Al content.

Importantly, all semi-polar (11-22) AlGaN overgrown on GaN samples exhibit crack-free surfaces as shown in Figure 5.5, which indicates significant strain relaxation within the AlGaN layers. This will be analysed in detail in Chapter 6.

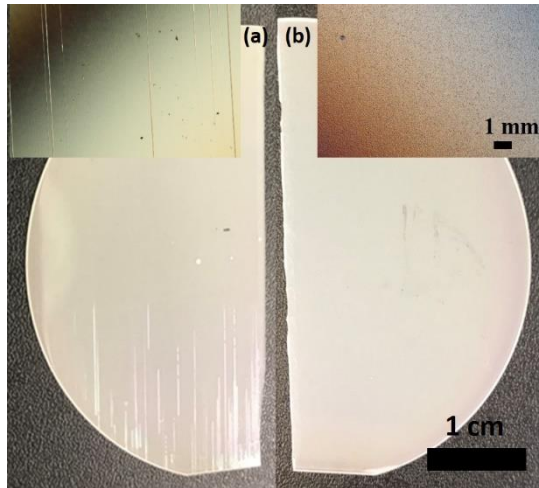


**Figure 5.5** Photography of standard AlGaN on GaN sample with cracking (a) and AlGaN overgrowth sample without cracking (b). The insets show the optical images under 50X magnification.

Figure 5.6 (a) shows the XRD data measured in a  $\omega/2\theta$  mode for all the samples with different Al composition. The diffraction peaks from (30-30) sapphire, (11-22) GaN and AlGaN have been clearly observed, with the positions of the former two peaks remaining unchanged when the Al composition varies. The normalized PL spectra measured at RT are shown in Figure 5.6 (b), exhibiting the emission wavelength changing from 309 to 271 nm.

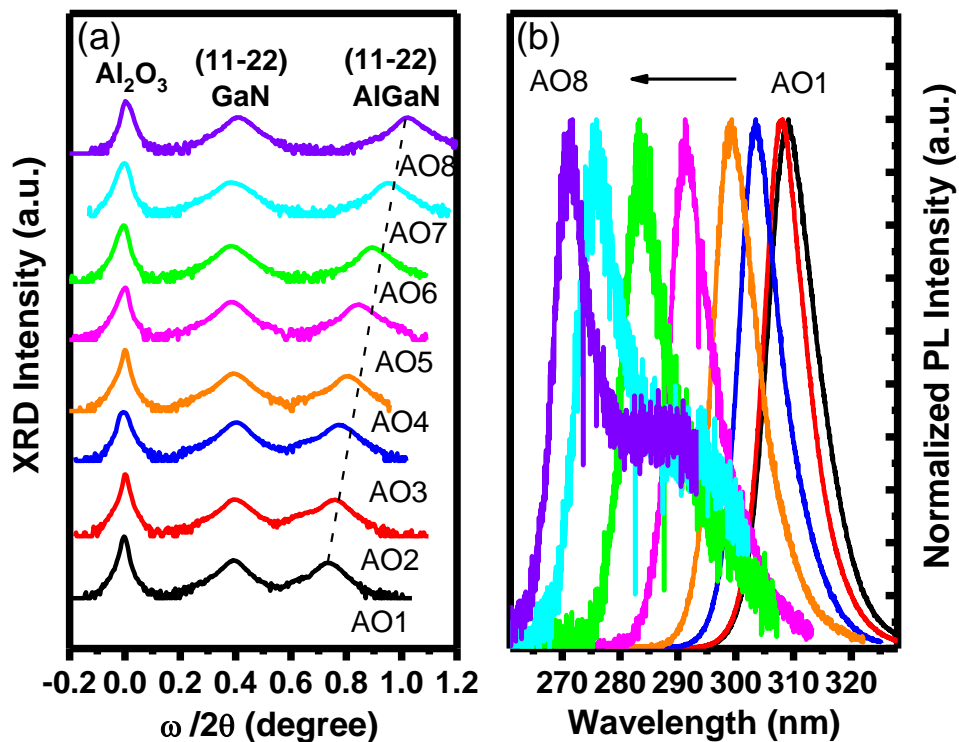


**Figure 5.6** XRD  $\omega/2\theta$  scans (a) and RT PL spectra (b) of semi-polar (11-22) AlGaN overgrowth samples.

### 5.3.2 Determination of the Al Content

The Al composition is first determined by symmetric XRD  $\omega/2\theta$  scans as people usually do in *c*-plane AlGa<sub>N</sub>. As suggested by Young *et al* [12], the degree of strain relaxation of semi-polar (11-22) III-nitride layers can be determined by the lattice tilt along [11-2-3], as the partial relaxation occurs along this direction through the misfit dislocation formation and threading dislocation glide on the (0001) slip plane. Such lattice tilt can be obtained by measuring the symmetric or asymmetric RSMs along [11-2-3]. It is found that from sample AO1 to AO8, the tilt angle between the AlGa<sub>N</sub> and the underlying Ga<sub>N</sub> is increased from 0.92° to 1.65° (shown in Chapter 6.4.3). Given that the fully relaxed semi-polar AlN exhibits a tilt angle of ~ 2.0° with respect to the substrate reported by Dinh *et al* [13], the relaxation degree of these AlGa<sub>N</sub> layers are roughly estimated to be from 46% to 83%, which is also in good agreement with the calculated relaxation degree reported in [12]. The obtained Al content is then shown in Figure 5.7. Given the simplification in the relaxation degree, a deviation of  $\pm 2\%$  in Al composition might be considered.

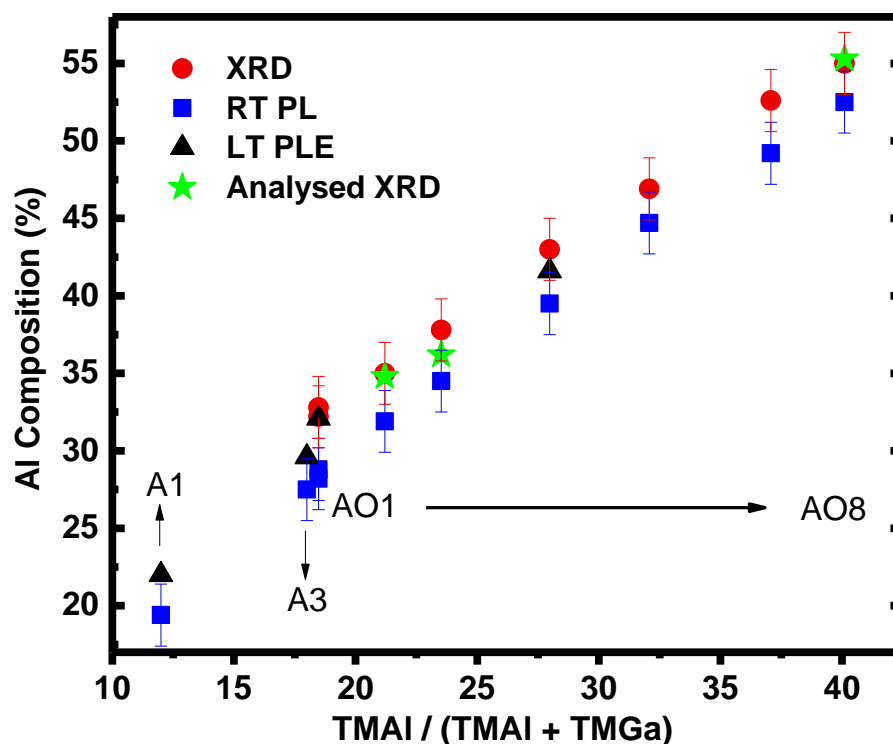


**Figure 5.7** The Al composition estimated from XRD, RT PL, LT PLE and analysed XRD as a function of the TMAI / (TMAI + TMGa) ratio.

The Al content can be also simply estimated from RT PL shown in Figure 5.6 (b) as what we have done in Chapter 4 in spite of some uncertainties e.g. Stokes shift and bowing parameters. The obtained Al content with  $\pm 2\%$  incertitude is also shown in Figure 5.7.

PLE measurements are further performed in some samples (including standard and overgrown samples) to calculate the Al content, as shown in Figure 5.8. To obtain the absorption edge associated with the AlGa<sub>1-x</sub>N band gap, the detection energy of PLE is fixed at the peak position of NBE. The absorption edge and Stokes shift can be extracted using a sigmoidal fitting curve below [14]:

$$\alpha(E) = \frac{\alpha_0}{1 + \exp\left(\frac{E_{eff} - E}{\Delta E}\right)} \quad (5.1)$$

where  $E_{eff}$  is the effective band gap or absorption edge,  $\Delta E$  is a broadening parameter and  $\alpha_0$  is a fitting constant. The Stokes shift is defined as the difference between  $E_{eff}$  and the PL peak energy  $E_{PL}$ , i.e.  $E_{eff} - E_{PL}$ . It can be seen from Figure 5.8 that the Stokes shift increases with increasing Al content, indicating larger localization effect in high-Al-content samples.

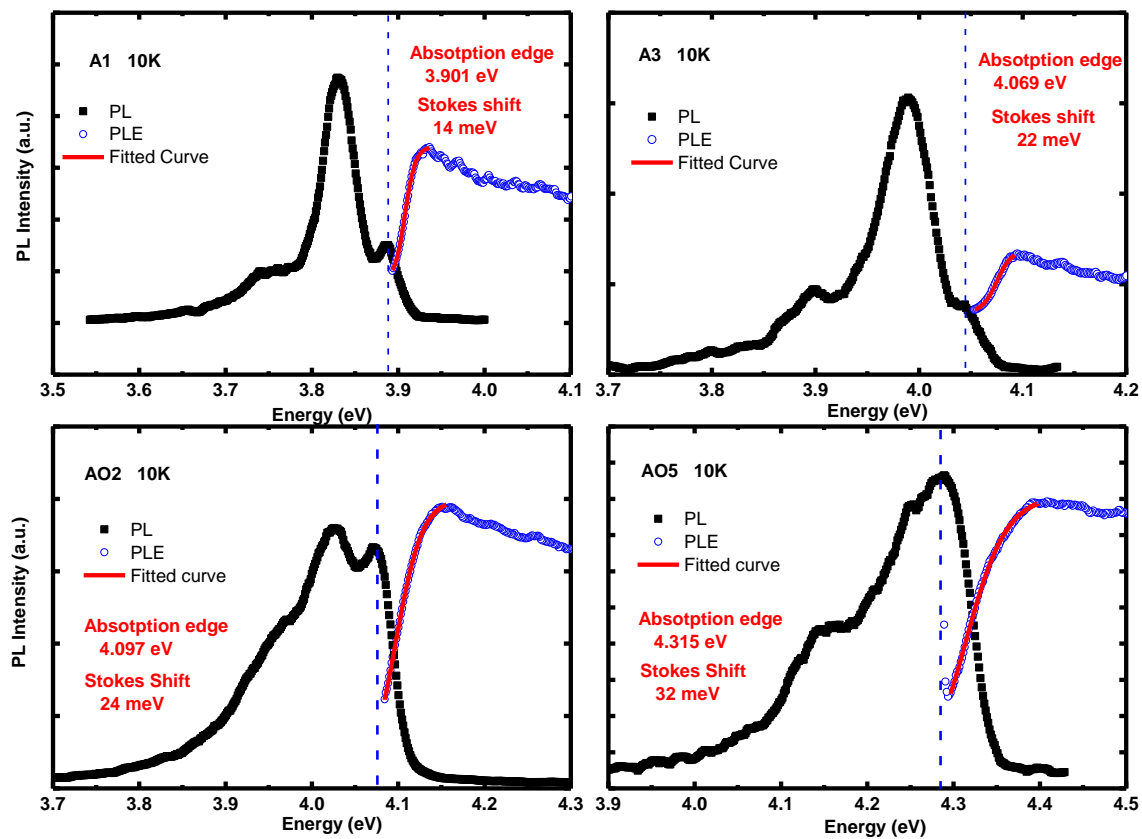


**Figure 5.8** PL and PLE spectra measured at 10K for standard samples A1 and A3, and overgrown samples AO2 and AO5. Detected energy in PLE is indicated with a dish line.

To obtain the Al content an equation similar to Equation 4.1 is used, whereas the band gap of AlN (6.089 eV) and GaN (3.478 eV) at 10K [15] and a widely used bowing parameter (+1 eV) are used. The result is also shown in Figure 5.7 for comparison.

Moreover, a more accurate method developed by Frentrup *et al* [16] based on a triclinic unit cell is adopted to get the Al content in some overgrowth samples as shown in Figure 5.7,

termed as ‘analysed XRD’. As the Al content is calculated from multiple on-axis and off-axis XRD measurements using a least square fit, the absolute error is expected to be about  $\pm 0.2\%$  [16]. Details about this calculation method are not described here (but will be introduced in Chapter 6) to avoid prolixity of this chapter.

It can be seen from Figure 5.7 that, the Al content almost linearly increases with the increasing TMAI fraction in gas phase. All four measurement methods are in good agreement with each other, given the simplification and/or incertitude there. The Al content obtained from analysed XRD and PLE measurements are more reliable, though uncertainty e.g. various published bowing parameters still exists in PLE measurements. The difference between PL data and the PLE (or analysed XRD) is mainly attributed to the Stokes shift, whose value is estimated and shown in Figure 5.8. Note that the Al content of all AlGaN overgrowth samples used in this thesis derives from the analysed XRD and PLE measurements where the data is available, or from the normal XRD measurements taking the proper relaxation degree into account.

### 5.3.3 Crystal Quality

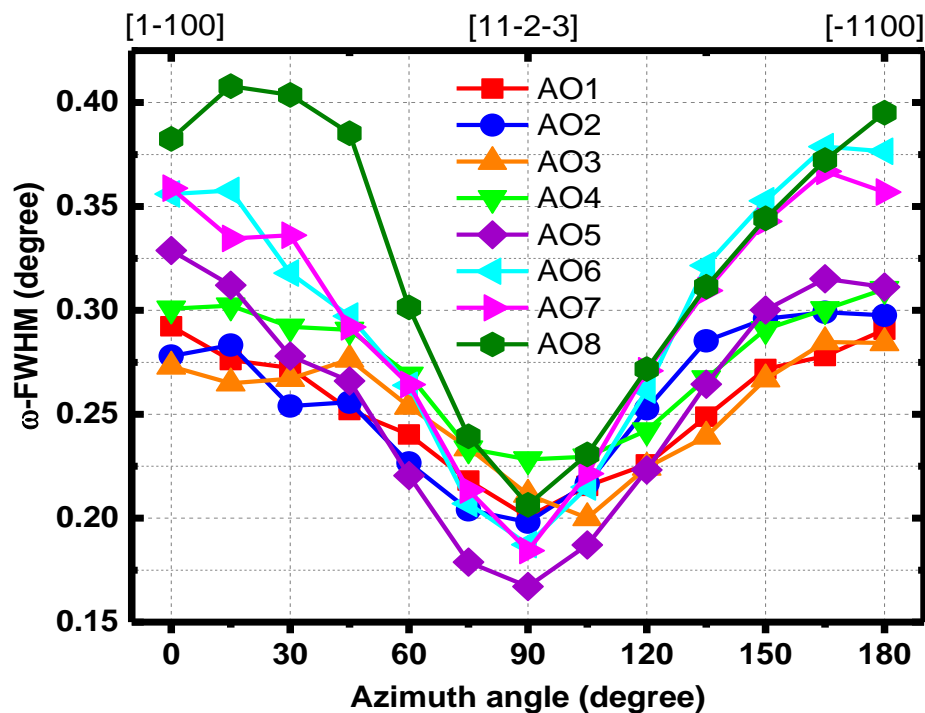


**Figure 5.9 Azimuth dependent XRC FWHMs for AlGaN overgrowth samples.**

FWHMs of XRD rocking curves (XRC) measured as a function of an azimuth angle from  $0^{\circ}$  to  $180^{\circ}$  on all samples is presented in Figure 5.9. It shows a typical behaviour for semi-polar

(11-22) nitrides, i.e., the lowest FWHM along [11-2-3] (i.e.,  $90^\circ$  azimuth angle) and the largest FWHM along [1-100] (i.e.,  $0^\circ$  azimuth angle).

XRC FWHMs as a function of Al composition is presented in Figure 5.10, indicating that the (11-22) FWHMs along the [1-100]/[11-2-3] directions increases from  $0.292^\circ/0.201^\circ$  to  $0.387^\circ/0.206^\circ$  with Al composition increasing from 32.0 to 55.3%. Among the reported results, these are the best report for the (11-22) AlGa<sub>N</sub> with similar Al composition [6, 17-19]. It means that our samples (although grown under un-optimized conditions) demonstrate the best quality of semi-polar AlGa<sub>N</sub> reported so far, which is expected to be further improved once optimized. More analysis about the crystal quality will be shown in Chapter 6.

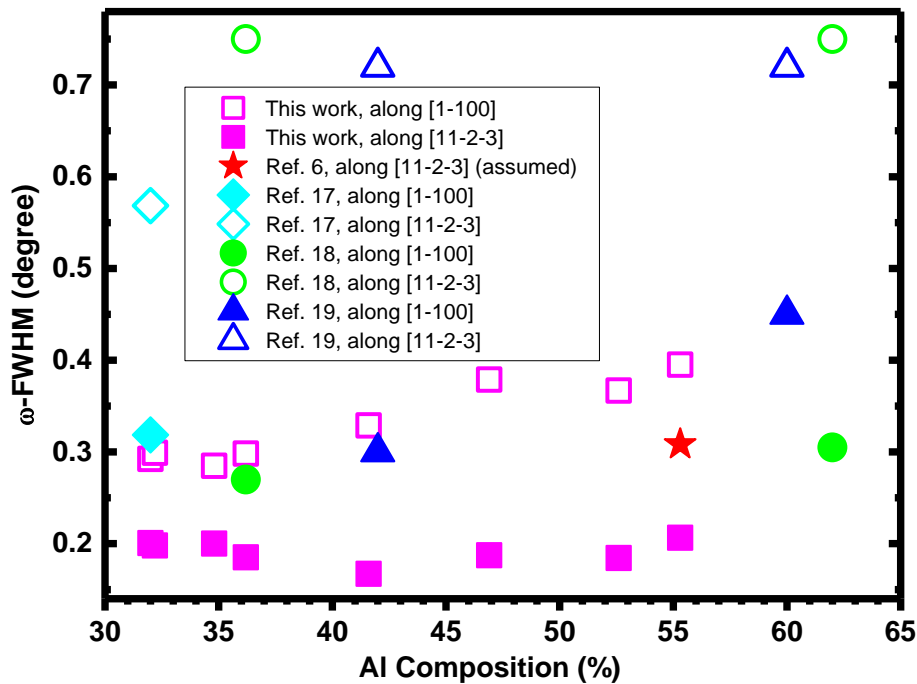


**Figure 5.10** The (11-22) XRC FWHMs of AlGa<sub>N</sub> overgrowth layers plotted as a function of the Al composition. Data from other reports is also plotted for comparison.

#### 5.3.4 Optical Property

All AlGa<sub>N</sub> overgrowth samples are further measured at same conditions to compare the PL intensity, as shown in Figure 5.11. It can be found that the PL intensity drops down quickly as the wavelength decreases from 309 nm to 283 nm. This is mainly attributed to the poorer crystal quality when the Al content increases, generating more defects as non-radiative recombination centres. However, when the wavelength decreases from 283 nm to 271 nm, a slight rise in PL intensity is observed. Since the quality of the samples at the short wavelength is poorer (see Figure 5.10), a possible reason for the increased intensity in this range could be

the rough surface of these samples, which could cause stronger light scattering and hence improve extraction efficiency.

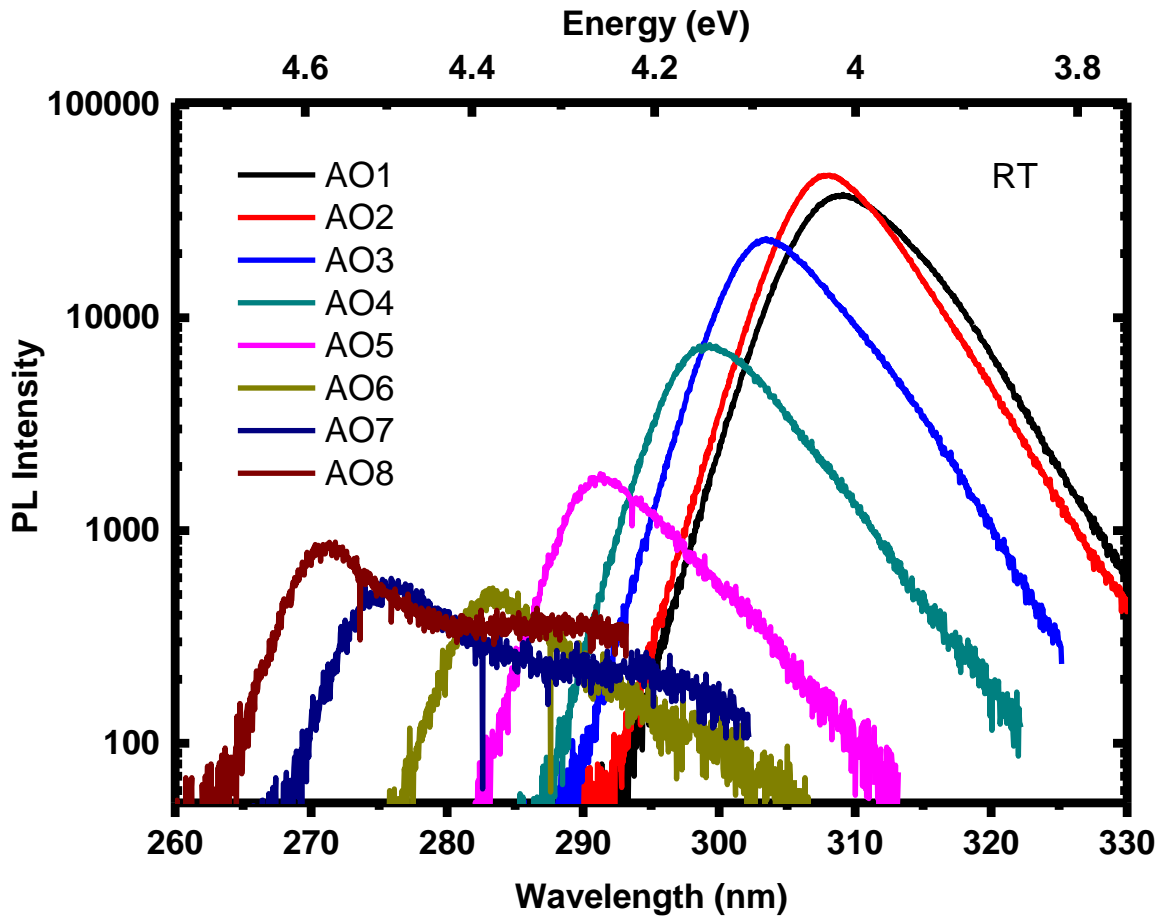


**Figure 5.11** RT PL of semi-polar (11-22) AlGaIn overgrowth samples.

It is noteworthy that in Figure 5.11 a shoulder peak at the long wavelength side of the RT PL spectra is observed in all samples and it becomes more pronounced when the Al composition is higher than 46%. In order to further investigate the optical properties, CL measurements are carried out on AlGaIn samples at RT, as shown in Figure 5.12.

It can be seen from the panchromatic CL image that the emission property of the arrow-like features (or “chevron”) is different with that of majority areas. The wavelength becomes longer whereas the intensity becomes weaker when it is close to the chevron, indicating different Al composition in these areas. As the chevron densities become significantly higher in high-Al-composition AlGaIn sample as shown in Figure 5.4, such non-uniformity of Al composition distribution near the chevron regions could contribute to the side peaks formation in PL spectrum shown in Figure 5.11.

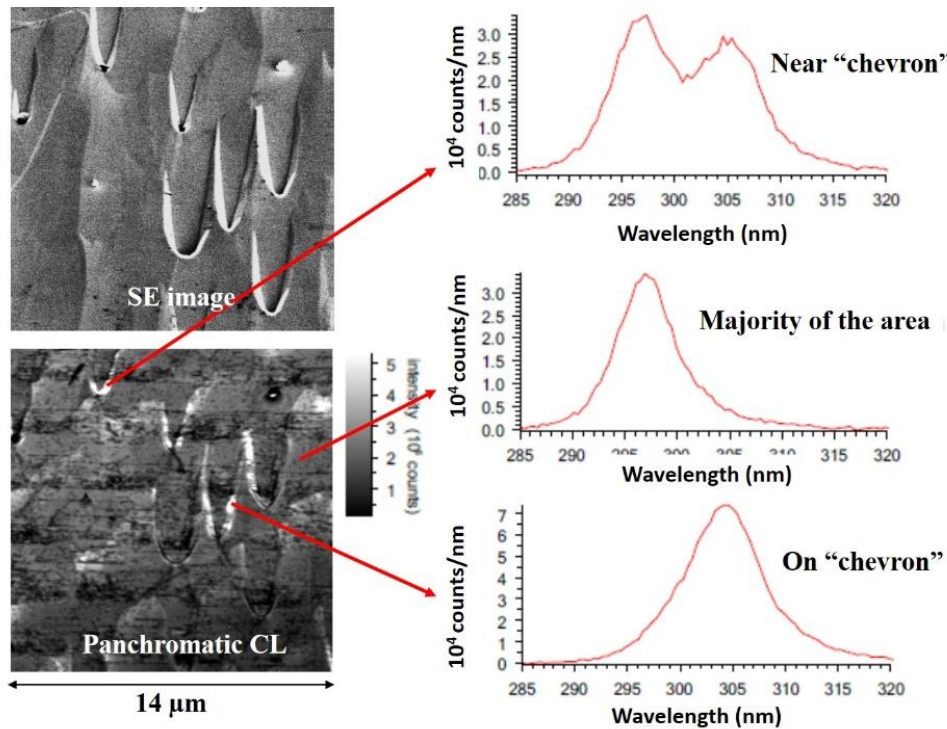


**Figure 5.12** Secondary-electron (SE) images and panchromatic CL images of the AlGaIn overgrowth sample (AO4). The CL spectra of different regions are extracted and shown. Dr. J. Bruckbauer is acknowledged for provision of this measurement.

### 5.3.5 Growth Temperature Effect

To investigate the growth temperature effect on surface morphology and crystalline quality of semi-polar (11-22) AlGaIn samples, the reactor pressure and the V/III ratio are fixed while growth temperature for AlGaIn layers varies from 1055 °C to 1087 °C. Growth parameters are summarized in Table 5.2.

**Table 5.2** Growth parameters for semi-polar (11-22) AlGaIn overgrowth samples with various growth temperatures.

Samples	Temp. °C	Press. torr	NH <sub>3</sub> mmol/min	TMGa μmol/min	TMAI μmol/min	PL@RT /nm
<b>BO1</b>	1055	75	66.9	61.5	18.1	296
<b>BO2</b>	1074	75	66.9	61.5	18.1	296
<b>BO3</b>	1080	75	66.9	61.5	18.1	296
<b>BO4</b>	1087	75	66.9	61.5	18.1	296

The surface morphology is characterized by the reflectivity of in-situ laser (635 nm) as well as the SEM. As shown in Figure 5.11, the highest reflectance of AlGaIn surface is obtained

at the moderate growth temperature, i.e. 1074<sup>0</sup>C, where the surface with lowest density of arrow-like features is also observed. Lower and higher temperatures both generate higher densities and deeper arrow-like features on the AlGa<sub>N</sub> surfaces.

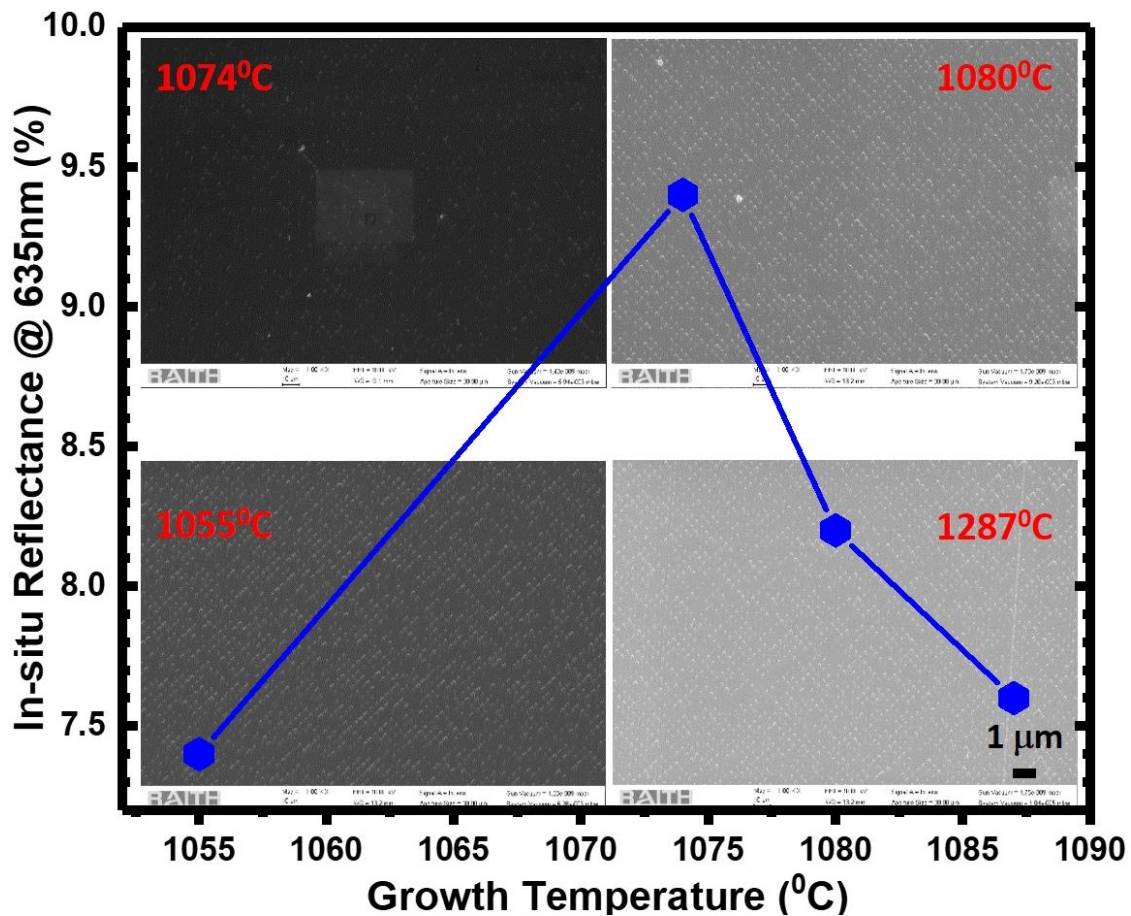


**Figure 5.11 In-situ reflectance of 635 nm laser of AlGa<sub>N</sub> overgrowth samples with different temperatures. The insets show the top-view SEM images at each temperature.**

It has been understood in *c*-plane Al(Ga)<sub>N</sub> growth that higher temperature is normally favourable of good surface due to the enhanced diffusion length, while the low temperature typically attenuates the anisotropic growth in semi-polar layers leading to better surface morphology. Therefore, the moderate growth temperature could be the compromised result of two competitive mechanisms.

The FWHMs of the XRD rocking curves dependence on the azimuth angle are shown in Figure 5.12. With increasing growth temperature, the overall crystal quality of the AlGa<sub>N</sub> samples improves. And the AlGa<sub>N</sub> sample with the highest temperature exhibits the narrowest XRC linewidth both along [1-100] direction (0<sup>0</sup>) and [11-2-3] direction (90<sup>0</sup>). The improved crystal quality could be attributed to the enhanced diffusion length of Al atoms when the temperature increases.

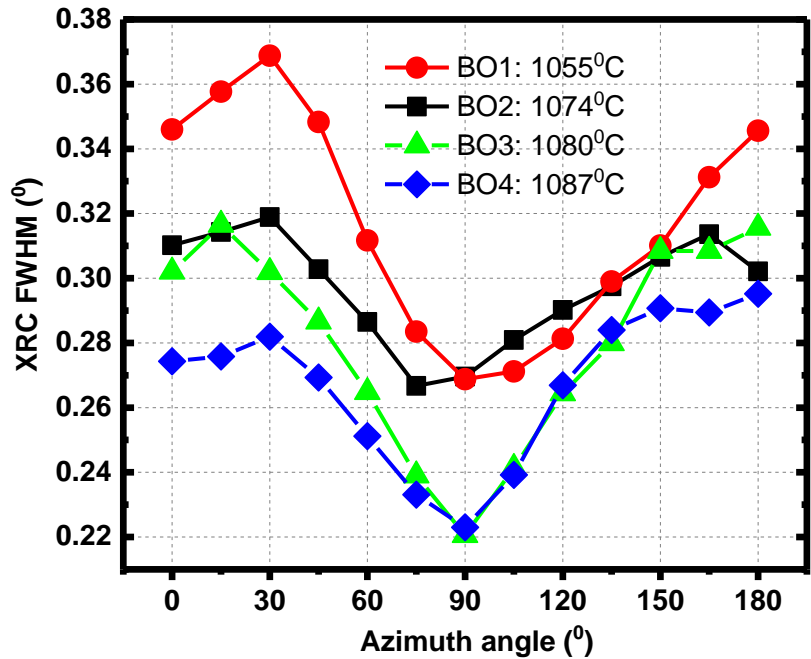


**Figure 5.12** Azimuth dependent XRC FWHMs of AlGaIn overgrowth samples grown at various temperatures.

The RT PL measurements are also performed as presented in Figure 5.13. Interestingly, although the growth temperature is increased from 1055 °C to 1087 °C, the PL wavelength (or Al composition) is almost no changed, indicating the non-sensitivity of Al incorporation towards the temperature at this range. However, the PL linewidth is narrowed from 12.7 nm at 1055 °C to below 10.5 nm at higher temperature (1074 - 1087 °C), which could be attributed to the improved crystal quality at elevated growth temperature.

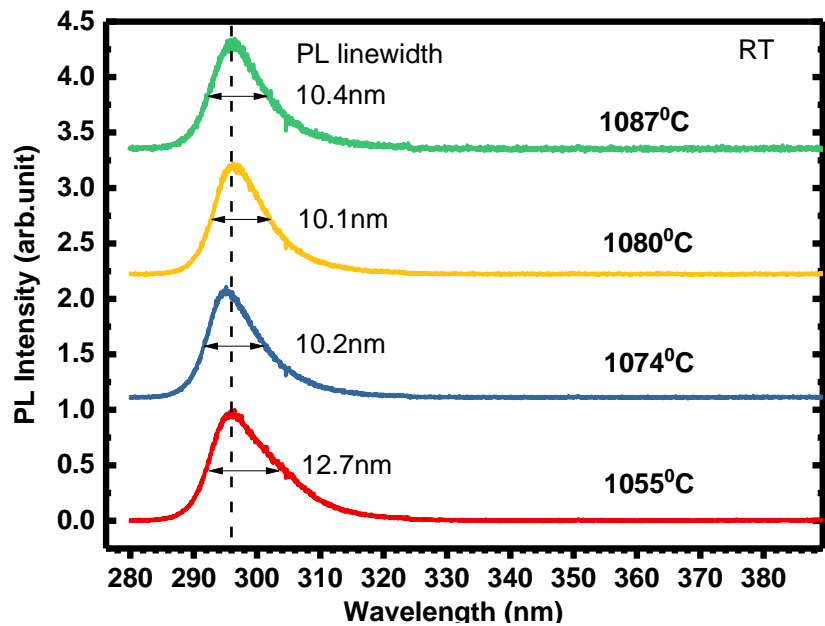


**Figure 5.13** Normalized RT PL of AlGaIn overgrowth samples grown at various temperatures.

## 5.4 Conclusion

A two-step overgrowth technology is developed to grow semi-polar (11-22) AlGa<sub>N</sub> on overgrown GaN on micro-rod templates to address the cracking issue and improve the crystal quality. 2 μm-thick (11-22) AlGa<sub>N</sub> layers with the Al composition ranging from 32.0 % to 55.3 % and corresponding PL emission ranging from 309 nm to 271 nm are obtained. A flat and relatively smooth surface is obtained, although the undulation and arrow-like features (or chevron) are observed on the sample surface, which becomes more and deeper with increasing Al composition. The shoulders observed in RT PL are attributed to the non-uniform Al distribution near the “chevron” regions with RT CL studies. Studies on the growth temperature effect show that the crystal quality is improved with increasing temperature, whereas the surface morphology reaches up to the best at the moderate temperature.

It is noteworthy that all AlGa<sub>N</sub> samples are crack-free across the 2 inch wafer. FWHMs of the X-ray rocking curves along the [1-100]/[11-2-3] directions are 0.292°/0.201° for 32.0% Al and 0.383°/0.206° for 55.3% Al, respectively, representing the best report for semi-polar AlGa<sub>N</sub> reported so far. These results indicate that the overgrowth technique is an effective approach to improve the crystal quality and address the cracking issue simultaneously for semi-polar (11-22) AlGa<sub>N</sub>.

## References

1. A. Khan, K. Balakrishnan, and T. Katona, *Nat. Photonics* 2, 77 (2008).
2. J. Zhang, X. Hu, A. Lunev, J. Deng, Y. Bilenko, T. M. Katona, M. S. Shur, R. Gaska, and M. A. Khan, *Jpn. J. Appl. Phys.* 44, 7250 (2005).
3. H. Hirayama, T. Yatabe, N. Noguchi, T. Ohashi, and N. Kamata, *Appl. Phys. Lett.* 91, 071901 (2007).
4. H. Amano, M. Iwaya, N. Hayashi, T. Kashima, S. Nitta, C. Wetzel, and I. Akasaki, *Phys. Stat. Sol. B* 216, 683 (1999).
5. J. P. Zhang, H. M. Wang, M. E. Gaevski, C. Q. Chen, Q. Fareed, J. W. Yang, G. Simin, and M. A. Khan, *Appl. Phys. Lett.* 80, 3542 (2002).
6. K. Balakrishnan, M. Lachab, H. C. Chen, D. Blom, V. Adivarahan, I. Ahmad, Q. Fareed, and M. A. Khan, *Phys. Stat. Sol. A* 208, 2724 (2011).
7. K. Balakrishnan, V. Adivarahan, Q. Fareed, M. Lachab, B. Zhang, and A. Khan, *Jpn J. Appl. Phys. Lett.* 49, 040206 (2010).
8. E. C. Young, F. Wu, A. E. Romanov, D. A. Haeger, S. Nakamura, S. P. Denbaars, D. A. Cohen, and J. S. Speck, *Appl. Phys. Lett.* 101, 142109 (2012).
9. Y. Zhang, J. Bai, Y. Hou, R. M. Smith, X. Yu, Y. Gong, and T. Wang, *AIP Adv.* 6, 025201 (2016).
10. T. Wang, *Semicond. Sci. Technol.* 31, 093003 (2016).
11. J. Bai, B. Xu, F. G. Guzman, K. Xing, Y. Gong, Y. Hou, and T. Wang, *Appl. Phys. Lett.* 107, 261103 (2015).
12. E. C. Young, A. E. Romanov, and J. S. Speck, *Appl. Phys. Express* 4, 061001(2011).
13. D. V. Dinh, M. Conroy, V. Z. Zubialevich, N. Petkov, J. D. Holmes, and P. J. Parbrook, *J. Cryst. Growth* 414, 94 (2015).
14. K. P. O'Donnell, R. W. Martin, and P. G. Middleton, *Phys. Rev. Lett.* 82, 237 (1999)
15. D. V. Dinh, S. N. Alam, and P.J. Parbrook, *J. Cryst. Growth* 435, 12 (2016).
16. M. Frentrup, N. Hatui, T. Wernicke, J. Stellmach, A. Bhattacharya, and M. Kneissl, *J. Appl. Phys.* 114, 213509 (2013).
17. H. Luan, X. Zhang, Z. Liang, Y. Wang, Q. Dai, H. Yang, Z. Wu, J. Zhao, and Y. Cui, *Phys. Stat. Sol. A* 214, 1600802 (2017).
18. J. Stellmach, F. Mehnke, M. Frentrup, C. Reich, J. Schlegel, M. Pristovsek, T. Wernicke, and M. Kneissl, *J. Cryst. Growth* 367, 42 (2013).

19. N. Hatui, A. A. Rahman, C. B. Maliakkal, and A. Bhattacharya, *J. Cryst. Growth* 437, 1 (2016).

# Chapter 6 Defect and Strain Analysis of Semi-polar (11-22) AlGa<sub>N</sub> Obtained with Overgrowth Technique

## 6.1 Introduction

Although growing AlGa<sub>N</sub> on a semi-polar or non-polar orientation is considered as a promising way to potentially improve the optical efficiency due to the significantly reduced electric field within the active regions, the material quality of semi-polar or non-polar AlGa<sub>N</sub> epilayers is still a fundamental problem. Owing to this obstacle, comprehensive studies on the structural characterization of a semi-polar or non-polar oriented AlGa<sub>N</sub> are quite rare. Stellmach *et al* [1-2] and Dinh *et al* [3] respectively reported the semi-polar (11-22) AlGa<sub>N</sub> layers directly grown on *m*-plane sapphire or AlN template and they performed some basic characterization. Young *et al* [4] also investigated the anisotropic properties of the tensile stress and cracking in semi-polar and non-polar AlGa<sub>N</sub>/Ga<sub>N</sub> heterostructures. However, these samples grown on planar substrates suffer from the relatively poor crystal quality, which makes the studies less impressive.

In the last chapter, a two-step overgrowth technique developed by our group has been presented to address the issue of the crystal quality as well as the wafer cracking. With such overgrowth technique, we have achieved thick (>2μm) and crack-free semi-polar (11-22) AlGa<sub>N</sub> layers with various high Al compositions grown on the top of nearly but not yet fully-coalesced Ga<sub>N</sub> overgrown on micro-rod templates, leading both cracking issue and quality improvement to be managed simultaneously [5].

In this chapter, a comprehensive investigation on the structural properties of semi-polar (11-22) AlGa<sub>N</sub> overgrowth samples was performed. The broadening behaviour in various reflections, and BSFs within the AlGa<sub>N</sub> layers are carefully checked and compared to the standard semi-polar (11-22) AlGa<sub>N</sub> counterparts. To study the strain relaxation in the semi-polar (11-22) AlGa<sub>N</sub> overgrowth samples, a triclinic unit cell model is adopted to calculate the

in-plane and out-of-plan strain. Furthermore, both the symmetric (11-22) and asymmetric (11-24) RSMs are employed to investigate the lattice tilt as well as the in-plane strain relaxation.

It is found that the crystal quality of AlGa<sub>N</sub> is significantly improved via the overgrowth approach compared with any conventional AlGa<sub>N</sub> counterparts on planar substrates. Through a detailed strain analysis, semi-polar (11-22) AlGa<sub>N</sub> layers with large lattice tilts have been found to be compressively strained instead of being conventionally tensile strained, which is advantageous to preventing cracks.

It is worth mentioning that the  $\mathbf{g} \cdot \mathbf{R} = n$  invisibility criteria [6] for stacking faults is used to investigate the anisotropic broadening behaviour of the XRD, where  $\mathbf{g}$  is the diffraction vector,  $\mathbf{R}$  is the stacking fault displacement vector and  $n$  is an integer (including zero). Under this criteria, if the XRC FWHM of the diffraction vector  $\mathbf{g}$  is broadened by the stacking fault (displacement vector,  $\mathbf{R}$ ), the  $\mathbf{g} \cdot \mathbf{R}$  product must be non-integer and the stacking fault has a substantial component along the X-ray incident direction. Dislocations with a Burgers vector  $\mathbf{b}$  can also broaden the XRC of diffraction vector  $\mathbf{g}$  when the  $\mathbf{g} \cdot \mathbf{b}$  is non-zero.

## 6.2 Experimental Details

Samples studied in this chapter are the overgrown samples AO1-AO8 with Al composition ranging from 32.0% to 55.3%. More details about growth parameters could be found in Chapter 5.

Crystal quality of the AlGa<sub>N</sub> epilayers is structurally characterized by XRD (Bruker D8 diffractometer) with azimuth-dependent rocking curve measurements in the on-axis (11-22) plane. And it is further investigated by other off-axis planes such as (000 $n$ ) and ( $n$ 0- $n$ 0) planes ( $n=1, 2, 3$ ). To check the BSFs of all samples, PL emission of AlGa<sub>N</sub> at LT is measured by using a doubled-frequency argon ion laser with an excitation wavelength of 244 nm. In order to study the strain of the semi-polar AlGa<sub>N</sub> as a function of Al composition, multiple on- and off-axis XRD measurements have been conducted. Symmetric (11-22) RSM measured along both the [1-100] and the [11-2-3] in-plane directions and asymmetric (11-24) RSM measured along [11-2-3] direction are also analysed to check the lattice tilt of the AlGa<sub>N</sub>.

## 6.3 Defect Reduction Analysis

### 6.3.1 On-axis (11-22) reflection

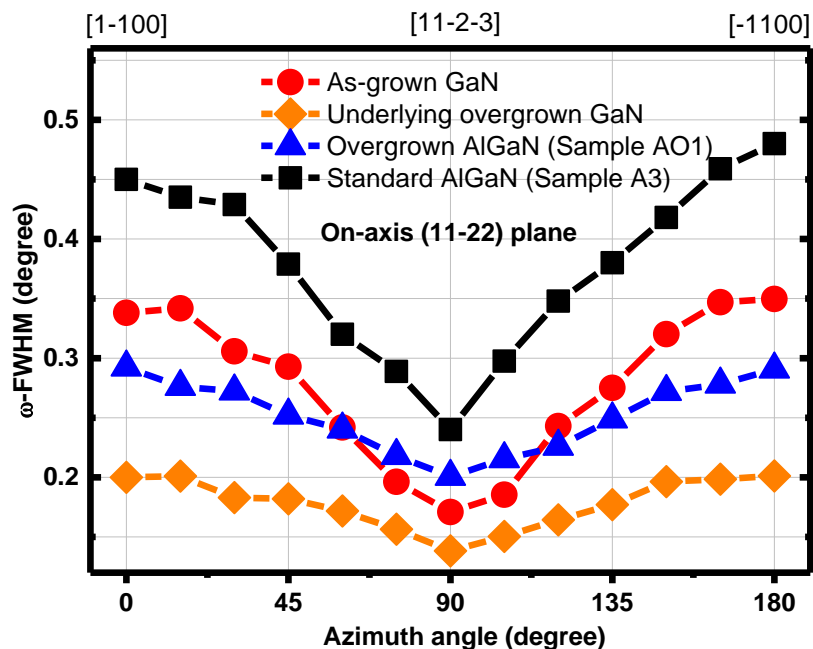


**Figure 6.1** Azimuth dependent XRC FWHMs of each layer in the overgrown AlGaIn (Sample AO1). Data of the standard AlGaIn (Sample A3) is also plotted for comparison.

XRD rocking curves of the on-axis (11-22) plane have been measured with an azimuth angle ranging from  $0^{\circ}$  to  $180^{\circ}$ . As an example, the FWHM of the XRD rocking curves measured on the sample AO1 with 32.0% Al are presented in Figure 6.1, showing a typical anisotropic behaviour for a semi-polar sample, namely, the lowest FWHM along [11-2-3] (i.e.,  $90^{\circ}$  azimuth angle) and the largest FWHM along [1-100] (i.e.,  $0^{\circ}$  azimuth angle). For comparison, the FWHMs of the underlying non-coalesced GaN, an as-grown (11-22) GaN (used for the fabrication of a micro-rod template), and a standard (11-22) AlGaIn (sample A3,  $\lambda = 310$  nm, non-overgrown) with similar Al composition of 32% are also presented.

Compared with the as-grown GaN, the crystal quality of the non-coalesced GaN is greatly improved, which has been attributed to the effective blockage of the defects due to the overgrowth technique. The overgrown GaN (although non-coalesced) serves as a good template for the subsequent AlGaIn growth, thus leading to the further overgrown AlGaIn with improved crystal quality. Compared with the standard (11-22) AlGaIn sample with a thickness of  $2 \mu\text{m}$  and Al composition of  $\sim 32\%$  obtained on the planar sapphire substrate using a HT AlN buffer, the crystal quality of overgrown AlGaIn has been significantly improved, confirmed by the XRD rocking curve FWHMs of  $0.292^{\circ}$  along [1-100] direction and  $0.201^{\circ}$  along [11-2-3]

direction. In contrast, the standard AlGaIn exhibits the FWHMs of  $0.456^\circ$  along [1-100] and  $0.245^\circ$  along [11-2-3].

Note that all semi-polar GaN and AlGaIn samples exhibit anisotropic broadening in XRD rocking curves: FWHM along [1-100] is broader than that along [11-2-3]. Such anisotropic property is common in semi- or non- polar structures and has been widely reported [6-7]. It has been suggested that many factors, such as mosaic tilt of epilayers, stacking faults (BSFs or PSFs) and dislocations, could contribute to anisotropic broadening of XRC [8].

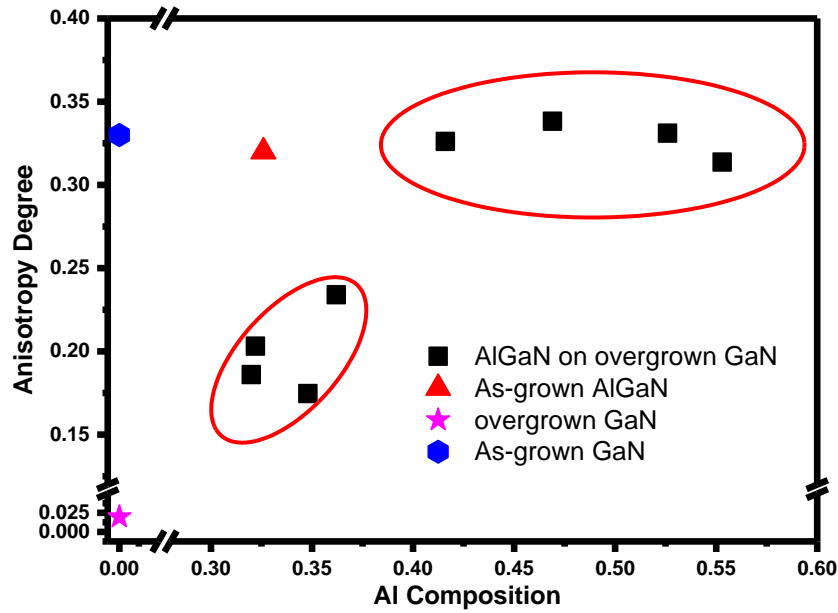


**Figure 6.2 Anisotropy degree of XRC FWHMs as a function of Al composition. Data of the as-grown GaN, overgrown GaN and standard AlGaIn is also plotted for comparison.**

Here, in order to analyse the in-plane anisotropy of crystal quality, we define the anisotropy degree as:

$$\rho = \frac{FWHM_{1-100} - FWHM_{11-2-3}}{FWHM_{1-100} + FWHM_{11-2-3}} \quad (6.1)$$

where  $FWHM_{1-100}$  and  $FWHM_{11-2-3}$  corresponds to the values measured along the [1-100] and the [11-2-3] directions, respectively.

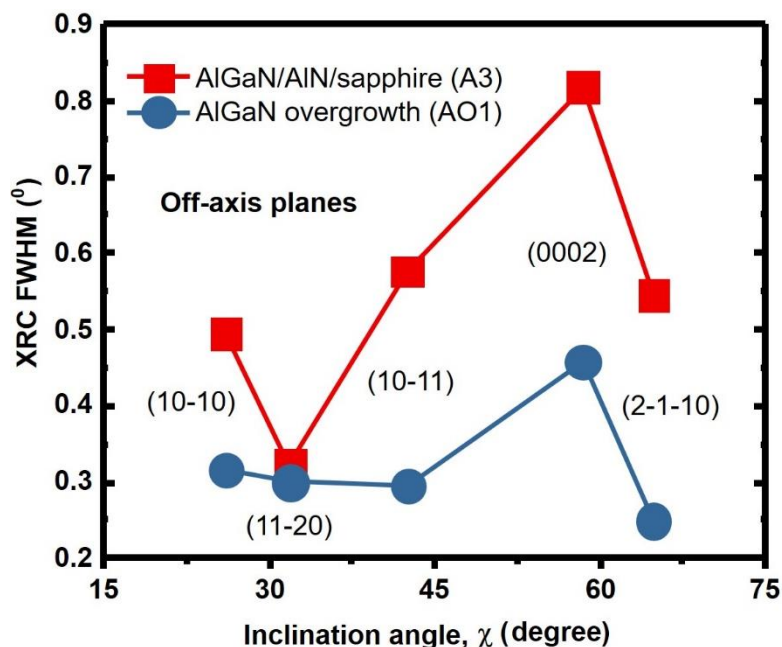
The anisotropy degree obtained as a function of Al composition is shown in Figure 6.2. It can be seen that the XRD anisotropy of high-quality overgrown GaN is almost smeared out leading to  $\rho = 0.02$ , whereas standard semi-polar GaN without using any overgrowth technique exhibits a strong anisotropic feature, typically  $\rho = 0.33$ . Similarly, the overgrown AlGaIn ( $\rho = 0.17$ , for 32.0% Al) also shows weaker anisotropic features than the standard AlGaIn ( $\rho = 0.30$ , with 32% Al). According to the  $\mathbf{g} \cdot \mathbf{R} = n$  invisibility criteria mentioned above, BSFs (mainly  $I_1$  type) are visible in the (11-22) reflection. Given a significant reduction in BSF density for our overgrown samples (see data in Figure 6.6), one can assume that BSFs and/or their partial

dislocations may be the predominating source for the strong anisotropic broadening of the XRD rocking curves.

On the other hand, it can be observed in Figure 6.2, the anisotropy degree is around 0.2 (the left circle) for the overgrown AlGa<sub>N</sub> samples with low Al composition below from 0.40, while the anisotropy degree remains around 0.33 for higher Al composition samples (the right circle). Since the BSF densities in all the overgrown AlGa<sub>N</sub> samples are actually comparable, confirmed by the NBE/BSFs PL intensity ratios measured at 10 K (all around 90 ~ 110 %), the enhanced anisotropy degree as a result of increasing Al composition could be mainly attributed to the lattice tilt, which is in turn due to an increase in lattice mismatch between AlGa<sub>N</sub> and GaN (see data in Figure 6.8).

### 6.3.2 Off-axis reflections

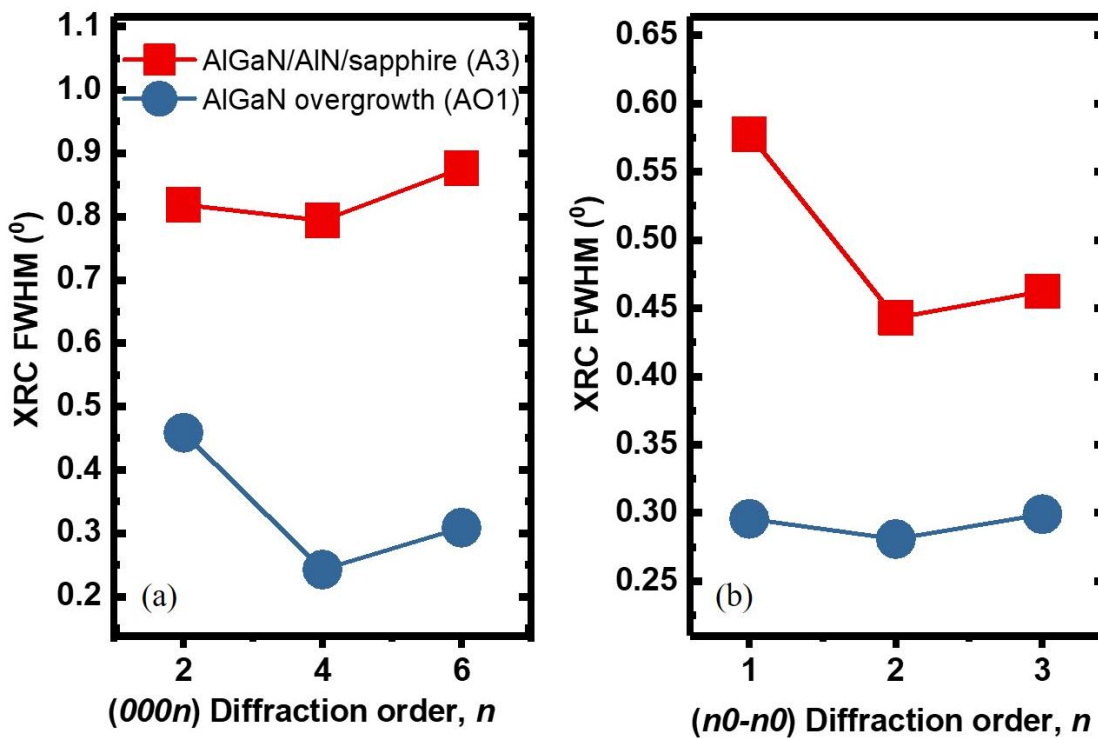
In order to study the in-plane mosaic twist of the (11-22) AlGa<sub>N</sub> samples, XRC measurements are performed in a skew symmetric geometry for off-axis planes. These planes have an inclination angle  $\chi$  with respect to the on-axis (11-22) plane at various azimuth angles and their XRCs are normally broadened by the in-plane misorientation. Sample A3 (standard AlGa<sub>N</sub>) and AO1 (overgrown AlGa<sub>N</sub>) with similar Al composition ~ 32% are analysed as examples and the results are shown in Figure 6.3.



**Figure 6.3 XRC FWHMs of the off-axis planes with different inclination angles with respect to the (11-22) plane. The azimuth angle for each reflection varies.**

It can be seen that, apart from (11-20) plane, the XRCs of the overgrowth sample are narrowed down by 38% ~ 48% compared to the standard AlGa<sub>N</sub> on planar substrate sample,

indicating a significant improvement in the microstructural quality with the overgrowth technique. Particularly, the (0002) reflection with the largest FWHM in both standard and overgrown samples exhibits the most significant improvement. This implies the great reduction of BSF-related partial dislocations and perfect dislocations. However, it shows no big change in the XRC linewidth of the (11-20) plane. Given that the (11-20) reflection is not sensitive to the BSFs based on the criteria mention above, it may imply that the major defect reduction associated with the two-step overgrowth technique lies on the BSFs and/or related partial dislocations.



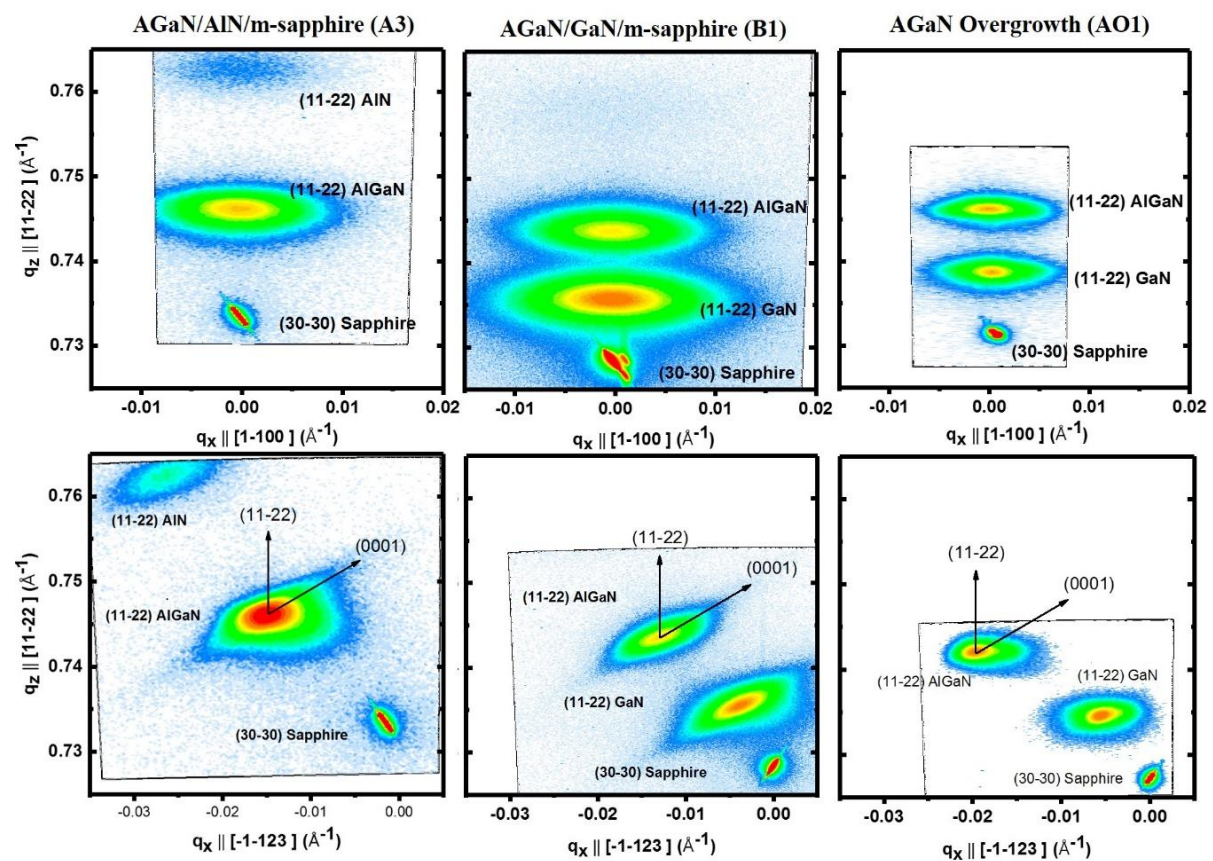
**Figure 6.4 XRC FWHMs of the (000n) (a) and the (n0-n0) (b) reflections at different diffraction order.**

Figure 6.4 shows the FWHMs of the XRC for the (000n) and (n0-n0) reflections. From the standard AlGaIn sample to the overgrowth sample, as the diffraction order n increases, the XRC FWHMs decrease by 71%, 70% and 65% for the (000n) reflections and decrease by 37%, 36% and 35% for the (n0-n0) reflections. It has been reported that different off-axis planes are broadened by different broadening factors. According to the  $\mathbf{g} \cdot \mathbf{R} = n$  invisibility criteria, the off-axis planes of (n0-n0) expect for the (30-30) reflection are broadened by BSFs, and the FWHMs of the c-plane (000n) diffraction is related to the partial dislocations and/or perfect dislocations (they are not sensitive to either BSFs or PSFs) [9]. Since there is a significant improvement in the XRC FWHMs for most off-axis planes, we conclude that our two-step

overgrowth technique could reduce both the BSFs and partial dislocations and/or perfect dislocations dramatically.

### 6.3.3 (11-22) RSMs

In order to further understand the XRD broadening of semi-polar AlGaN with different structures, the symmetric (11-22) reciprocal space mappings are taken along two primary in-plane directions, namely the [1-100] direction ( $0^\circ$  azimuth angle) and the [11-2-3] direction ( $90^\circ$  azimuth angle), as shown in Figure 6.5.



**Figure 6.5 (11-22) RSMs measured along both in-plane directions ( $0^\circ$  and  $90^\circ$  azimuth angle) for standard AlGaN samples (A3 and B1) and AlGaN overgrowth sample (AO1).**

For the RSMs measured along both in-plane directions, the diffraction spots of semi-polar (11-22) (Al)GaN in overgrowth samples exhibit smaller broadening than those in standard samples obtained on the planar substrates, indicating the overall improvement of crystal quality of the AlGaN and GaN epilayers. While the reciprocal lattice points of the AlGaN, GaN (or AlN) and the sapphire substrate are aligned in a vertical line in all  $0^\circ$  RSMs, a tilt angle of  $1.1^\circ$ ,  $1.0^\circ$  and  $1.5^\circ$  between AlGaN and the substrate is observed in  $90^\circ$  RSMs for the AlGaN/AlN/sapphire (A3,  $\lambda = 310$  nm), the AlGaN/GaN/AlN/sapphire (B1,  $\lambda = 309$  nm) and the AlGaN overgrowth sample (AO1,  $\lambda = 309$  nm), respectively. The large mosaic tilt observed

in the overgrowth sample is believed to be able to effectively release the strain within the AlGaIn layers, which will be discussed further later.

It is noteworthy that in the  $90^\circ$  RSMs of the standard AlGaIn samples, the A3 and B1, a distinct streak (or broadening) which has an inclination angle of  $\sim 58^\circ$  with respect to the (11-22) plane can be observed. Such a streak indicates the  $c$  direction and therefore is attributed to the diffuse scattering of the BSFs [10-12]. With the overgrowth technique in the sample AO1, however, the BSF-related broadening becomes much weaker, implying that a great reduction in the BSF density has been achieved.

#### 6.3.4 BSFs in LT PL

PL measurements at LT ( $T=10\text{K}$ ) are further carried out to investigate the BSFs-related emission property. PL spectra of sample A3 and AO1 with the similar Al composition are displayed as examples shown in Figure 6.6. The BSFs-related emission and the NBE emission can be clearly distinguished in both spectra. The intensity ratio, NBE/BSFs normally used to rapidly check the BSFs density, increases from 38% for sample A3 to 103% for AO1, which indicates the less BSFs existing in the overgrowth sample. More LT PL measurements show that the NBE/BSFs ratio for the standard AlGaIn samples is typically 30-40% while the ratio is all around 90-110% for the overgrowth samples, which further supports the conclusion.

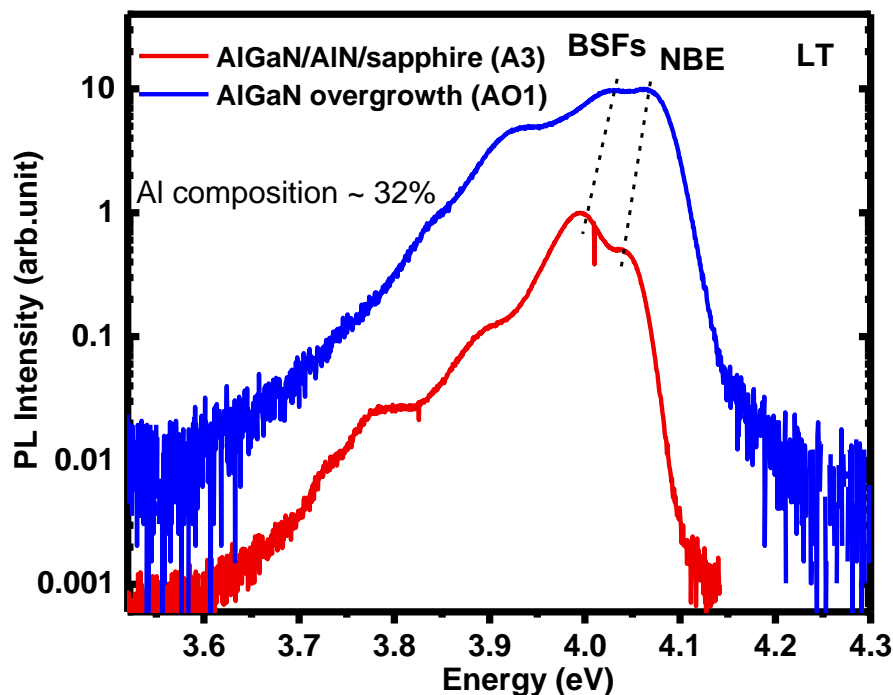


Figure 6.6 LT PL spectra of the standard AlGaIn (A3) and overgrown AlGaIn (AO1).

## 6.4 Strain Relaxation

### 6.4.1 Strain modelling in semi-polar (11-22)

Although the study of strain in AlGaIn/GaN has been well established on traditional *c*-plane samples, it becomes complicated in semi-polar structures due to reduced symmetry and more complex distortion. Based on a triclinic unit cell mode, Frentrup *et al* [13] have developed an approach to determining the lattice parameters of semi-polar (11-22) structures using multiple on- and off-axis XRD measurement in a  $\omega/2\theta$  mode. The calculation principle of this approach could be briefly described as follows.

In the traditional *c*-plane layers, the equation of the interplanar spacing  $d_{hkl}$  of an ideal hexagonal crystal can be described by Equation 3.9 in chapter 3. However, due to lattice distortion in semi-polar orientated epilayers, unit cell base angles in addition to lattice constants, i.e. ( $a, b, c, \alpha, \beta, \gamma$ ), are needed. Regarding the distorted hexagonal cell as a triclinic cell, then the expression of  $d_{hkl}$  will be expressed by:

$$\frac{1}{d_{hkl}^2} = \frac{1}{V^2} (S_{11}h^2 + S_{22}k^2 + S_{33}l^2 + 2S_{12}hk + 2S_{23}kl + 2S_{13}hl) \quad (6.2)$$

with the volume of the unit cell  $V$  and the parameters  $S_{ij}$  described by the following equations.

$$V = abc\sqrt{1 - \cos^2 \alpha - \cos^2 \beta - \cos^2 \gamma + 2\cos\alpha \cos\beta \cos\gamma} \quad (6.3)$$

$$S_{11} = b^2c^2 \sin^2 \alpha \quad (6.4)$$

$$S_{22} = a^2c^2 \sin^2 \beta \quad (6.5)$$

$$S_{33} = a^2b^2 \sin^2 \gamma \quad (6.6)$$

$$S_{12} = abc^2(\cos\alpha \cos\beta - \cos\gamma) \quad (6.7)$$

$$S_{23} = a^2bc(\cos\beta \cos\gamma - \cos\alpha) \quad (6.8)$$

$$S_{13} = ab^2c(\cos\gamma \cos\alpha - \cos\beta) \quad (6.9)$$

For the very small distortions in semi-polar (11-22) layers, where the deviation of the basis angles  $\delta_i$  ( $i=\alpha, \beta, \gamma$ ) is typically in the order of  $|\delta_i| < 0.5^\circ$ , the first-order Taylor series approximation for the sine and cosine terms can be used in Equation 6.3 - 6.9 to simplify the expression. Inserting these simplified equations into Equation 6.2, the interplanar spacing  $d_{hkl}$  of  $\{h k i l\}$  planes in a triclinic lattice is expressed as:

$$\frac{1}{d^2} = \frac{4}{3} \frac{(h^2+k^2+l^2)}{a^2} + \frac{l^2}{c^2} + \frac{(8h^2+8k^2+20hk)}{3\sqrt{3}a^2} \delta_\gamma + \frac{(4hl+8kl)\delta_\alpha+(8hl+4kl)\delta_\beta}{3ac} \quad (6.10)$$

where the two additional terms compared to the hexagonal crystal describe the distortion within the basal plane and the shearing between the *c*-axis and the basal plane, respectively.

The expression could be simplified even further by inserting the correlation between  $\delta_\alpha$  and  $\delta_\gamma$  in the semi-polar (11-22) structure namely  $\delta_\alpha = \delta_\gamma$  as following:

$$\frac{1}{d^2} = \frac{4}{3} \frac{(h^2+k^2+l^2)}{a^2} + \frac{l^2}{c^2} + \frac{(8h^2+8k^2+20hk)}{3\sqrt{3}a^2} \delta_\gamma + \frac{4(hl+kl)}{ac} \delta_\alpha \quad (6.11)$$

Based on the above equation, lattice parameters and unit cell base angles of our overgrown AlGaN can be extracted. Below is an example using the overgrown AlGaN sample AO3. A series of multiple on- and off-axis  $\omega/2\theta$  measurements for the overgrown AlGaN and the GaN underneath have been carried out, respectively, namely, (0002), (0004), (11-20), (2-1-12), (-12-1-2), (11-22), (11-24), (1-103) and (1-101), as shown in Table 6.1. These on- and off-axis planes with various inclination angle with respect to the surface are measured at various azimuth angles, which could provide more accurate information on the in-plane and out-of-plane distances as well as the shearing of the crystal lattice.

**Table 6.1 On- and off-axis  $\omega/2\theta$  measurements for GaN and AlGaN in sample AO3.**

(11-22) underlying GaN			
h k l	$\omega$ /degree	$\Delta\omega$ /FWHM	$d_{hkl}/\text{\AA}$ measured
0002	17.283	0.195	2.5928
0004	36.348	0.229	1.2997
11-20	28.887	0.241	1.5946
2-1-1-2	34.559	0.192	1.3580
-12-1-2	34.766	0.212	1.3509
11-22	34.500	0.243	1.3600
11-24	49.958	0.230	1.0062
1-103	31.739	0.205	1.4643
1-101	18.517	0.326	2.4255
(11-22) AlGaN			
h k l	$\omega$ /degree	$\Delta\omega$ /FWHM	$d_{hkl}/\text{\AA}$ measured
0002	17.536	0.462	2.5566
0004	37.055	0.418	1.2783
11-20	29.255	0.335	1.5762
2-1-1-2	35.116	0.310	1.3391
-12-1-2	35.193	0.278	1.3366
11-22	34.900	0.278	1.3463
11-24	50.770	0.328	0.9944
1-103	32.165	0.441	1.4470
1-101	18.578	0.362	2.4179

Based on the Equation 6.11, with the software MATLAB or EXCEL, the lattice parameters and basis angles of the AlGa<sub>N</sub> and GaN have been obtained:  $a = (3.1743 \pm 0.0001) \text{ \AA}$ ,  $c = (5.1947 \pm 0.0001) \text{ \AA}$ ,  $\alpha = (90.000 \pm 0.020)$  and  $\gamma = (119.990 \pm 0.010)$  for the underlying GaN;  $a = (3.1501 \pm 0.0001) \text{ \AA}$ ,  $c = (5.1091 \pm 0.0001) \text{ \AA}$ ,  $\alpha = (89.990 \pm 0.020)$  and  $\gamma = (119.990 \pm 0.020)$  for the AlGa<sub>N</sub>. The basis angles  $\alpha$  and  $\gamma$  in both layers are quite close to their respective counterparts in an unstrained state, indicating negligible distortion or shearing as a result of significant strain relaxation.

With the lattice parameters derived above, the out-of-plane and in-plane strain in the AlGa<sub>N</sub> and the GaN layers can be then deduced from equations below:

$$\varepsilon_{11-22} = \frac{d_{11-22}^{meas} - d_{11-22}^0}{d_{11-22}^0} \quad (6.12)$$

$$\varepsilon_{11-2-3} = \frac{L_{11-2-3}^{meas} - L_{11-2-3}^0}{L_{11-2-3}^0} \quad (6.13)$$

$$\varepsilon_{1-100} = \frac{L_{1-100}^{meas} - L_{1-100}^0}{L_{1-100}^0} \quad (6.14)$$

where  $d$  and  $L$  are the interplanar spacing and distance, respectively; index “0” and “meas” denote the unstrained and strained layers, respectively. For the unstrained layers, the interplanar spacing and the in-plane distance obey the linear Vegard’s law,

$$d_{hkl}^0 = x d_{hkl}^{0,AlN} + (1-x) d_{hkl}^{0,GaN} \quad (6.15)$$

$$L_{hkl}^0 = x L_{hkl}^{0,AlN} + (1-x) L_{hkl}^{0,GaN} \quad (6.16)$$

where  $x$  is the Al composition of the AlGa<sub>N</sub> alloy. For the lattice parameters and elastic constants used in this work, please refer to Ref. [13].

#### 6.4.2 Analysis for the strain calculation

**Table 6.2 Calculated in-plane and out-of-plane strain in the AlGa<sub>N</sub> overgrowth sample (AO3). ‘+’ means tensility; ‘-’ means compression.**

Epilayers	In-plane strain		Out-of-plane strain
	$\varepsilon_{11-2-3}$	$\varepsilon_{1-100}$	$\varepsilon_{11-22}$
Underlying GaN	$-5.8482 \times 10^{-5}$	$-4.7737 \times 10^{-3}$	$+1.1651 \times 10^{-3}$
AlGa <sub>N</sub>	$-1.1895 \times 10^{-3}$	$-3.3888 \times 10^{-3}$	$+1.6665 \times 10^{-3}$

The calculated results of the in-plane strain and out-of-plane strain are summarized in Table 6.2. It has been found that both the AlGaIn and the underlying GaN exhibit anisotropic in-plane compressive strain. For the underlying GaN, the in-plane strain along [11-2-3] is  $-5.8482 \times 10^{-5}$ , approaching to zero and thus indicating almost complete relaxation along this direction, while the strain along [1-100] is two orders higher than that along [11-2-3], showing much higher compressive strain.

This anisotropic strain in the overgrown GaN layer could be understood from the specific material overgrowth process. The GaN overgrowth initiated from the sidewalls of micro-rods and advanced along the *c* and *a* direction, where the *c*-oriented growth is much faster than the *a*-oriented growth. The predominant *c*-oriented growth should lead to large strain relaxation along the [11-2-3] direction which is the in-plane projection of the *c*-direction. The voids, formed when the *c*-oriented growth facet meets with the *a*-oriented growth facet, can effectively block the BSFs and cause either annihilation or termination of dislocations [14] along with the strain relaxation simultaneously. The second GaN coalescence which is not completely finished further maintains the strain relaxation of the GaN layer. Moreover, the anisotropic lattice mismatch between GaN and the sapphire substrate, which is 1% along the *c*-direction but 16% along the *m*-direction [15], respectively, also probably contributes to the in-plane strain anisotropy.

For the AlGaIn layer, it exhibits compressive instead of tensile strain. The strain along the [1-100] is about three times larger than that along the [11-23] direction. Due to the non-coalesced GaN underneath, the AlGaIn growth proceeds laterally at the initial stage (evidenced by the formation of a triangle void observed in the circle in Figure 5.3 in Chapter 5). Similar to the GaN overgrowth, the lateral overgrowth along the *c*-direction in the AlGaIn also results in much larger strain relaxation than that along the [11-2-3] direction. Furthermore, the strain relaxation can effectively occur as a result of residual voids formed when the AlGaIn was grown on the non-coalesced GaN. Therefore, the great improvement in the crystal quality of AlGaIn is attributed not only to the high-quality GaN underneath, but also to the great strain relaxation which provides less chance for the formation of dislocations or wafer cracking.

#### 6.4.3 Lattice tilt in (11-22) and (11-24) RSMs

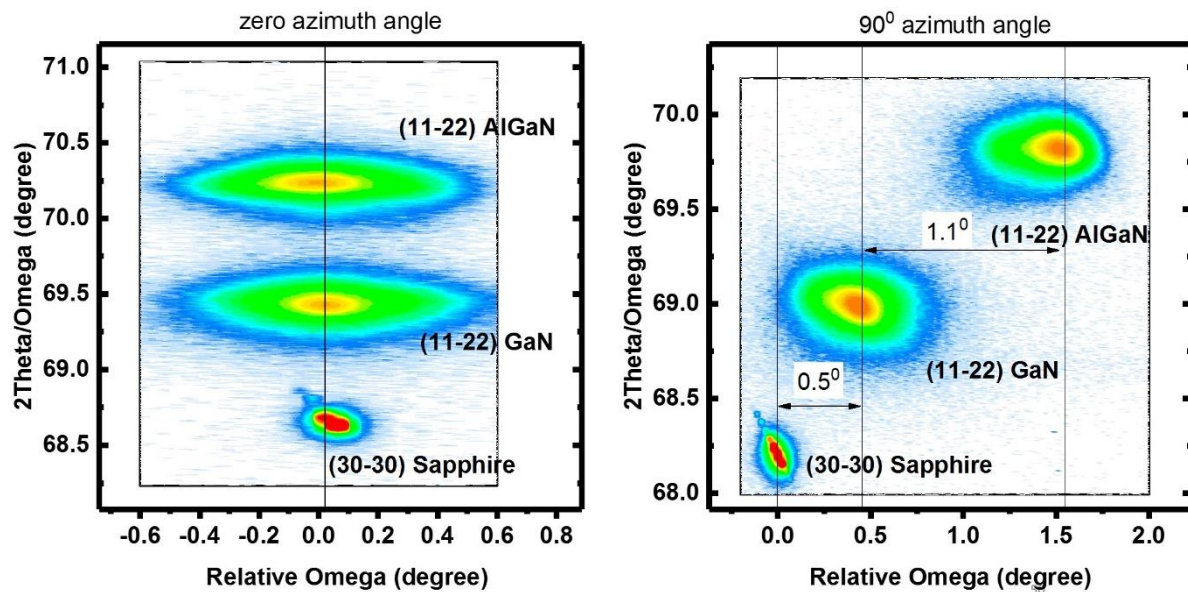


**Figure 6.7 (11-22)  $2\theta/\omega$  maps measured at both  $0^\circ$  and  $90^\circ$  azimuth angle. The tilt angle (referring to the omega difference) between different layers can be easily read from maps.**

The strain has been further investigated by XRD reciprocal space mapping measurements in which the distortion or relaxation of the reciprocal lattice point (RLP) can be clearly observed. As an example, Figure 6.7 shows the  $2\theta/\omega$  mapping of the AlGaN with Al composition of 36.2% (sample AO4), measured along a symmetrical direction, i.e., (11-22). The corresponding RSM with a reciprocal coordinate  $q_x$  and  $q_z$  is shown in Figure. 6.5.

As shown in both figures, when the (11-22) RSM is measured along [1-100], the RLPs of the GaN and the AlGaN nearly stand in a straight line with the RLP of sapphire, showing that the AlGaN is coherently grown on the GaN layers along this direction. However, when measured along [11-2-3], the mosaic tilt between the three layers can be clearly observed. A tilt angle of  $0.5^\circ$  is exhibited for the underlying GaN layer with respect to the m-plane sapphire while a tilt of  $1.1^\circ$  for the AlGaN layer with respect to the underlying GaN. This is in good agreement with the above analysis that  $\varepsilon_{1-100}$  is much larger than  $\varepsilon_{11-2-3}$  in both the GaN and the AlGaN. It has been reported by Tyagi *et al* [16] that lattice tilt could cause partial strain relaxation via misfit dislocation generation at the AlGaN/GaN interface and even be used to quantify the strain relaxation. In comparison with the tilt angles reported by other groups [3, 17], the increased tilt angle in our AlGaN sample indicates enhanced great strain relaxation, which is consistent with the residue strain obtained above.

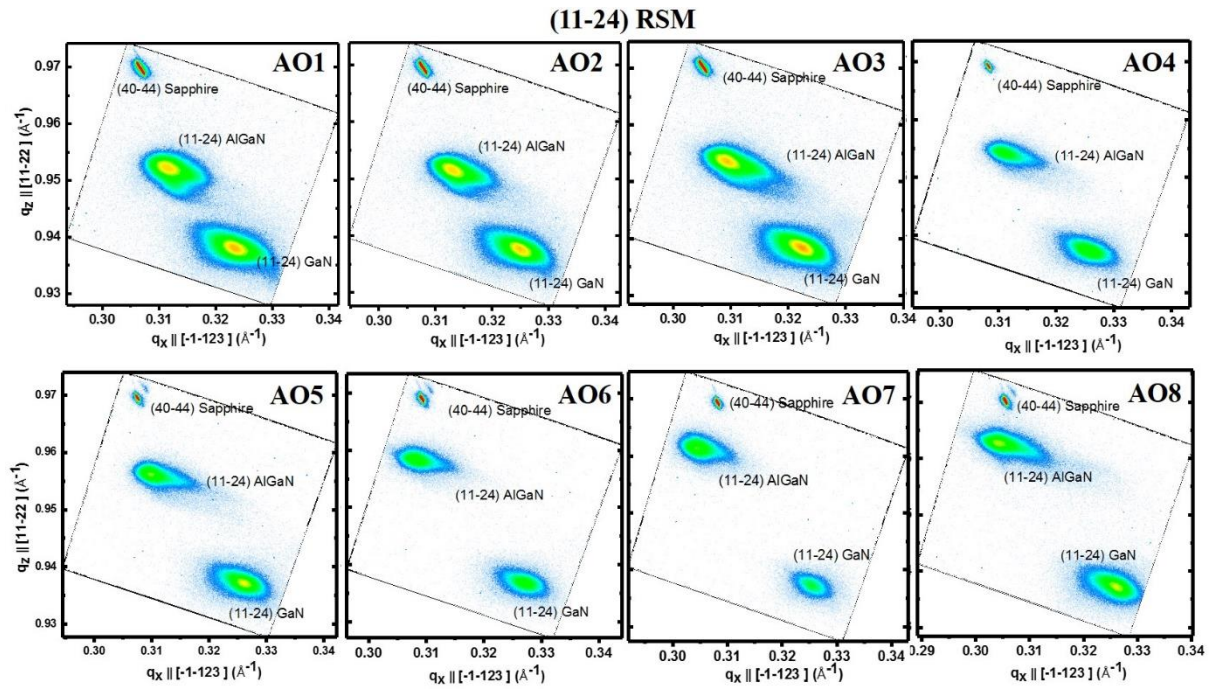


**Figure 6.8 Asymmetric (11-24) RSMs measured at  $90^\circ$  azimuth angle for AlGaIn overgrowth samples with various Al compositions.**

The asymmetric (11-24) RSMs measured at  $90^\circ$  azimuth angle, namely the  $c$ -axis projection are used to further check the relaxation along the in-plane direction, as shown in Figure 6.8.

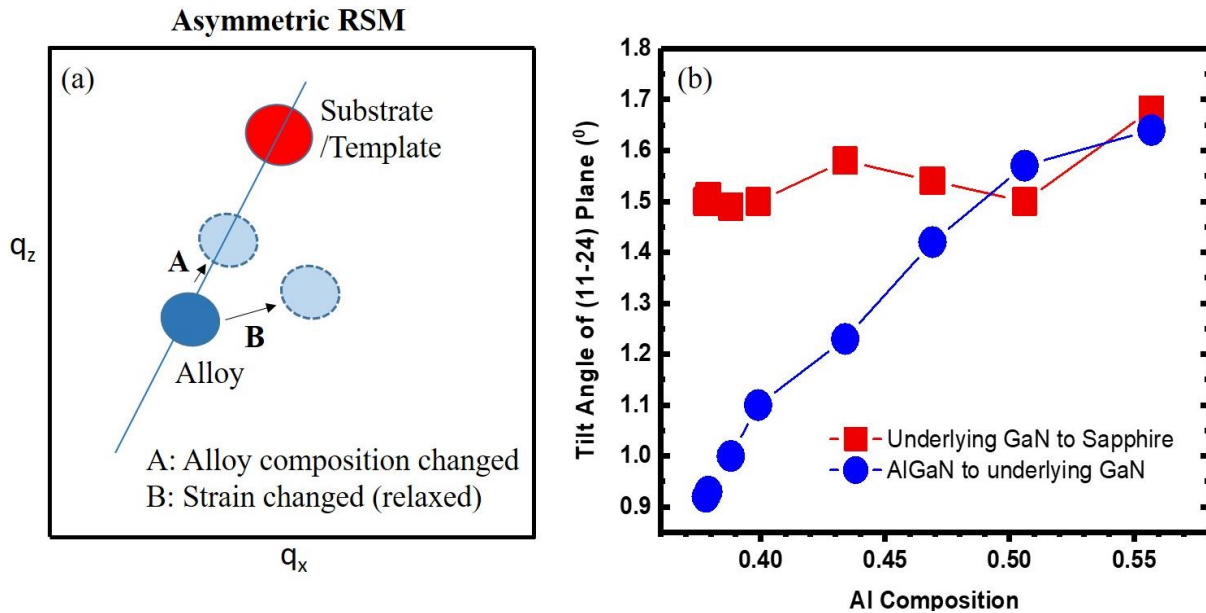


**Figure 6.9 (a) Illustration of the RLP change in an asymmetric RSM. (b) Tilt angles of (11-24) plane extracted from RSMs as a function of the Al composition.**

It has been understood that both the alloy composition and strain can make the RLP shift in the asymmetric RSM. As illustrated in Figure 6.9 (a), if only the alloy composition is changed (no strain), the RLP will shift along a straight line to the substrate (or template),

whereas if only the strain is changed within the alloy (but no composition change), the RLP will deviate from this line, showing a lattice tilt.

From the overgrowth AlGa<sub>N</sub> sample AO1 to the AO8 (Figure 6.8), we can see that the RLPs of the AlGa<sub>N</sub> become closer to the RLPs of the sapphire substrate (or away from the RLPs of the Ga<sub>N</sub>), indicating the increase of the alloy composition. In addition, similar to the symmetric (11-22) RSMs measured along the [11-2-3] direction, a lattice tilt between the epilayer and the substrate is also observed, which confirms the strain relaxation along the in-plane direction. Interestingly, the tilting direction from the Ga<sub>N</sub> to sapphire is opposite to the tilting direction from the AlGa<sub>N</sub> to the Ga<sub>N</sub>, which possibly results from the different strain state between them.

The tilt angles of the (11-24) plane extracted from the RSMs are shown in Figure 6.9 (b) as a function of the Al composition. As the Al composition increases, the tilt angle from the Ga<sub>N</sub> to sapphire remains similar being around  $1.5^\circ$  while the tilt angle from the AlGa<sub>N</sub> to the Ga<sub>N</sub> increases gradually. Such increasing tilt angles could be attributed to the more misfit dislocations at the AlGa<sub>N</sub>/Ga<sub>N</sub> interface due to the larger lattice mismatch, which would result in strain relaxation.

## 6.5 Conclusion

Crack-free semi-polar (11-22) AlGa<sub>N</sub> with a  $\sim 2$   $\mu\text{m}$  thickness and high Al composition of up to 55.3% have been successfully grown on our specially designed overgrown Ga<sub>N</sub> on a micro-rod template by MOCVD. The FWHMs of the X-ray rocking curves along the [1-100]/[11-2-3] directions are  $0.292^\circ/0.201^\circ$  for 33.2% Al and  $0.381^\circ/0.206^\circ$  for 55.3% Al, respectively, representing the best report for semi-polar AlGa<sub>N</sub> reported so far. XRD studies of the on-axis and off-axis planes show a dramatic improvement of the crystal quality compared to the standard AlGa<sub>N</sub> sample. Detailed studies of the strain have been investigated by means of multiple on- and off-axis XRD measurements along with the (11-22) symmetric and the (11-24) asymmetric RSM measurements, showing compressive instead of tensile in-plane strain and also significant strain relaxation in our AlGa<sub>N</sub> layers. It indicates that our overgrowth method is an effective way to both release the strain and improve the crystal quality simultaneously, which plays an important role in developing semi-polar deep UV emitters with a step-change in optical performance.

## References

1. J. Stellmach, F. Mehnke, M. Frentrup, C. Reich, J. Schlegel, M. Pristovsek, T. Wernicke and M. Kneissl, *J. Cryst. Growth* 367, 42 (2013).
2. J. Stellmach, M. Frentrup, F. Mehnke, M. Pristovsek, T. Wernicke and M. Kneissl, *J. Cryst. Growth* 355, 59 (2012).
3. D. V. Dinh, M. Conroy, V. Z. Zubialevich, N. Petkov, J. D. Holmes, and P. J. Parbrook, *J. Cryst. Growth* 414, 94 (2015).
4. E. C. Young, C. S. Gallinat, A. E. Romanov, A. Tyagi, F. Wu and J. S. Speck, *Appl. Phys. Express* 3, 111002 (2010).
5. Z. Li, L. Jiu, Y. Gong, L. Wang, Y. Zhang, J. Bai and T. Wang, *Appl. Phys. Lett.* 110, 082103 (2017).
6. M. A. Moram, C. F. Johnston, J. L. Hollander, M. J. Kappers and C. J. Humphreys, *J. Appl. Phys.* 105, 113501 (2009).
7. N. Hatui, A. A. Rahman, C. B. Maliakkal and A. Bhattacharya, *J. Cryst. Growth* 437, 1 (2016).
8. M. B. Mclaurin, A. Hirai, E. Young, F. Wu, and J. S. Speck, *Jpn J. Appl. Phys.* 47, 5429 (2008).
9. Q. Sun, B. Leung, C. D. Yerino, Y. Zhang and J. Han, *Appl. Phys. Lett.* 95, 231904 (2009).
10. M. Pristovsek, M. Frentrup, Y. Han and C. Humphreys, *Phys. Status Solidi B*, 253, 61 (2016).
11. S. Lazarev, S. Bauer, T. Meisch, M. Bauer, I. Tischer, M. Barchuk, K. Thonke, V. Holy, F. Scholz and T. Baumbach, *J. Appl. Cryst.* 46, 1425 (2013).
12. G. Zhao, L. Wang, S. Yang, H. Li, H. Wei, D. Han and Z. Wang, *Sci. Rep.* 6, 20787 (2016).
13. M. Frentrup, N. Hatui, T. Wernicke, J. Stellmach, A. Bhattacharya, and M. Kneissl, *J. Appl. Phys.* 114, 213509 (2013).
14. J. Bai, Y. Gong, K. Xing, X. Yu and T. Wang, *Appl. Phys. Lett.* 102, 101906 (2013).
15. M. Tsuda, H. Furukawa, A. Honshio, M. Iwaya, S. Kamiyama, H. Amano and I. Akasaki, *Phys. Stat. Sol. B* 243, 1524 (2006).
16. A. Tyagi, F. Wu, E. C. Young, A. Chakraborty, H. Ohta, R. Bhat, K. Fujito, S. P. Denbaars, S. Nakamura and J. S. Speck, *Appl. Phys. Lett.* 95, 251905 (2009).
17. E. C. Young, F. Wu, A. E. Romanov, D. A. Haeger, S. Nakamura, S. P. Denbaars, D. A. Cohen and J. S. Speck, *Appl. Phys. Lett.* 101, 142109 (2012).

# Chapter 7 Optical Investigation of High-Quality Semi-polar (11-22) AlGa<sub>N</sub> layers

## 7.1 Introduction

The AlGa<sub>N</sub>-based UV emitters reported so far are almost exclusively grown on c-plane substrates. This polar orientation leads to built-in electric fields across the active region and thus a reduced quantum efficiency [1]. Another issue in the ternary alloy is the exciton localization induced as a result of alloy compositional fluctuations [2]. This issue becomes more severe for the growth of DUV emitters with a sub-280 nm wavelength, where higher Al content (>50%) is required leading to significantly enhanced compositional fluctuations [3-4]. It is well-known that exciton localization plays an important role in improving the quantum efficiency for III-nitride light-emitting diodes (LEDs), in particular InGa<sub>N</sub> LEDs [5], but large localization disturbs uniform population inversion, thus leading to an increase in threshold current for lasing [2]. Finally, it is understood that it is another great challenge to achieve high Al-content p-type AlGa<sub>N</sub> with good conductivity as a result of its large activation energy. Consequently, the shortest wavelength of the UV laser diodes (LDs) reported so far is limited to 336 nm and such UV LDs can only be operated in pulsed mode with very high thresholds [6].

Building on experience from InGa<sub>N</sub> based semi-polar emitters in the visible spectral region [7], one promising approach forward is to grow UV emitters along semi-/non- polar orientations, which can reduce or eliminate the polarization induced electrical fields. It has also been understood that there exists significant difference in exciton localization between semi-polar and c-plane InGa<sub>N</sub>. Higher homogeneity of indium composition has been achieved in semi-polar (20-21) InGa<sub>N</sub> [8]. Note, however, that atom probe tomography has been used to indicate a greater non-randomness in indium distribution in non-polar InGa<sub>N</sub> compared to polar c-plane [9]. So far, there is rare report on the study of the exciton localization in semi-polar AlGa<sub>N</sub> [10]. Furthermore, it has been predicted theoretically that a higher optical gain could be obtained in semi-/non- polar AlGa<sub>N</sub> based LDs [11-12]. All these imply that semi-/non-polar AlGa<sub>N</sub> can possibly exhibit advantages over than its c-plane counterpart in terms of growing LDs.

However, owing to great challenges in obtaining semi-/non- polar AlGa<sub>N</sub> with high quality, there are only a few reports on the studies of the optical properties of such materials. So far, there has been a near complete absence of research on semi-polar AlGa<sub>N</sub> with high Al composition. Unlike *c*-plane AlGa<sub>N</sub>, semi-/non- polar AlGa<sub>N</sub> generally suffers from basal-plane stacking faults (BSFs) in addition to dislocations, further complicating the study of the optical properties of semi-/non- polar AlGa<sub>N</sub>. Huang *et al* [13] studied the exciton localization of the BSFs-related emission in non-polar AlGa<sub>N</sub> with Al composition ranging from 0 to 0.28. Netzel *et al* [14] investigated the optical polarization properties of both the NBE emission and the BSFs-related emission in semi-polar AlGa<sub>N</sub>. However, in both cases the BSFs-related emission is hardly distinguished from the NBE emission, thus leading to great challenges in performing detailed studies due to the difficulty in obtaining high-quality AlGa<sub>N</sub>.

In Chapter 4, we have developed a two-step overgrowth technique for (11-22) semi-polar AlGa<sub>N</sub> based on the overgrowth approach of semi-polar (11-22) GaN on micro-rod arrayed templates [15-17]. Such two-step overgrown samples exhibits the best crystal quality compared with other reports [18]. So far, we have achieved thick and crack-free semi-polar (11-22) AlGa<sub>N</sub> with Al composition of up to 55%.

In this chapter, the optical properties of these high crystal quality (11-22) semi-polar AlGa<sub>N</sub> samples have been investigated. Both the NBE and the BSFs-related emissions, which have been clearly distinguished as a result of the high crystal quality, have been systematically studied by means of temperature-dependent photoluminescence and RT CL measurements. A comprehensive study on the exciton localization of the NBE and the BSFs-related emissions has been also performed. More importantly, a detailed comparison study has been performed on these semi-polar AlGa<sub>N</sub> samples and their *c*-plane AlGa<sub>N</sub> counterparts with similar Al composition. All the semi-polar AlGa<sub>N</sub> samples show a clear reduction in Al composition fluctuations compared with their *c*-plane counterparts. The results presented demonstrate that semi-polar (11-22) AlGa<sub>N</sub> may be more favourable for being employed to grow DUV LDs than *c*-plane AlGa<sub>N</sub>.

## 7.2 Experimental Details

The semi-polar (11-22) AlGa<sub>N</sub> samples used were grown by using the two-step overgrowth approach, where the thick and crack-free semi-polar (11-22) AlGa<sub>N</sub> has been achieved on the top of nearly-but-not-fully coalesced GaN deliberately grown on the micro-rod arrayed templates. The Al composition of these overgrowth samples ranges from 32.0% to

55.3%. The FWHMs of XRD rocking curves measured along the [1-100]/[11-2-3] directions (XRD measurements along the two directions are typically used to evaluate the crystal quality of III-nitrides [8]) are  $0.292^{\circ}/0.201^{\circ}$  for 32.0% Al and  $0.381^{\circ}/0.206^{\circ}$  for 55.3% Al respectively, representing the best quality for semi-polar (11-22) AlGaIn with similar Al composition ever reported. It has also been demonstrated that our overgrowth technique can effectively both manage strain and improve crystal quality simultaneously [18]. More details about the overgrowth and structural characterization can be found in Chapter 5.

PL measurements were performed by using a doubled-frequency Argon ion laser with an excitation wavelength of 244 nm. For temperature-dependent PL measurements, the samples were held in a helium closed-circuit cryostat where the temperature can be controlled from 10 to 300K. The photoluminescence was spatially separated by a diffraction grating within a 0.5 m monochromator and then analysed using a CCD which was thermoelectrically cooled down to  $-70^{\circ}\text{C}$ . CL measurements were carried out at RT using a field-emission gun scanning electron microscope equipped with a 0.125m spectrometer and electron multiplying CCD detector and using a Cassegrain reflecting objective to collect luminescence down to 200 nm [19].

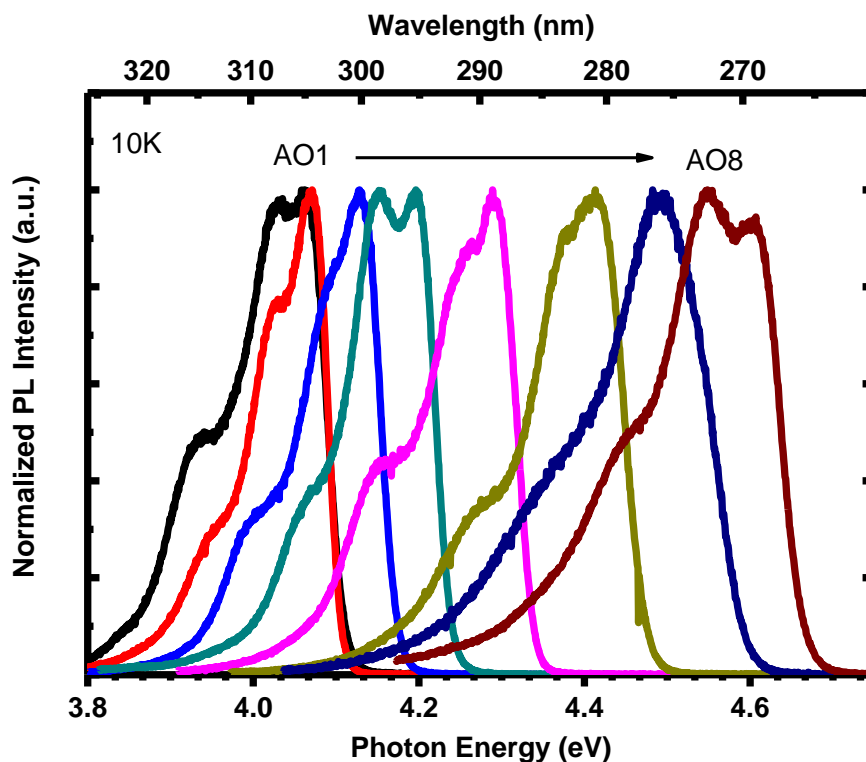


**Figure 7.1** Normalized LT PL spectra of semi-polar (11-22) AlGaIn overgrowth samples.

## 7.3 Results and Discussion

### 7.3.1 LT PL

Figure 7.1 shows the normalized PL spectra measured at 10K, exhibiting two main peaks in all the samples. Being similar to semi-polar GaN, these two peaks are due to the NBE and BSFs-related emission, respectively. In all PL spectra, a cascade of longitudinal optical (LO) phonon replica on the low energy side of the main peaks have also been observed, with an energy spacing of around 95-100meV as shown in Figure 7.2, where the PL spectrum of the AlGaN sample with 32.2% Al content is provided in a logarithmic scale as an example. The LO phonon energy obtained for our AlGaN samples agrees well with the LO phonon energy reported for GaN (91meV) [20] and AlN (110meV) [21].

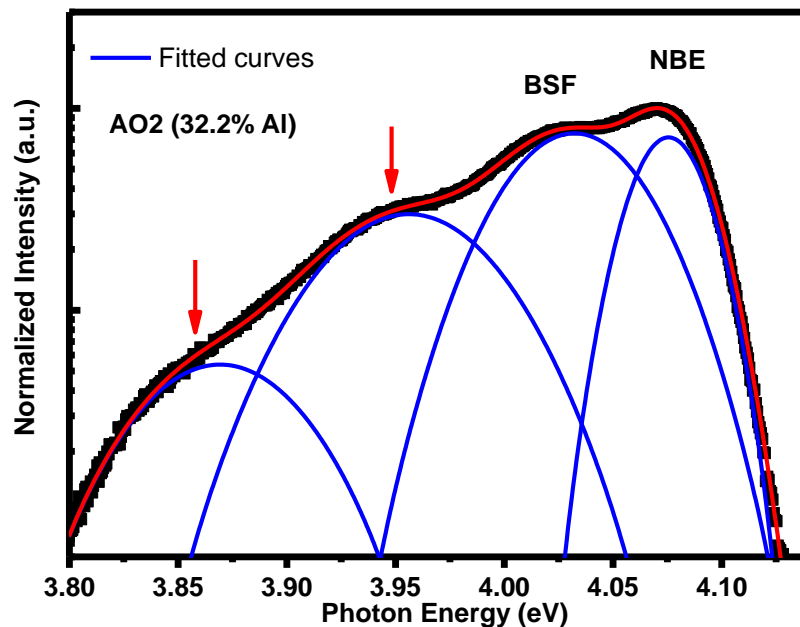


**Figure 7.2 Multiple peaks Gaussian fitting of the LT PL spectrum for the AlGaN with 32.2% Al content. The red arrows show LO phonon replicas.**

Although the NBE and the BSF emissions are clearly separated at a low temperature, a fitting using multiple Gaussian curves has been made in order to obtain the accurate emission peak energies of these two emissions. Figure 7.2 presents an example about our fitting. Although fitting with symmetric Gaussian curves is a commonly-used method in PL spectrum [4, 22], it should be noted that the real peaks are not strictly symmetric, which might cause some deviation in the value of peak positions and FWHMs.

Figure 7.3 shows the emission energies and their separation of the NBE and the BSFs-related emission as a function of Al composition, exhibiting that the BSFs-related emission is

about 41 meV and 52 meV lower than that of the NBE emission when the Al composition is 32.0% and 55.3%, respectively. Furthermore, Figure 7.3 demonstrates that the emission energy separation between the NBE and the BSFs-related emissions increases with increasing Al composition, agreeing with the other report [13].

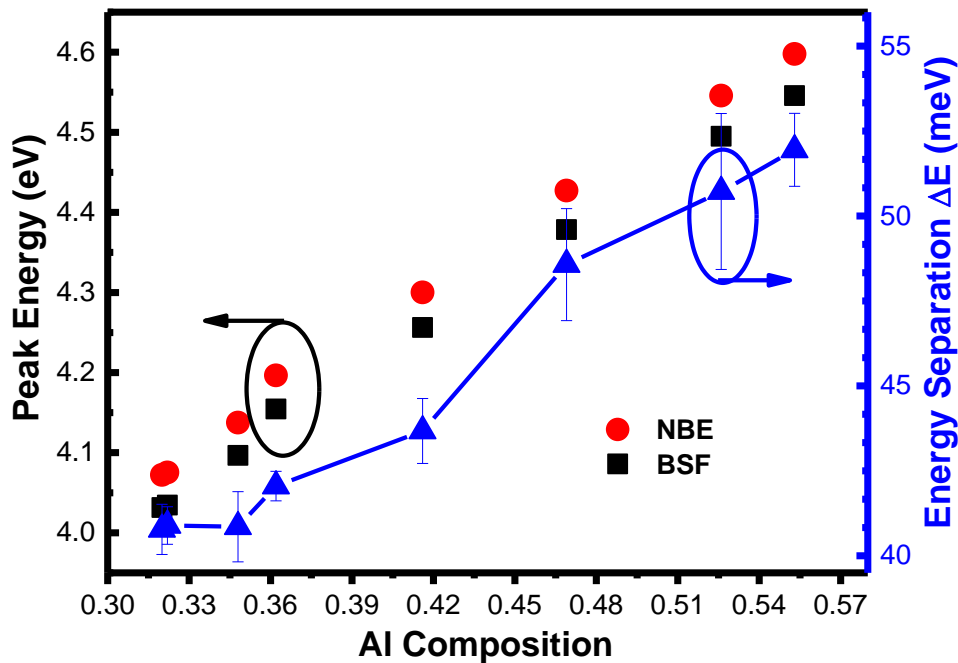


**Figure 7.3 Emission peak energies of the NBE and the BSFs-related emissions, and their energy separation as a function of Al composition.**

Generally speaking, the emission energy separation between NBE and BSFs-related emission is also affected by the difference of their respective exciton binding energies and their localization energy difference. Tischer *et al* [23] reported that the energy separation between the NBE and the BSFs-related emission in (11-22) AlGaIn is larger than that in GaN, suggesting that the BSFs regions exhibiting a cubic core with lower Al composition serving as a “quantum well” (QW) are sandwiched by the regions without containing BSFs as “barriers”. Assuming that the composition discrepancy between such “QWs” and such “barriers” increases with increasing Al composition, the exciton binding energy difference between NBE and BSFs-related emission will be enhanced with increasing Al composition. Another possible reason for the increase of the energy separation involves the polarization field induced QCSE in BSF regions. Lahnemann *et al* [24] suggested that the spontaneous polarization at the wurtzite/zinc-blende interface could result in electric fields across the BSFs regions, leading to a redshift of the BSF related emission. The spontaneous polarization induced electrical fields are expected to be stronger with increasing Al composition [25].

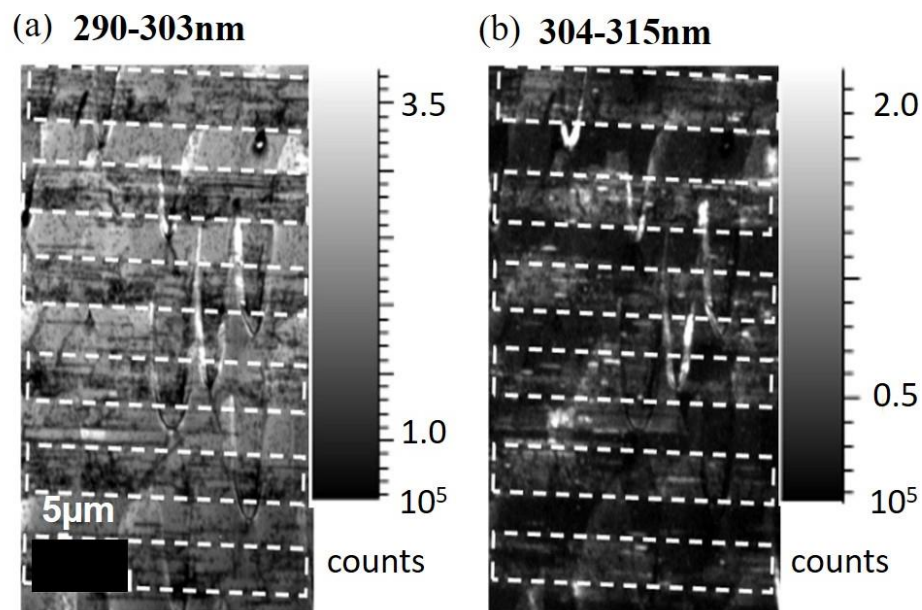


**Figure 7.4** Integrated RT CL intensity images of sample AO4 with a detected wavelength at 290-303nm (a) and 304-315nm (b), where the dashed rectangles indicate BSFs regions. Dr. J. Bruckbauer is acknowledged for provision of this measurement.

To further characterize the emission properties of AlGa<sub>N</sub> alloys, RT CL measurements were carried out on the AlGa<sub>N</sub> sample with 36.2% Al content as an example, which is shown in Figure 7.4. The excitation voltage used is 5 kV, corresponding to an electron penetration depth of ~100 nm, and thus only the emission from the AlGa<sub>N</sub> can be detected. Since BSFs are two dimensional extended defects embedded in a basal plane, they appear as sets of parallel lines or bundles in CL or transmission electron microscope (TEM) images [16,26]. The RT CL shows two dominant emissions in the region 290-315 nm, which we attribute to NBE emission from regions of different composition. As shown by the CL intensity variations in Figure 6.4, BSFs-related regions (dashed rectangles) are separated by BSF-free regions, forming a periodic distribution on the AlGa<sub>N</sub> surface. Such a distribution is similar to that observed in the TEM images of our overgrown GaN [16], suggesting that the BSFs within the underlying GaN extend to the top AlGa<sub>N</sub> layer. The majority of the surface is dominated by the NBE emission at about 297 nm, as observed in the CL intensity image with an integration window of 290-303 nm (Figure 7.4 (a)). The CL intensity image integrated over 304-315 nm reveals a different Al content at the chevrons (running perpendicular to the stripes), where the NBE peak is shifted to approximately 305 nm as shown in Figure 7.4 (b).

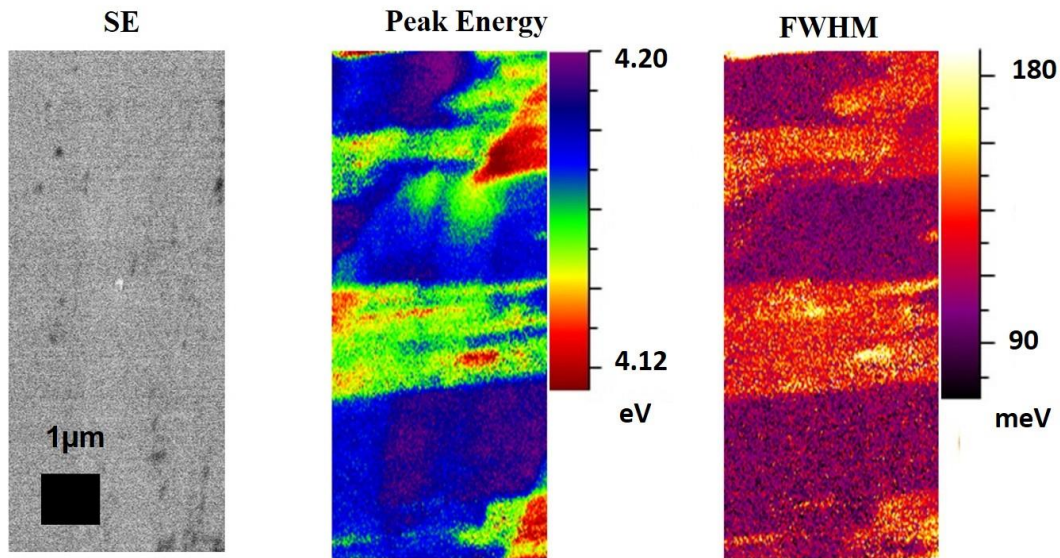


**Figure 7.5 High spatial resolution CL imaging in a chevron-free region of sample AO4. The SE image, emission peak energy image and emission peak FWHM image are shown. Dr. J. Bruckbauer is acknowledged for provision of this measurement.**

High spatial resolution CL was performed to further investigate the emission characteristics of the NBE in a chevron-free region. Figure 7.5 shows the CL peak energy and the FWHM images of the sample, alongside the corresponding secondary electron (SE) image of the mapped area. The area where BSFs are present exhibits a lower emission energy at  $\sim 4.14$  eV and a broader CL linewidth (FWHM) of  $\sim 150$  meV, compared to the area where there are no BSFs (with an emission energy of  $\sim 4.18$  eV and a CL linewidth of  $\sim 100$  meV). The broader linewidth is most likely due to the lower quality of the material in that region with a high density of BSFs, which also leads to the apparent shift in energy.

### 7.3.3 Temperature dependent PL

In order to investigate exciton localization arising from Al compositional fluctuations in AlGa<sub>N</sub> alloys, temperature-dependent PL measurements for all AlGa<sub>N</sub> samples have been performed. In all cases, the peak energy of the NBE exhibits the same “S” shape behaviour when the temperature increases from 10 to 300 K, namely, it redshifts initially, then blueshifts and finally redshifts. Such a behaviour has been widely reported in c-plane AlGa<sub>N</sub> as an indicator of the existence of localized states [4]. The initial redshift is due to carrier redistribution to deeper localized states via a hopping process. With increasing temperature, the carriers are delocalized to higher energy states, giving rise to a blueshift in peak energy. The redshift at higher temperatures is due to the temperature induced bandgap shrinkage.

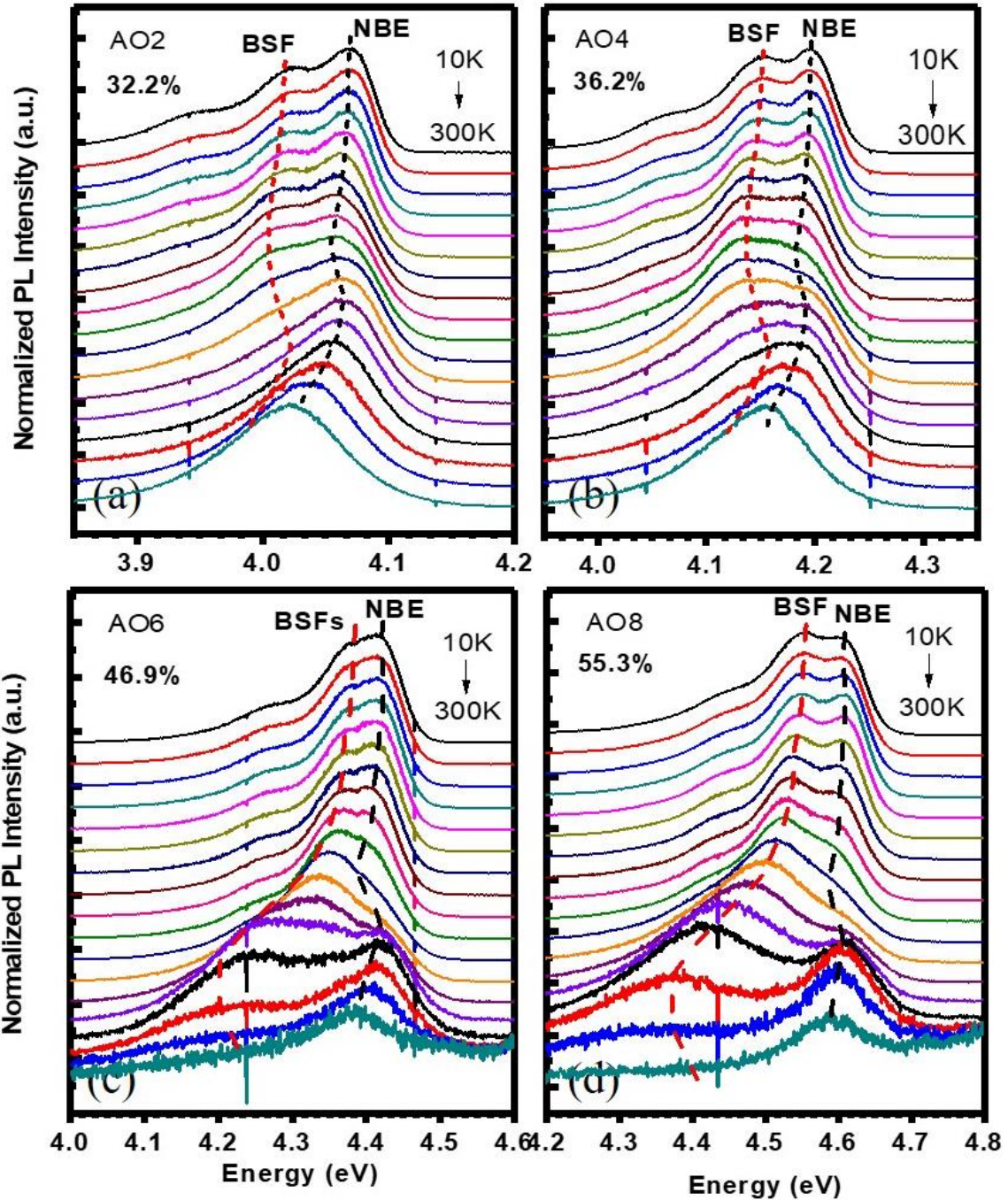


**Figure 7.6** Temperature-dependent PL spectra of the semi-polar (11-22) AlGaIn with Al content of 32.2% (a), 36.2% (b), 46.9% (c) and 55.3% (d). The dash lines show the emission energy shift of the NBE and BSFs.

Being similar to c-plane AlGaIn, such “S” shape behaviour for the NBE in semi-polar AlGaIn is also attributed to Al compositional fluctuation induced exciton localization. In contrast, the temperature dependent behaviour of the BSFs-related emission shows a different story. For the samples with low Al composition (< 46.9%), the emission peak still exhibits the similar “S” shape behaviour as the NBE does, whereas the samples with high Al composition

(> 46.9%) show a redshift and then a blue shift only. The typical temperature-dependent PL spectra corresponding to the above two regions are shown in Figure 7.6 (a)-(b) and Figure 7.6 (c)-(d), where the samples with 32.2% and 36.2% Al content and 46.9% and 55.3% Al content are used as examples, respectively.

As shown in Figure 7.6 (c)-(d), the BSFs-related emission quenches quickly at high temperatures. From the XRD data shown in Figure 5.7, it can be seen that the XRC FWHM along [1-100] increases from  $\sim 0.3^\circ$  for low-Al-content samples to  $\sim 0.4^\circ$  for high-Al-content samples. This means with higher Al incorporation, higher density of defects, e.g. partial dislocations associated with the BSFs and the threading dislocations, are expected. They act as non-radiative recombination centres, contributing to the fast thermal quench at high temperatures observed in the samples with higher Al-content.

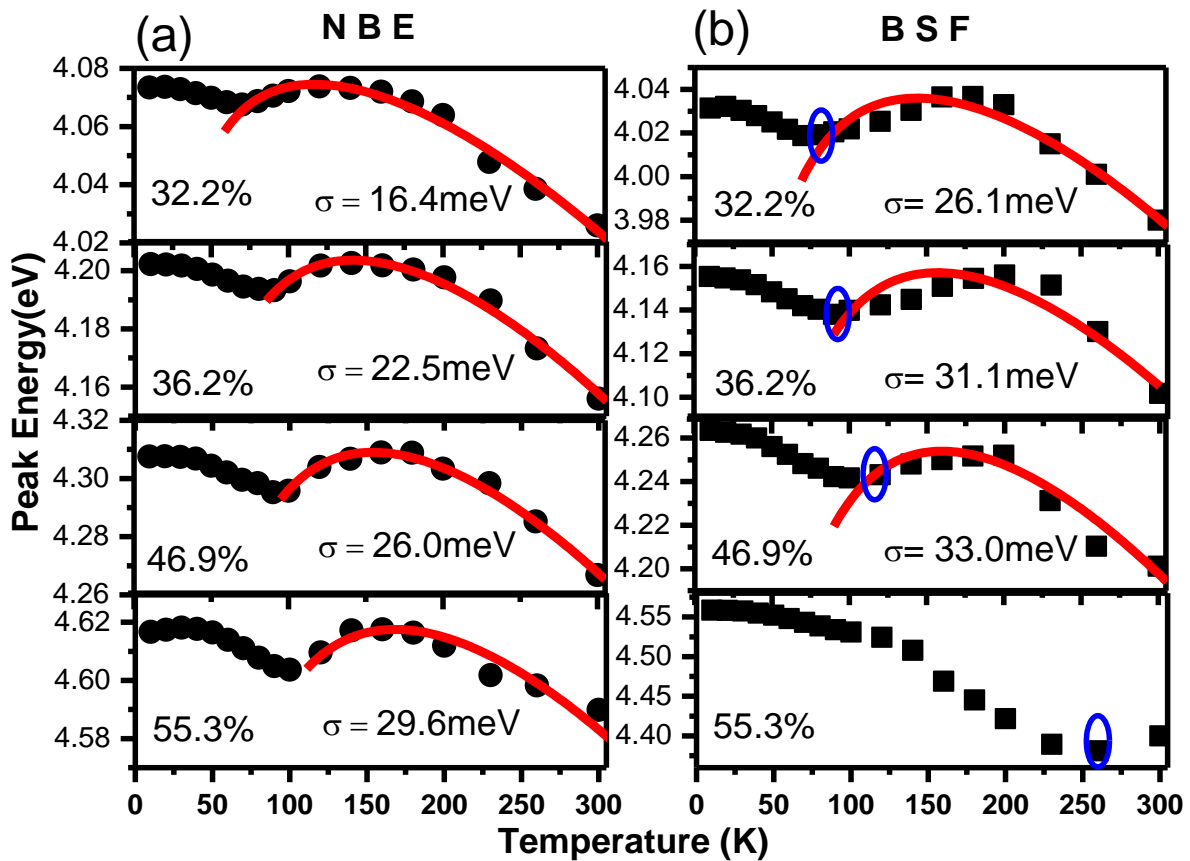


**Figure 7.7** Peak energy shifts for the NBE (a) and BSFs-related (b) emissions of selected semi-polar (11-22) AlGaIn samples (AO2, AO4, AO6 and AO8). The red solid lines represent the fitted curves by using the modified Varshni equation in order to obtain exciton localization depth. The blue circles in (b) indicate the transition temperatures.

#### 7.3.4 Localization Effect

Figure 7.7 shows the temperature dependence of the emission peak energies of the NBE and the BSFs-related emissions. The modified Varshni equation based on a band-tail-filling model, has been widely used in InGaN and can be employed to fit the emission peak energy,

$$E(T) = E(0) - \frac{\alpha T^2}{T + \beta} - \frac{\sigma^2}{k_B T} \quad (7.1)$$

where  $E(0)$  is the band gap energy of AlGaIn,  $\alpha$  and  $\beta$  are the fitting parameters,  $k_B$  is Boltzmann's constant and  $\sigma$  is the localization depth which represents an estimated degree of localization. The best fitting in both the NBE and the BSFs-related emissions can be obtained with  $\alpha = (1-1.18) \times 10^{-3}$  eV/K and  $\beta = (1100-1500)$  K, which are comparable with the values reported for their  $c$ -plane counterparts [27]. For AlGaIn with  $47\% < \text{Al}\% < 56\%$ , it is difficult to estimate the localization depth of the BSFs-related emission as a result of the quenching of the BSFs-related emission at high temperatures. However, it could be estimated from a transition temperature at which the emission peak energy switches from a redshift to a blueshift. When the Al composition increases from 32.0% to 46.9%, the localization depth increases from 26 to 33 meV, where the corresponding transition temperature increases from 80 to 100K. Given that the transition temperature is as high as 230K for the sample with 55.3% Al content, the localization depth of the BSFs-related emission should be much higher than 33 meV.

The obtained localization depths of the NBE and the BSFs-related emission have been provided in Figure 7.7. When the Al composition increases from 32.0% to 55.3%, the localization depth of the NBE increases from 16 to 29 meV, while the localization depth of the BSF related emission increases from 26 to 33 meV with increasing Al content from 32.0% to 46.9%, about 10 meV larger than that for the NBE.

One possible reason is due to the Al redistribution in BSF regions as mentioned above [23]. Such a compositional discrepancy between the BSF regions (serving as "QWs") and the BSF-free regions (serving as "barriers") forms a kind of "hetero-structure", roughening their interface sharpness. Being similar to InGaIn/GaN systems, this kind of interfacial roughness enhances exciton localization.

Furthermore, the localization effect in BSFs can be further enhanced as a result of the generation of the donor nuclei in the vicinity of BSFs. As Corfdir *et al* [28] highlighted, the coupling between donor nuclei and BSFs could lead to the localization of electrons within the plane of BSFs in  $a$ -plane GaIn. In our AlGaIn, in particular the high Al contained AlGaIn, the

generation of these extrinsic donors is probably further enhanced, as a large ratio of Al precursor/Ga precursor is required.

It is interesting to compare exciton localization in semi-polar (11-22) AlGa<sub>N</sub> with that in *c*-plane AlGa<sub>N</sub> [4, 29-30]. The typical values of the localization depths and the LT PL line-width in *c*-plane AlGa<sub>N</sub> with various Al composition, which are extracted from Ref. 29, have been summarized in Table 7.1.

**Table 7.1 Localization depths of semi-polar (11-22) AlGa<sub>N</sub> and *c*-plane AlGa<sub>N</sub>.**

Al%	Semi-polar (11-22) AlGa <sub>N</sub>		<i>c</i> -plane AlGa <sub>N</sub> [29]	
	$\sigma$ (NBE) / meV	PL FWHM / meV	$\sigma$ (NBE) / meV	PL FWHM / meV
32.2%	16.4	31	40	36
36.2%	22.5	35	43	39
46.9%	26.0	39	56	45
55.3%	29.6	48	67	51

It can be observed that the localization depth of the NBE increases from 40 to 67 meV when the Al composition increases from 32.2% to 55.3% in *c*-plane AlGa<sub>N</sub>, which are considerably larger than those of the semi-polar (11-22) AlGa<sub>N</sub> with similar Al composition. It means that the exciton localization in semi-polar (11-22) AlGa<sub>N</sub> is generally weaker than that in its *c*-plane counterpart.

This is further confirmed by the PL linewidths, where the PL emission of the semi-polar (11-22) AlGa<sub>N</sub> is generally narrower than that of its counterpart. As mentioned above, a reduced localization depth leads to an increase in optical gain and thus a reduction in threshold for lasing. This means that semi-polar (11-22) AlGa<sub>N</sub> exhibits major advantages over than its *c*-plane counterpart, in particular in the growth of DUV LDs. Of course, a further improvement in crystal quality is necessary, as BSFs and their associated partial dislocations in semi-polar AlGa<sub>N</sub> can also affect the performance of LDs such as threshold for lasing.

## 7.4 Conclusion

We have investigated the optical properties of a number of semi-polar (11-22) AlGa<sub>N</sub> samples with Al composition ranging from 32.0% to 55.3%. Combination of temperature-dependent PL and RT CL measurements have been performed in order to study both NBE and

BSFs-related emissions. The energy separation between the two emissions increases with increasing Al composition, which is mainly ascribed to the compositional discrepancy within BSF regions and enhanced QCSE also within the BSF regions. A detailed study of exciton localization of the NBE and the BSFs-related emissions have been performed, showing the localization depth of the BSFs-related emission is larger than that of the NBE in each sample. Most importantly, the localization depth of semi-polar (11-22) AlGa<sub>N</sub> is generally smaller than that of its *c*-plane counterpart, suggesting that semi-polar (11-22) AlGa<sub>N</sub> is more favourable for the growth of DUV LDs than its counterpart. Our results provide a deep insight into the optical properties of semi-polar AlGa<sub>N</sub>, which is of significant importance to the development of semi-polar AlGa<sub>N</sub> based DUV LDs.

## References

1. A. Khan, K. Balakrishnan, and T. Katona, *Nat. Photonics* 2, 77 (2008).
2. M. Adachi, *Jpn. J. Appl. Phys.* 53, 100207 (2014).
3. K. Wang, K. P. O'Donnell, B. Hourahine, R. W. Martin, I. M. Watson, K. Lorenz, and E. Alves, *Phys. Rev. B* 80, 125206 (2009).
4. K. B. Lee, P. J. Parbrook, T. Wang, F. Ranalli, T. Martin, R. S. Balmer, and D. J. Wallis, *J. Appl. Phys.* 101, 053513 (2007).
5. Y. Narukawa, Y. Kawakami, S. Fujita, and S. Nakamura, *Phys. Rev. B* 59, 10283 (1999).
6. H. Yoshida, Y. Yamashita, M. Kuwabara, and H. Kan, *Appl. Phys. Lett.* 93, 241106 (2008).
7. T. Wang, *Semicond. Sci. Technol.* 31, 093003 (2016).
8. M. Funato, A. Kaneta, Y. Kawakami, Y. Enya, K. Nishizuka, M. Ueno, and T. Nakamura, *Appl. Phys. Express* 3, 021002 (2010).
9. F. Tang, T. Zhu, F. Oehler, W. Y. Fu, J. T. Griffiths, F. C. -P. Massabuau, M. J. Kappers, T. L. Martin, P. A. J. Bagot, M. P. Moody, and R. A. Oliver, *Appl. Phys. Lett.* 106, 072104 (2015).
10. D. V. Dinh, S. N. Alam, and P. J. Parbrook, *J. Cryst. Growth* 435, 12 (2016).
11. A. A. Yamaguchi, *Appl. Phys. Lett.* 96, 151911 (2010).
12. K. Kojima, A. A. Yamaguchi, M. Funato, Y. Kawakami, and S. Noda, *J. Appl. Phys.* 110, 043115 (2011).
13. H. -M. Huang, Y. -C. Wu, and T. -C. Lu, *J. Electrochem. Soc.* 158, H491 (2011).
14. B. Netzel, J. Stellmach, M. Feneberg, M. Frentrup, M. Winkler, F. Mehnke, T. Wernicke, R. Goldhahn, M. Kneissl, and M. Weyers, *App. Phys. Lett.* 104, 051906 (2014).
15. Y. Gong, K. Xing, B. Xu, X. Yu, Z. Li, J. Bai, and T. Wang, *ECS Trans.* 66, 151 (2015).
16. Y. Zhang, J. Bai, Y. Hou, R. M. Smith, X. Yu, Y. Gong, and T. Wang, *AIP Adv.* 6, 025201 (2016).
17. J. Bai, B. Xu, F. G. Guzman, K. Xing, Y. Gong, Y. Hou, and T. Wang, *Appl. Phys. Lett.* 107, 261103 (2015).
18. Z. Li, L. Jiu, Y. Gong, L. Wang, Y. Zhang, J. Bai, and T. Wang, *Appl. Phys. Lett.* 110, 082103 (2017).
19. P. R. Edwards, L. K. Jagadamma, J. Bruckbauer, C. Liu, P. Shields, D. Allsopp, T. Wang, and R. W. Martin, *Microsc. Microanal.* 18, 1212 (2012).

20. V. Y. Davydov, Y. E. Kitaev, I. N. Goncharuk, A. N. Smirnov, J. Graul, O. Semchinova, D. Uffmann, M. B. Smirnov, A. P. Mirgorodsky, and R. A. Evarestov, *Phys. Rev. B* 58, 12899 (1998).
21. T. Onuma, S. F. Chichibu, T. Sota, K. Asai, S. Sumiya, T. Shibata, and M. Tanaka, *Appl. Phys. Lett.* 81, 652 (2002).
22. R. Pecharroman-Gallego, P. R. Edwards, R. W. Martin, and I. M. Watson, *Mater. Sci. Eng. B* 93,94 (2002).
23. I. Tischer, M. Frey, M. Hocker, L. Jerg, M. Madel, B. Neuschl, K. Thonke, R. A. R. Leute, F. Scholz, H. Groiss, E. Müller, and D. Gerthsen, *Phys. Stat. Sol. (b)* 251, 2321 (2014).
24. J. Lahnemann, U. Jahn, O. Brandt, T. Flissikowski, P. Dogan, and H. T. Grahn, *J. Phys. D: Appl. Phys.* 47, 423001 (2014).
25. E. T. Yu, X. Z. Dang, P. M. Asbeck, S. S. Lau, and G. J. Sullivan, *J. Vac. Sci. Technol. B* 17, 1742 (1999).
26. R. Liu, A. Bell, F. A. Ponce, C. Q. Chen, J. W. Yang, and M. A. Khan, *Appl. Phys. Lett.* 86, 021908 (2005).
27. R. Passler, *J. Appl. Phys.* 90, 3956 (2001).
28. P. Corfdir, J. Ristic, P. Lefebvre, T. Zhu, D. Martin, A. Dussaigne, J. D. Ganiere, N. Grandjean, and B. Deveaud-Pledran, *Appl. Phys. Lett.* 94, 201115 (2009).
29. N. Nepal, J. Li, M. L. Nakarmi, J. Y. Lin, and H. X. Jiang, *Appl. Phys. Lett.* 88, 062103 (2006).
30. G. Steude, B. K. Meyer, A. Goldner, A. Hoffmann, F. Bertram, J. Christen, H. Amano, and I. Akasaki, *Appl. Phys. Lett.* 74, 2456 (1999).

# Chapter 8 Summary and Future work

## 8.1 Summary

Due to the tremendous application prospects, AlGa<sub>N</sub>-based UV emitters have recently attracted much research interest, in particular for the deep UV emitters operating below 280 nm wavelength where the high Al compositions are required. Since the conventional *c*-plane AlGa<sub>N</sub> structures suffer from the quantum-confined stark effect across the active regions, we move forward to the research on a semi-polar direction, i.e., (11-22), in which the QCSE is expected to significantly reduced and hence the quantum efficiency potentially improved.

The main work of this research is about the epitaxial growth of high quality semi-polar (11-22) AlGa<sub>N</sub> epilayers with the MOCVD technique as well as comprehensive characterization of structural and optical properties of the AlGa<sub>N</sub> layers.

Semi-polar (11-22) AlGa<sub>N</sub> epilayers with various Al compositions have been obtained with two different approaches. One is to directly grow standard AlGa<sub>N</sub> on the AlN or GaN buffer layer on the planar (10-10) *m*-plane sapphire, and another one is to grow AlGa<sub>N</sub> on the overgrown GaN on micro-rod templates with a two-step overgrowth technique developed by our group.

In both ways, the Al composition could be tuned spanning a wide range by varying the TMAI / (TMAI + TMGa) ratio. The typical undulations and arrow-like features are observed in all semi-polar AlGa<sub>N</sub> samples, but they are larger and deeper in overgrowth samples. CL measurements in overgrowth samples show that the side peaks in PL spectrum derive from the non-uniformity of Al distribution near the “chevron” regions. It has been found that the crystal quality is improved with increasing temperature, whereas the surface morphology reaches up to the best at an intermediate temperature.

Moreover, semi-polar AlGa<sub>N</sub> MQWs with various QW thickness grown on standard AlGa<sub>N</sub> show no clear blueshift with increasing excitation power, indicating the absence of QCSE within the semi-polar MQWs.

More importantly, the standard AlGa<sub>N</sub> samples exhibit poor crystal quality and severe wafer cracking whereas the overgrowth samples are crack-free across 2-inch wafers and exhibit excellent crystal quality. The FWHMs of the X-ray rocking curves along the [1-100]/[11-2-3]

directions are  $0.292^{\circ}/0.201^{\circ}$  for 32.0% Al and  $0.381^{\circ}/0.206^{\circ}$  for 55.3% Al, respectively, representing the best report for semi-polar AlGa<sub>N</sub> so far.

By performing a detailed azimuth dependent (11-22) on-axis XRC measurements, the XRC FWHMs of the AlGa<sub>N</sub> samples with two different structures are compared, indicating a significant improvement of the overall crystal quality with the overgrowth technique. XRD studies on the off-axis planes including the (000*n*) (*n*=2, 4, 6) and the (*n*0-*n*0) (*n*=1, 2, 3) diffraction are performed, also showing dramatically improved crystal quality of overgrowth samples compared to the standard AlGa<sub>N</sub>.

Detailed studies of the strain have been performed using a triclinic unit cell model by means of multiple on- and off-axis XRD  $\omega/2\theta$  measurements. It shows that the in-plane strain are anisotropic and even compressive instead of tensile, which is advantageous to prevent cracking. Further studies on the (11-22) symmetric and the (11-24) asymmetric RSMs measurements reveal large lattice tilts between the AlGa<sub>N</sub> and the Ga<sub>N</sub>, confirming significant strain relaxation in the AlGa<sub>N</sub> overgrowth layers. It indicates that our overgrowth method is an effective way to both release the strain and improve the crystal quality simultaneously, which plays an important role in developing semi-polar deep UV emitters with a step-change in optical performance.

Furthermore, the optical properties of high quality semi-polar (11-22) AlGa<sub>N</sub> layers with Al composition ranging from 32.0% to 55.3% are investigated systematically. Combination of LT PL and RT CL measurements has been performed in order to study both NBE and BSFs-related emissions. The energy separation between the two emissions increases with increasing Al composition, which is mainly ascribed to the compositional discrepancy within BSF regions and enhanced QCSE also within the BSF regions.

A detailed study of exciton localization of the NBE and the BSFs-related emissions has been performed with the temperature dependent PL measurements. Localization energies for both emissions are obtained by using the modified Varshni equation, showing the localization depth of the BSFs-related emission is larger than that of the NBE in each sample. Most importantly, the localization depth of semi-polar (11-22) AlGa<sub>N</sub> is generally smaller than that of its c-plane counterpart, suggesting that semi-polar (11-22) AlGa<sub>N</sub> is more favourable for the growth of DUV LDs than its counterpart. Our results provide a deep insight into the optical properties of semi-polar AlGa<sub>N</sub>, which is of significant importance to the development of semi-polar AlGa<sub>N</sub> based DUV LDs.

## 8.2 Future work

The future work in this project will be suggested as follows.

### (1) Structural analysis for AlGa<sub>N</sub> overgrowth samples

To characterise the defect densities, e.g. BSFs and threading dislocation densities, and further study the defect reduction mechanism with the overgrowth technique, the TEM measurement is suggested. Also, accurate Al composition analysis throughout all AlGa<sub>N</sub> overgrown samples are recommended.

### (2) Growth condition optimisation of current overgrowth technology

Growth conditions with current overgrowth technology need further optimization in the future, in order to get smoother surface and better crystal quality for semi-polar (11-22) AlGa<sub>N</sub> overgrowth layer. This may involve the optimization of the reactor pressure, the flow rates of TMGa and TMAI, and the total flow of carrier gas.

Chemical mechanical polishing (CMP) might be considered to remove the strong arrow-like features to improve the flatness of AlGa<sub>N</sub> surface, given the poor surface morphology in the high-Al-content samples.

### (3) Further improvement with other approaches

To improve the crystal quality even further, other approaches might be considered. One approach may involve the AlGa<sub>N</sub> overgrowth on nano-rod templates. Since the lattice-mismatch induced strain could be better managed by the nano-rod templates (refer to Conroy *et al*, J. Mater. Chem. C 3, 431 (2015)) compared to the micro-rod templates, the crystal quality of AlGa<sub>N</sub> might be improved further. Another approach is to grow AlGa<sub>N</sub> on nano-porous GaN template, which is actually under test in our group. Such porous GaN template is obtained by the photoelectrochemical (PEC) etching to the n-doped as-grown GaN. It is expected that AlGa<sub>N</sub> grown on such nano-porous template will benefit from great strain relaxation and negligible misfit dislocation.

### (4) Semi-polar AlGa<sub>N</sub> MQWs growth

Semi-polar AlGa<sub>N</sub> MQWs will grow on the overgrown AlGa<sub>N</sub> templates. The growth conditions for the QWs may be optimized by tuning the well and/or barrier width, the NH<sub>3</sub> flow rate and the growth rate of the QW.

Characterization in these QW samples may also be performed to investigate the optical properties. This includes the investigation of QCSE within the semi-polar MQWs and optical polarization properties in semi-polar AlGa<sub>N</sub> MQWs with various Al compositions.

#### (5) N type and p type doping investigation

Also, studies on the n-type and p-type doping of the semi-polar AlGa<sub>N</sub> are also included in the plan. Different dopant concentration will be tried to find the optimal condition. The mobility and concentration of electrons (n-type) and holes (p-type) in semi-polar AlGa<sub>N</sub> will be examined. For p-type semi-polar AlGa<sub>N</sub>, different doping approaches may be tried to achieve conductive layers, such as compositional-graded p-AlGa<sub>N</sub>. Besides, to make a ohmic contact to p-AlGa<sub>N</sub>, a thin GaN layer will be deposited on top of p-AlGa<sub>N</sub> as a contact layer. The thickness of p-GaN needs to optimized to reduce UV absorption and improve contact property.

#### (6) Full UV device structure growth and characterization

Finally, the full structural UV LEDs will be demonstrated. The structure of a semi-polar UV LED will consist of a thick un-doped AlGa<sub>N</sub> overgrowth layer, a Si-doped n-type AlGa<sub>N</sub> layer, several pairs of semi-polar AlGa<sub>N</sub> MQWs, a Mg-doped p-AlGa<sub>N</sub> electrons blocking layer, a p-AlGa<sub>N</sub> layer and a heavily doped p-GaN contact layer. The device performance of semi-polar AlGa<sub>N</sub> UV LEDs will be studied, including I-V curves, electroluminescence, light output power, etc. It is suggested to make comparison between the semi-polar UV devices and the standard *c*-plane counterparts, in terms of internal quantum efficiency, light output power and optical polarization property, etc.